A New Hybrid Agent-Based Model Approach to Evaluate Antibody-Drug Conjugates in Solid Tumors

by

Bruna Menezes

A dissertation submitted in partial fulfillment
of the requirements for the degree of
Doctor of Philosophy
(Chemical Engineering)
in the University of Michigan
2021

Doctoral Committee:

Professor Jennifer Linderman, Co-chair
Associate Professor Greg Thurber, Co-chair
Professor Gary Luker
Associate Professor Deepak Nagrath

Bruna Menezes
bmenezes@umich.edu
ORCID ID: 0000-0002-2155-2715

Dedication

In honor to my parents for all they have done for me

and

my incredible husband and life partner

Acknowledgments

There are many people whom I am deeply thankful for during this challenging journey. The completion of this work would not be possible without their support and guidance. Here I eagerly take the time to thank all of them.

First, I thank God for providing me this opportunity to achieve one of my dreams: to study in such a prestigious institution as the University of Michigan and have outstanding advisors, mentors, labmates, classmates, friends, opportunities, and so many resources. Here, I have grown not only as a scientist, young professional, and leader, but also in my faith and maturity. I feel incredibly humbled and grateful that through this extremely challenging season, God's tangible presence and provision sustained me through all the heights and valleys.

I could not be more thankful to be advised by both Dr. Jennifer Linderman and Dr. Greg Thurber. Under their different advising and mentorship styles, I learned immensely as they often challenged me to think critically while giving unreserved support. Jennifer has been a role model to me as a scientist, female engineer, and minorities' advocate. Her enthusiasm for research and diversity in academia is truly inspirational. Greg's excitement about the field of antibody-drug conjugates and his teachings on pharmacology has equipped me to do this work. His professionalism, willingness to help, and his funny sense of humor certainly made meetings and classes even more enjoyable. It truly has been an honor and privilege to have worked for both of them. Thank you also to the other committee members, Dr. Gary Luker and Dr. Deepak Nagrath, for their help and input for me to conclude this work.

I want to thank all my classmates, labmates, postdocs, and research staff who have trained me, helped me study, discussed research difficulties, figured out possible issues with my simulation runs or experimental results, and even lent me a pair of eyes to look at my code when I could not find that tricky, sneaky bug. Thank you Eshita Dr. Khera, Dr. Sarah Owen, Iona Nadra, Luciana Pinheiro, Stephen Vicchio, Nahal Habibi, Dr. Phillip Spinosa, Dr. Joey Cicchese, Louis Joslyn, Patrick Kinnunen, Ray Asare, Celia Shujun Dong, Melissa Calopiz, Paul Wolberg, Dr.

Elsje Pienaar, Dr. Caitlin Hult, Dr. Timothy Wessler, Dr. Liang Zhang, Dr. Sumit Bhatnagar, Dr. Cornelius Cilliers, Dr. Tejas Navaratna, Dr. Lydia Atangcho, Ian Nessler, Reginald Evans, Anna Kopp, Marshall Case, Yinuo Chen, Haolong Huan, Jane Kwon, Dr. Mukesh Mahajan, and Dr. Corine Jackman. I especially want to thank Paul Wolberg for teaching me almost everything I know about C++ and for always being willing to help me when I could not do something by myself. The completion of this thesis would not be possible without his help. Also, I would like to give a special thank you to Eshita Khera for her help in the classroom, studying with me during the late hours at the Duderstadt library (also known as the 'Dude') and at the NCRC, and her help in the lab. Her amazing friendship has extended beyond science and will surely remain after the conclusion of this PhD.

I would like to thank the mentors that I could always reach out to during difficult times in academia, for my professional pursuits, and for my mental health: Dr. Susan Montgomery, Debbie Taylor, Crystal Ashby, and Angela Farrehi. Their work is so fundamental for the success of minority students in academia, and I could not thank them enough for their support any time I needed it.

Thank you also for my advisors in my undergraduate education that highly motivated me to pursue higher education. Dr. James Wilson was the main reason I pursued graduate school. He accepted me in the Honors Program, taught me the importance of leadership and excellence, supported me with my application statements, and even helped me find funds to pay for application fees. I wish he could see that I am becoming the Doctor of Philosophy in chemical engineering he was confident I could be. Thank you also to Dr. Michael Gymerah for giving me guidance and support to navigate in the complex scientific world.

Outside of academia, I want to thank my incredible friends and church community who have supported me during my deep lows. Thank you to Kenny and Annelie Lentz for loving me like a daughter and being my unofficial host parents since I first came to the USA. Their friendship and lives have encouraged me to seek God with all my heart. Thank you also to Terry Parker and her family for supporting me even at a distance. Anita Luong, Elaine Lee, Jasmine Jones, Laura Wong, Cathy Wong, and Kristin and Solomon Zheng: growing spiritually and in community with you all has been a privilege. Thank you also Maria and Daniel Yamamoto for your friendship, support, and for being my local host parents.

Thank you also to my cheering family who have encouraged me every step of the way. My mom and dad made many sacrifices to support my education, and this PhD work is certainly the fruit of their efforts. My aunt Marcia continually inspired my education and my fight for minorities inclusion with her own work. My caring siblings and best friends Fernanda and Luis Felipe always made sure I could count on them during the most difficult times. I am blessed to have them all in my life.

Finally, but certainly not least, thank you to my amazing husband and life partner, Vinnie, who showed me understanding when I was really stressed and could not focus on anything else. He continually supported me with his love, kindness, amazing food, prayers, and encouragement to complete this work. He and our adorable cats have provided me strength to continue pushing through the various obstacles I faced. I love you very much.

Table of Contents

List of Figures

List of Tables

.

List of Appendices

Abstract

Antibody-drug conjugates (ADCs) are a type of targeted therapy that combines the specificity of an antibody and a cytotoxic payload agent connected by a linker. The development of new ADCs has improved in the last few years with new ADCs being approved by the FDA and many others in the pipeline, but the failure rate for ADCs in solid tumors is still nearly 90%. One of the major problems is the limited ability of the ADC to penetrate into the tumor tissue; for example, the FDA-approved ADC Kadcyla® (T-DM1 targeted against HER2+ breast cancer) is localized only on tumor cells close to the blood vessel even at the clinical dose. As a result, many cells in the tumor do not receive any drug, influencing efficacy. In the clinic, it has also been found that the efficacy of T-DM1 and other ADCs is closely related to the expression of receptors per cell, making tumors with low receptor expression resistant to the treatment. Besides these challenges, several additional aspects of the tumor environment can influence efficacy such as variability in cancer cell dynamics (proliferation and death), blood vessel dynamics (angiogenesis), heterogeneous receptor expression, and intrinsic resistance.

New approaches to improve ADC treatment, such as coadministration of the ADC with its unconjugated antibody, fractionated dosing, and bystander payloads, have been proposed to overcome these challenges that limit the efficiency of ADCs as cancer therapeutics. These approaches have overlapping contributions to efficacy, and analyzing them experimentally is a difficult and time-consuming task that requires an impractical and unethical number of *in vivo* experiments. Developments in the field of computational modeling methods have enabled the

development of more sophisticated and mechanistic models that can capture the complexity of the tumor environment to predict ADC behavior in vivo.

In this thesis, I describe the use of a new hybrid agent-based model framework to mechanistically capture pharmacokinetics and pharmacodynamics of ADC treatment in solid tumors. I first describe the development of this new model that combines a commonly used deterministic Krogh cylinder tumor model with a stochastic agent-based model and show how it captures systemic, intratumoral, and single-cell dynamics that impact the overall drug efficacy. I also demonstrate how this model can be used to inform different dosing regimens, such as coadministration of ADC with its unconjugated antibody and fractionated dosing, by predicting tumor inhibition efficiency for each. I further extend the model capabilities to capture heterogeneity in receptor expression and intrinsic resistance by changing cell properties. I compare how different ADC dosing regimens influence the efficacy of ADCs containing bystander payloads, which possess the inherent ability to compensate for tumor heterogeneity. Finally, I apply this model to elucidate the in vivo behavior of a complex ADC currently under clinical evaluation in the complex tumor microenvironment of patient derived tumors.

In summary, I demonstrate a new approach to evaluate the pharmacokinetics and pharmacodynamics of ADCs from the perspective of varying dosing regimens, mechanism of action, and tumor microenvironments that can guide future experiments and improve the overall development of this drug class.

Chapter 1 Introduction

1.1 Motivation

Cancer is the second most deadly disease worldwide and is caused by mutations that lead to uncontrollable cell proliferation.[1] The most common treatment for metastatic cancer is still chemotherapy, usually accompanied by surgery for the complete removal of the tumor when possible. Chemotherapy is usually given intravenously with doses of potent chemical compounds that function to kill rapidly dividing cells, but this treatment also has harsh side effects as it subsequently attacks healthy cells. New therapies have been developed to improve targeting of cancer cells while reducing toxicity to healthy cells. Typically these therapies focus on increasing the therapeutic index by increasing the maximum tolerable dose (MTD) while reducing the minimum effective dose.[2, 3]

Antibody-drug conjugates (ADCs) are one type of targeted therapy for cancer. With nine Food and Drug Administration (FDA)-approved to date (Table 1), ADCs rank among the most actively pursued class of therapeutics in oncology.[4] A major limitation in the development of ADCs for solid malignancies is that they have an elevated failure rate of about 90% in the clinic.[5] These failure rates have been related to poor ADC distribution, complicated ADC pharmacokinetics (PK) and pharmacodynamics (PD), and the complex tumor environment. Only 0.001-0.01% of the injected dose of antibody reaches one gram of solid tumor in the clinic.[3] Understanding the mechanism and dynamics of these ADCs in the complex tumor environment could help us reduce the high failure rate in the clinic.

Table 1.1 ADCs FDA approved by 2020

Drug (Trade Name)	Maker	Condition	Year Approved
Gemtuzumab ozogamicin (Mylotarg®)	Pfizer/Wyeth	Relapsed acute myelogenous leukemia (AML)	2001^ Reapproved 2018
Brentuximab vedotin (Adcetris®)	Seattle Genetics, Millennium/Takeda	Relapsed HL and relapsed sALCL	2017
Trastuzumab emtansine (Kadcyla®)	Genentech, Roche	HER2-positive metastatic breast cancer (mBC) following treatment with trastuzumab and a maytansinoid	2013
Inotuzumab ozogamicin (Besponsa®)	Pfizer/Wyeth	Relapsed or refractory CD22-positive B-cell precursor acute lymphoblastic leukemia	2018
Polatuzumab vedotin (Polivy®)	Genentech, Roche	Relapsed or refractory (R/R) diffuse large B-cell lymphoma (DLBCL)	2019
Enfortumab vedotin (Padcev®)	Astellas/Seattle Genetics	Adult patients with locally advanced or metastatic urothelial cancer who have received a PD-1 or PD-L1 inhibitor, and a Pt-containing therapy	2019
Trastuzumab deruxtecan (Enhertu®)	AstraZeneca/Daiichi Sankyo	Adult patients with unresectable or metastatic HER2-positive breast cancer who have received two or more prior anti-HER2 based regimens	2019
Sacituzumab govitecan (Trodelv®)	Immunomedics	Adult patients with metastatic triple-negative breast cancer (mTNBC) who have received at least two prior therapies for patients with relapsed or refractory metastatic disease	2020
Belantamab mafodotin (Blenrep®)	GlaxoSmithKline	Multiple myeloma patients whose disease has progressed despite prior treatment with an immunomodulatory agent, proteasome inhibitor and anti-CD38 antibody	2020

Source: www.adcreview.com

^Mylotarg was withdrawn in 2010 due high toxicity and reapproved in 2018.

Efficacy for new drugs and regimens is typically tested using animal models, and these are very expensive and time consuming. Computational models have been developed to help understand factors determining drug and regimen efficacy, guide experiments, and accelerate the development of these and other drug classes. Although very effective in building an understanding of ADC distribution, most of these models do not capture essential features of the drug delivery in the complex tumor environment. These factors include single cell efficacy, blood vessel dynamics, heterogeneous tumor environment, the influence of ADC PK on PD and vice-versa, and others.[6, 7]

Here, I present a new hybrid agent-based systems pharmacology model that is the foundation of a new platform to elucidate their PKPD properties, predict the best regimens of ADCs, quantify their efficacy, and guide new experiments.

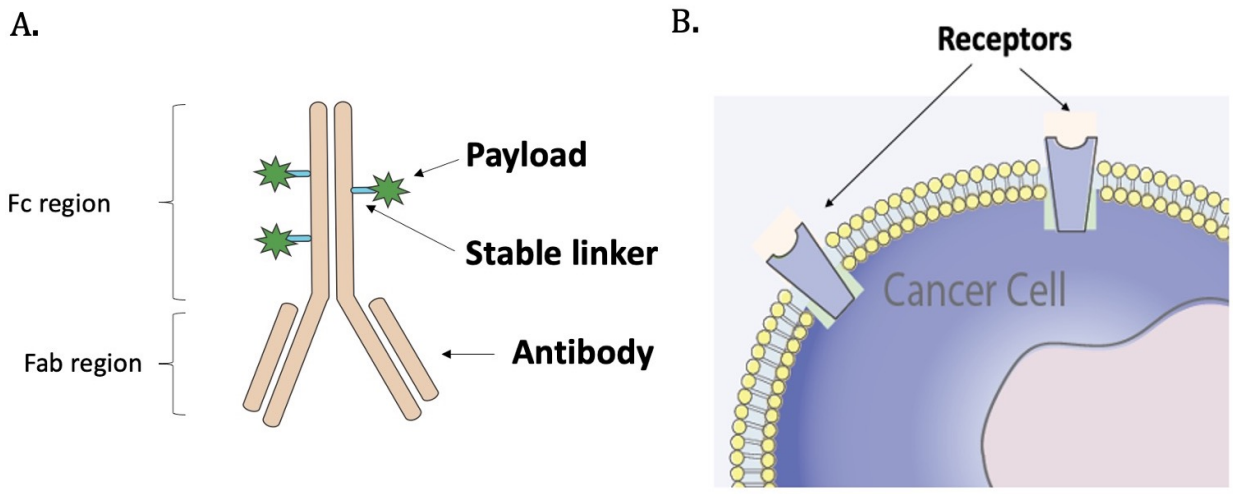

Figure 1.1 Antibody-Drug Conjugate Structure and Target Scheme
(A) ADCs are composed of an antibody back-bone, a toxic payload, and a linker. Antibodies have a Fc region that attracts immune cells, and the fab region contains the variable regions that bind to the receptors. (B) ADCs target receptors overexpressed on the cancer cell surface.

1.2 Antibody-Drug Conjugates

Antibody-drug conjugates are composed of three main parts: 1) antibody, 2) payload, and 3) linker (Figure 1). The antibody is responsible for binding to receptors that are overexpressed and/or selectively expressed on cancer cells. The payload is typically a very toxic drug that kills cells by interfering with cell proliferation via microtubule inhibiters, DNA crosslinkers, or DNA alkylators. The linkers connect the payload to the antibody, and they are usually classified as either non-cleavable, breaking this connection only after antibody degradation inside the cell, or cleavable, causing early release of the payload inside the cell and/or in the plasma and tumor environment.[8, 9] Following intravenous delivery, ADCs extravasate from blood vessels into the tumor tissue, diffuse through the interstitium, and bind to receptors on cancer cells. Once bound,

they are typically internalized and degraded in lysosomes, and the free payload or payload-linker compound binds to the cellular target to initiate apoptosis.

Target

The selection of the appropriate target is very important for the efficacy of ADCs, and factors such as expression, shedding potential, and internalization dynamics must be taken into consideration. Optimal targets must be overexpressed on the cancer cell surface and have reduced or absent expression on heathy cells. They must also not shed into the interstitial tissue causing off-target binding and a decrease in overall efficacy. Finally, receptors must be internalized to initiate ADC degradation in the lysosomes, making the payload free to kill cells.[10] For example, human epidermal factor receptor 2 (HER2) is overexpressed in about 25% of the cases of breast cancer, and it is currently the target of two FDA approved ADCs: trastuzumab emtansine (T-DM1, commercially known as Kadcyla® by Genentech, Roche) and trastuzumab deruxtecan (DS-8201, Enhertu® by AstraZeneca/Daiichi Sankyo). Another receptor that has been targeted in the clinic in solid tumors is guanylyl-cyclase C (GCC) found in colorectal cancer and GI malignancies. In this thesis, I focus on both HER2 and GCC targets.

Antibody

Antibodies are large proteins known as biologics that are produced by the immune system to contain foreign agents that are harmful to the body. These proteins can be engineered to bind cancer targets and used to deliver toxic drugs selectively to the cancer cells. The physicochemical properties of these antibodies of choice influence the pharmacokinetics of ADCs, and thus affect their distribution and uptake. Two major properties that affect distribution are affinity to target and

size.[11, 12] High antibody affinity to the targets is essential for the efficiency of ADC uptake by cancer cells, and the majority of the antibodies in the clinic have a binding affinity (K_d) usually from the sub-micromolar ($<10^{-6}$ M) to picomolar (10^{-12} M) range. For example, trastuzumab, an antibody that targets HER2 receptors, has a K_d of 0.5nM.[13] Antibody size is another important property for increased uptake of these biologics, and size can affect both systemic clearance and drug penetration into the tumor.[7, 12, 14] Full antibodies are known to have a long residence time with clearance half-life of several days, which is beneficial for uptake compared to small molecules that can be cleared in hours.[7] However, due to their lower diffusivity coefficient, high affinity to receptors, and lower dose, they do not diffuse deep into the intracellular tissue.[15, 16] Images of the distribution of fluorescently-labeled trastuzumab in xenograft mouse tumors show that most of the ADC is localized around the blood vessels and the drug permeates only a few cell layers.[17] The next generation of ADCs are finding ways to overcome this problem. For example, some agents use only the binding region of the antibody such as peptides (several kDa), antigen binding fragments (50 kDa Fab), single chain Fv fragments (25 kDa scFv), or single domain antibody fragments (15 kDa sdAb or V_H), instead of the full 150 kDa antibody.[18-20] To avoid quick clearance of these small fragments though renal filtration, a half-life extender can be attached to the molecule such as with Humanbody® created by Crescendo Biologics.[21]

Antibodies can also cause direct cell killing without the toxic payload through receptor signaling modulation and Fc-mediated immune cell recruitment.[20] Human antibodies come in several isotypes (IgG1, IgG2, IgG3, and IgG4), with IgG1 being the most common for ADCs. This isotype has a long circulation half-life, is easy to conjugate to linkers, and some can activate the immunoglobin receptors (FcγR). Binding to FcyR helps the engagement of antibody dependent cellular cytotoxicity (ADCC), antibody dependent cellular phagocytosis (ADCP), antibody

dependent cytokine release (ADCR), complement dependent cytotoxicity (CDC), and priming dendritic cells with neoantigens.[22] Immunotherapy approaches can further take advantage of these interactions using immune check point inhibitors to stimulate the immune system against antibody targeted cells, e.g. programmed cell death proteins on cancer cells and/or immune cells including PDL1, PD, and CTLA-4.[23]

Cytotoxic Payload

Payloads are the main driver of efficacy for ADCs. To achieve effective treatment, payloads must have high potency in the tumor, which is usually accompanied by high toxicity in healthy tissue. The payloads that are FDA approved in the clinic for example cannot be administered alone due to their low therapeutic index.[24] The main failure in the first ADC generation was indeed due to the low potency of the payloads as they were usually drugs already used in chemotherapies, e.g. doxorubicin.[25] The second generation, however, includes more potent payloads such as emtansine (DM1) and indolinobenzodiazepine DNA-alkylating (DGN). New and more potent payloads are still the focus of many researchers in the field to improve the therapeutic index.

Payloads in the ADCs usually affect microtubules, DNA, or replication machinery that are important for cell proliferation; therefore, affecting their function can potentially lead the cell to apoptosis, senescence, or necrosis.[3, 26] Some of the main classes of payloads include: microtubules inhibitors (auristatins and maytansinoids), topoisomerases inhibitors (SN-38), DNA-intercalators (camptothecin and anthracycline agents), DNA double strand breakers (calicheamicin), and DNA alkylators (pyrrolobenzodiazepine - PBDs and duocarmycin-hydroxibenzamide-azaindole, also

known as duacarmycin-DUBA).[27, 28] In this thesis, we will focus on auristatins, maytansionoids, and PBDs, and the reader is referred to [27, 29] for more information on other classes.

Payloads also have other requirements for efficacy such as a functional handle for payload after conjugation, stability and solubility in the plasma, hydrophobicity in conjunction with the drug to antibody ratio (DAR), cell killing potency, and small immunogenicity risk.[10, 27] Once conjugated to antibodies through a linker, the payload must not change the stability of the antibody in a way which results in faster clearance or premature release of the payload. Another factor that causes faster clearance is the number of payloads per antibody. As shown in Bender *et al,* the deconjugation rate of a single payload with a higher DAR is faster than the deconjugation of a single payload with lower DAR.[22] In addition, DAR and hydrophobicity of the payload are an important consideration that affects the distribution and penetration of ADCs into the tumor.[30] Lower DAR allows higher ADC doses, and the total antibody dose to payload uptake has shown improved responses in some ADC treatments.[14, 31] Hydrophobic payloads on other hand can diffuse through cell membranes, potentially reaching neighboring cells in a process known as bystander killing. These payloads that exhibit bystander effects could potentially improve distribution compared to more hydrophilic payloads that do not easily cross the cancer cell membrane.

Linker

The linker choice and conjugation to the antibody is fundamental for ADC kinetics, and there are cleavable and non-cleavable linkers. Cleavable linkers are used in the majority of ADCs, but they also have a greater risk of release outside the cancer cell in the plasma or interstitium. In contrast, non-cleavable linkers only release the payload after ADC degradation in the lysosomes

through enzymes (proteases) or pH-dependent degradation.[3] These linkers do not release the payload in its original form, and their use with payloads such as MMAE are not very practical since MMAE is most effective in its original form. Over the past years, extensive research has been focused on creating more stable linkers, but, counterintuitively, the unstable linker found in sacituzumab govitecan (IMMU-132), an ADC that targets trophoblastic cell-surface antigen (Trop2) found in many epithelial cancers, has been used with great efficacy in the clinic.[32] The reason for this ADC's success with an unstable linker is still not clear, and researchers are still trying to understand the advantages and disadvantages of each type of linker.

ADC Resistance

The development of ADC resistant mechanisms is a challenge in the field and can be due to low receptor expression, defective ADC and payload trafficking, efflux pumps, and others.[33] The most common form of resistance is a reduction in receptor expression. For example, down regulation of CD30 receptors in refractory Hodgkin lymphoma and anaplastic large cell lymphoma (ALCL) have shown to be the reason for resistance of the ADC Brentuximab vedotin.[34] In the clinic, variability of receptors is also found from cell to cell in the same tumor, and in a tumor with high overall average of receptors per cell, some cells have much lower receptor expression.[35-38] Finding ways to overcome this resistance through different regimens or ADC mechanisms has been actively pursued in the field.

1.3 Tumor Environment

The tumor environment is composed of many different cells, including proliferating tumor cells, tumor stroma, blood vessels, infiltrating inflammatory cells, and a variety of associated tissue cells, making it extremely complex and challenging for the delivery of drugs such as ADCs.[39-41]

When cancer cells grow uncontrollably, the intratumor pressure increases, preventing the penetration of fluids into the tumor.[42, 43] Molecules can only penetrate into the tumor tissue through diffusion, and large molecules such as biologics have low diffusivity coefficients, making this a barrier against ADCs. As cells proliferate and the tumor enlarges, access to oxygen also worsens causing cells to enter a hypoxic state and potentially leading to reduced drug sensitivity and cell death.

Cells in hypoxic states start releasing vascular endothelial growth factor (VEGF), a signaling protein that recruits more blood vessels to sustain tumor growth. The tumor vascular network, however, is differentiated from normal vasculature, and the blood vessels that are recruited are characterized by tortuous and leaky vessel walls with lack of pericytes, making them inefficient in delivering oxygen, nutrients, and other substances such as drugs. Previous works have targeted the tumor vasculature either by normalizing it and potentially increasing drug uptake in the tumor or by targeting these vessels to obstruct cancer cells' access to resources, preventing cancer cell growth.[44, 45]

The tumor environment is also composed of many immune cells whose presence can be correlated with good or poor prognosis, such as T lymphocytes, natural killer cells, macrophages, dendritic cells, and others.[39, 41, 46, 47] For example, cytotoxic T cells (CD8+) kill cancer cells and are supported by T helper cells (CD4+), and these are correlated with a good prognosis. Macrophages and natural killer cells (NK) also kill cancer cells through the process of ADCC. However, NK cells are scarce in the tumor environment, and tumor-associated macrophages (TAMs) are correlated with poor prognosis.[48] In particular, TAMs are thought to facilitate malignant cell migration, invasion, and metastases. Dendritic cells (DCs) are similarly complex in their effect. Even though DCs are important in antigen processing and presentation to other

immune cells' attacks, they have been shown to suppress T cell responses at the tumor site.[39] All these interactions between different cells in the tumor environment make it challenging to develop efficacious treatments that control the most important interactions of these cells, those that promote tumor progression.

1.4 Computational Models of Tumor Growth and Drug Delivery

Computational models capturing tumor growth and drug delivery are valuable to assist in approximating clinical doses, efficacy, and toxicity.[49-51] Here I present some of the most common models used to capture tumor volume and drug delivery for the predictions of clinical dose, drug clearance, and distribution.

Computational Models of Tumor Growth

The computational modeling of tumor growth has a long history.[52-57] Skipper's law is one of the oldest and most simplistic approaches to tumor growth and involves a set of relationships regarding the efficiency of chemotherapies.[58] Skipper's first law assumes that all cells are in a proliferative state with a particular cell doubling time. The tumor volume is calculated from the number of cells in the tumor, and tumor growth is captured by a logarithmic or exponential curve. The second law assumes that drug killing follows first order kinetics regardless of the tumor burden. However, tumors have been demonstrated to not possess a high proliferation rate, as they also have a resting state for which chemotherapies are ineffective.

Another older and famous model for tumor growth is the Gompertz model (Equation 1). The tumor volume curve of the Gompertz model follows a sigmoidal curve with a lower cell growth rate initially (avascular tumor formation), followed by a very fast or exponential growth rate (vascular tumor growth), and finally reaching a plateau which is assumed to be the maximum

tumor volume which kills the host (tumor saturation) (Figure 1.2). This model has been modified over time to take into account different dynamics and complexities of the tumor environment.[59] The tumor volume V at time t given by the Gompertz model is:

$$V(t) = V_{inj}e^{k(1-e^{-bt})} \quad (1)$$

where V_{inj} is the initial tumor volume at time $t_{inj} = 0$, b is a constant, and positive constant $k = log_e\left(\frac{V(\infty)}{V(0)}\right)$, regulating both growth rate and saturation size.

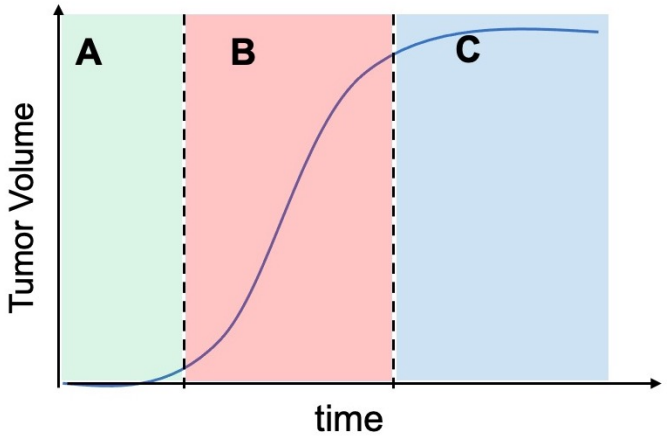

Figure 1.2 Gompertz growth curve
The Gompertz tumor growth model includes three phases. (A) Avascular tumor growth initiates with few cells and is characterized by slow growth. (B) Exponential curve representing the vascular tumor growth during which tumors have ready access to oxygen and nutrients after recruiting blood vessels. (C) Tumor growth reaches a plateau at which cells no longer have space and resources to grow or the tumor causes host's death.

More recent tumor growth models use ordinary and partial differential equations (ODEs and PDEs, respectively) to account for other tumor characteristics and dynamics such as cell cycle, oxygen and nutrient availability, necrosis, immune cell action, vascular characteristics, tumor-cell density, cell motility, and/or stress response.[60-64] Hybrid stochastic and deterministic models are becoming more common as these also capture the randomness of the biological systems and their intracellular interactions.[65, 66] In this thesis I develop a model platform that uses doubling time to

represent tumor growth and vessel density changes within the tumor volume to predict ADC delivery and efficacy. This platform also allows other important features to drug delivery to be added in the future.

Vascular Network Models

The tumor vasculature is part of the tumor environment, and its complex arrangement and dynamics, such as angiogenesis, are of great interest in computational research.[67-69] These models vary widely in complexity, from capturing only vessel density to capturing microvasculature details. As mentioned before, cells release signaling proteins to recruit new blood vessels, and these stimulate capillaries from parental vessels to sprout.[70] Pericytes and cell-cell junctions are loosened and endothelial cells become migratory. The endothelial cells proliferate quickly, and the sprouting tip extends until it connects to another parental vessel.

Tumor vascular network models can be represented by continuous, discrete, or hybrid models.[71, 72] The most important aspect for cancer treatment involves predicting angiogenesis, the spatial orientation of vessels, vessel permeability, vessel density change with tumor growth, and responses to anti-angiogenic treatments, as all these affect ADC delivery.[73] These different dynamics can be very computationally time expensive, and choosing how to simplify them, making appropriate assumptions to select only the important aspects of this complex system, is an important challenge for modelers when studying drug delivery.

Models for Drug Delivery and Distribution

Tumor growth models provide a description of how the tissue behaves in the absence of treatment. Pharmacology deals with the drug delivery, the pharmacokinetics (PK), and how the

drug exerts its effect, the pharmacodynamics (PD). In the body, drugs are absorbed, distributed, metabolized, and excreted (ADME), and different types of models can represent many of these details.[74, 75] The concentration and interaction with the drugs biological target then mediates an PD response, typically cell death in the case of ADC payloads.

Mathematical and computations approaches can capture a large range in size and dynamic scales, and these approaches can take many forms such as compartmental models, non-compartmental models, continuous and stochastic models, physiological/mechanistic models, and others.[76-79] Compartmental models dedicate each part to represent a space of interest such as different blood compartments, organs, or parts of the tumor, and the change of substances (e.g. oxygen, drugs, immune cells, etc) in these spaces as a function of time is usually determined with continuous equations.[80-82] For example, it is very common to use two or three compartment models to describe the absorption (for oral drug) and/or drug clearance in the plasma as a function of time and clearance parameters.[83, 84] In comparison, non-compartmental models are independent of the number of compartments and capture important drug considerations for patients such as the maximum plasma concentration (C_{max}), area under the plasma concentration-time curve (AUC), average drug concentration, apparent total plasma clearance (CL), elimination rate constant (k_{10}), half-life ($t_{1/2}$), and others.[77, 85] Nevertheless, mechanistic models are usually more complex and describe more specific details that represent drug distribution, and these can use continuous and/or stochastic approaches.

Mechanistic models are very common for drug delivery and capture details of drug transport such as drug diffusion into the body, binding to targets, internalization into cells, and intracellular metabolism.[86, 87] The Krogh cylinder model for example, originally developed by August Krogh in 1919 to study supply of oxygen in muscular tissues, has been used to capture the

distribution of ADCs from the blood vessels through the tumor tissue.[88, 89] This model has a small cylinder in the center representing the blood vessel, surrounded by a larger cylinder representing the tumor tissue (Figure 1.3). Combined with ordinary and partial differential equations, it describes each dynamic shown. Although the Krogh cylinder model represents ADC distribution around single vessels well, it does not capture other important features for drug delivery in solid tumors such as changes in blood vessel density, single cell drug uptake, single cell killing, angiogenesis, and the interplay of pharmacokinetics and pharmacodynamics. In this thesis, I utilize a multi-layered approach, connecting a two-compartment model to capture the drug clearance in the plasma, a more detailed mechanistic models to capture drug distribution through the tumor tissue and entering cell compartments, and a stochastic agent-based model to capture pharmacodynamics and the influence of the tumor environment.

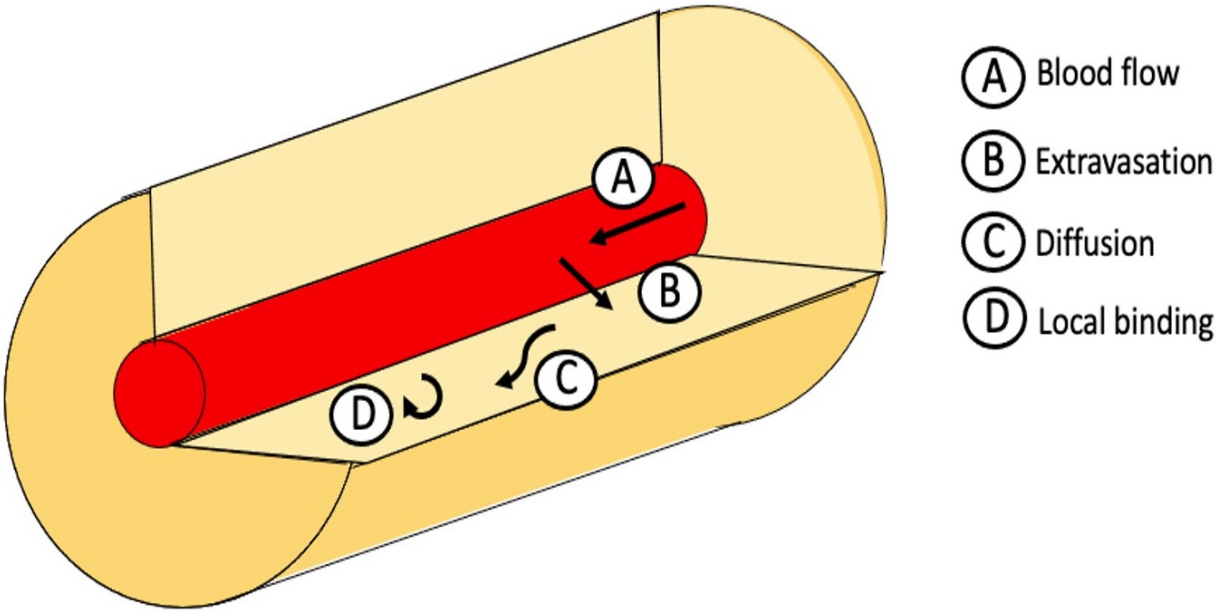

Figure 1.3 Krogh cylinder model
(A) ADCs flow through blood vessels, (B) leave blood vessel into interstitium tissue, (C) diffuse between cells, (D) and bind to antigens on the surface of cells.

1.5 Agent-Based Models

Hybrid Agent-Based Models (Hybrid-ABMs), a type of discrete model, have been used not only to describe the complex interactions between cells in cancer biology, but also in areas such as economics, sociology, criminology, epidemiology, immunology, and healthcare.[90-94] In systems biology, ABMs are often multiscale models that capture dynamics over different size and time scales.[95-98] ABMs are also discrete and stochastic, having defined agents that behave based on probabilities. These probabilities change based on the environment and on the behavior of other agents, making this a powerful model framework to capture the complex interactions that occur within the tumor and affect drug delivery.

ABMs can have agents with defined location determined by the modeler (lattice-based models) or be represented by volumes or masses (off-lattice methods).[99] In this thesis, I focus on lattice-based models only, and for a list of many models and open ABM sources toolkits, the reader can refer to Metzcar *et al*.[100] Both types of models can capture 2D or 3D dynamics, but lattice-based are usually easier to connect to PDEs to solve diffusion of molecules such as chemokines, oxygen, or drugs in the ABM environment.[101-103] Lattice-based models are beneficial for capturing single cell behavior in comparison with models that only take into account tumor volume or mass. Improving computational time for ABMs is still a hurdle. Because of ABM stochasticity, multiple simulations must be performed to study the average and ranges of model behavior, and, for example, a very descriptive 3D model with thousands of cells could take many hours to simulate. Another characteristic of ABMs that affects simulation time is the method of choice to solve the PDEs during diffusion on the environment grid compartments.[104] PDE solvers and time steps must be chosen to achieve accurate solutions. Small drugs, such as antibiotics, diffuse very quickly into the systems, and PDEs solvers can use relatively large time steps while the opposite occurs with

large molecules. In addition, large molecules such as biologics bind with high affinity to receptors on cancer cells causing them to have even smaller effective diffusivity and require small time steps for optimal solution. Consequently, simpler PDE solvers are not efficient to provide optimal solutions, and implicit methods or smaller time steps must be used. Even with these different challenges, however, ABMs are being increasingly utilized in the field.[105]

1.6 Thesis summary

In this thesis, I will present a new ABM as a new platform to help better predict distribution and efficacy of ADCs. In Chapter 2, I describe the development of the model and show how it can capture single cell dynamics that impact the overall drug efficacy. I also demonstrate how we used this model to predict different regimens' efficacy such as coadministration of ADC with its naked antibody and fractionated dosing. In Chapter 3, I extend the model capabilities to capture cell heterogeneity regarding receptor expression and intrinsic resistance. I compare how regimens with ADCs containing payloads that have bystander effects could potentially be effective in heterogenous tumors. In Chapter 4, I use this same model framework to help describe the experimental results of a new ADC that has a lipophilic payload in a system with lower receptors per cell. Finally, in the last chapter, I discuss future applications for this model and recommendations for the development of new ADCs.

Chapter 2 An Agent-Based Systems Pharmacology Model of the Antibody-Drug Conjugate Kadcyla to Predict Efficacy of Different Dosing Regimens

2.1 Publication Information

Menezes, B, C. Cilliers, T. Wessler, G. M Thurber, J. J. Linderman. *An Agent-Based Systems Pharmacology Model of the Antibody-Drug Conjugate Kadcyla to Predict Efficacy of Different Dosing Regimens. AAPS. 2020; J 22, 29.*

Modifications have been made to the published document to adapt the content to this text. The goal of this chapter is to develop a new complex agent-based model to better understand the efficacy of coadministration between T-DM1 and trastuzumab with different regimens including dose fractionation.

2.2 Abstract

The pharmaceutical industry has invested significantly in antibody-drug conjugates (ADCs) with increasing number of FDA-approved therapies and several more showing promise in late-stage clinical trials. The FDA-approved therapeutic Kadcyla (ado-trastuzumab emtansine or T-DM1) can extend the survival of patients with tumors overexpressing HER2. However, tumor histology shows that most T-DM1 localizes perivascularly, but coadministration with its unconjugated form, trastuzumab, improves penetration of the ADC into the tumor and subsequent treatment efficacy. ADC dosing schedule, e.g., dose fractionation, has also been shown to improve tolerability. However, the impact of coadministration with carrier doses in efficacy is still not clear in terms of receptor expression, dosing regimens, and payload potency. Here, we develop a hybrid

agent-based model (ABM) to capture ADC and/or antibody delivery and to predict tumor killing and growth kinetics. The results indicate that a carrier dose improves efficacy when the increased number of cells targeted by the ADC outweighs the reduced fractional killing of the targeted cells. The threshold number of payloads per cell required for killing plays a pivotal role in defining this cut off. Likewise, fractionated dosing lowers ADC efficacy due to lower tissue penetration from a reduced maximum plasma concentration. It is only beneficial when an increase in tolerability from fractionation allows a higher ADC/payload dose that more than compensates for the loss in efficacy from fractionation. Overall, the multiscale model enables detailed depictions of heterogeneous ADC delivery, cancer cell death, and tumor growth to show how carrier dosing impacts efficacy to design the most efficacious regimen.

2.3 Background

The number of approved antibody-drug conjugates (ADCs) has grown in recent years with nine ADCs approved by the Food and Drug Administration (FDA) and several more in late-stage clinical trials. However, developing effective ADC candidates for cancer therapy with a sufficient therapeutic index has been difficult, and several clinical failures of ADCs could have been avoided by minor improvements in the therapeutic window.[106] This is due to the highly complex ADC pharmacokinetics and pharmacodynamics in the tumor environment, especially for solid tumors. Ado-trastuzumab emtansine (T-DM1), commercially known as Kadcyla, is the first FDA-approved ADC for solid tumors, and only in 2020 the other three were approved: enfortumab vedotin, trastuzumab deruxtecan, and sacituzumab govitecan.

ADCs are composed of three main parts - a targeting antibody (Ab), a cytotoxic payload, and a linker connecting the two. These agents must be optimized to specifically deliver the payload

to cancer cells while minimizing healthy tissue uptake as they traverse multiple drug delivery barriers. After intravenous administration, ADCs flow through the blood to the tumor, extravasate from blood vessel, diffuse through the interstitial tumor tissue, bind antigens, are internalized by cancer cells, and, upon linker cleavage or digestion, release the cytotoxic payload that diffuses across membranes to their site of action (often DNA or microtubules) inside the cells. Tumors may vary in blood vessel density, receptor expression, and receptor internalization, all affecting ADC delivery.

ADC distribution in solid tumors is typically heterogeneous, which can impact efficacy.[14] Because of the large size of ADCs, uptake into the tumor is limited by extravasation from the blood to the tumor tissue (i.e., they are permeability-limited),[15] resulting in reduced amounts of drug in the tissue. Once in the tissue, tumor penetration is slow as a result of elevated interstitial pressure, making them reliant on diffusion through the interstitial space. ADCs rapidly bind to antigens surrounding tumor blood vessels and are typically internalized before they can dissociate and diffuse deeper into the tissue. For example, at clinical doses of 3.6 mg/kg, T-DM1 localizes perivascularly, as seen in multiple mouse models,[107] due to its large size and high affinity to HER2 receptors.

We and others have demonstrated that some ADC regimens can improve ADC distribution, efficacy, and tolerability. As previously established in our lab, the co-administration of T-DM1 with its unconjugated antibody, trastuzumab, improves drug penetration and efficacy.[31, 108] Other work from Hinrichs et al. and Jumbe et al. show that fractionating a single dose into 3 weekly doses can lead to similar efficacy, but better tolerability.[109, 110]

Despite these findings, the design principles underlying the best choice of regimen and drug combinations are not well-understood. For example, it is not clear if/when a 'carrier dose'

will increase drug penetration and improve efficacy. The impact of HER2 expression level and payload potency on the increase or reduction in efficacy from a carrier dose are also not well defined. Finally, the interplay of dose fractionation with carrier doses on overall efficacy is currently unknown.

Testing all combinations of receptor expression, payload potencies, carrier doses, dose fractionation regimes, etc. *in vivo* would be a daunting and expensive process. For this reason, computational models that guide experiments and predict best drug regimens are becoming more widely used. Computational models to capture the pharmacokinetics of ADCs are already established in the field,[111] [112] [113] [89] [114] but to our knowledge, there is not a pharmacokinetic/pharmacodynamic (PKPD) model of ADC distribution that captures the heterogeneous distribution of ADCs on individual cells to connect experimental single cell PK data to overall efficacy.

Here we took a systems pharmacology approach to study and predict the best ADC regimens. We developed a hybrid agent-based model (ABM) to capture ADC and/or antibody delivery and predict individual cell killing and tumor growth kinetics. This multiscale model enables detailed depictions of heterogeneous ADC delivery, cancer cell death, and tumor growth. Partial and ordinary differential equation models of ADC extravasation from multiple vessels, diffusion, binding, and processing are overlaid on a grid of individual cancer cells (agents). These cells undergo growth (cell division) and respond to the drug by cell death as a probability function of their intracellular payload concentration. Tumor growth rate is a function of the total number of cancer cells at a given time. The model was validated by comparison to experimental measurements in a HER2 positive NCI-N87 mouse xenograft model.[31] With this model, the role

of the carrier dose was analyzed, and predictions for the best regimen for different types of tumors overexpressing HER2 are presented.

2.4 Materials and Methods

We built a computational model to predict the efficacy of particular ADC regimens, accounting for ADC distribution in a heterogeneous tumor microenvironment. Our model is a hybrid ABM comprised of cancer cells and blood vessels that compose the tumor microenvironment and behave based on predefined rules and changes in their local microenvironment. The multi-scale model has portions that describe the tumor environment and PKPD: plasma dynamics, drug dynamics for T-DM1 and trastuzumab, and individual cancer cell dynamics (e.g., cell division, death) (Figure 2.1).

Simulation Environment

We simulate a subsection of a tumor and assume that i) the dynamics are representative of the entire tumor and ii) the tumor volume is proportional to the number of cells in the simulation. The model was simplified to a 2D representation because ADC concentration along the blood vessel is approximately constant (permeability limited).[15] The representative subsection of the tumor includes a zero net-flux boundary condition on its border. At low doses, few drug molecules reach the boundaries of the subsection, so the effects of the boundary conditions are minimal. At higher doses, a zero net-flux boundary condition is convenient to represent the equal diffusion of drug into and out of the subsection from adjacent regions of the tumor. Because antibodies are permeability limited, this changes the location of the cells that are targeted but has a negligible impact on the total tumor uptake or fraction of cells targeted by the ADC. Each simulation starts with approximately 2500 cells, which is used to represent an initial tumor size of 250mm^3. Cancer

cells and blood vessels each have different states, i.e., alive or dead for cells and functional and non-functional for vessels, and they occupy a position on the simulation grid. Their state changes during the simulation depending on their microenvironment. For example, a sufficient number of released payloads can kill a cancer cell or sufficient time allows the cells to proliferate. Blood vessel density and placement within tumors is highly variable (both between tumors and within the same tumor). To capture the heterogeneity in vessel distribution, each simulation has blood vessels randomly placed in the tumor space at its initialization, creating a different microenvironment for each cancer cell in the simulation. This variability can change the drug spatial distribution across cancer cells and consequently impact efficacy.

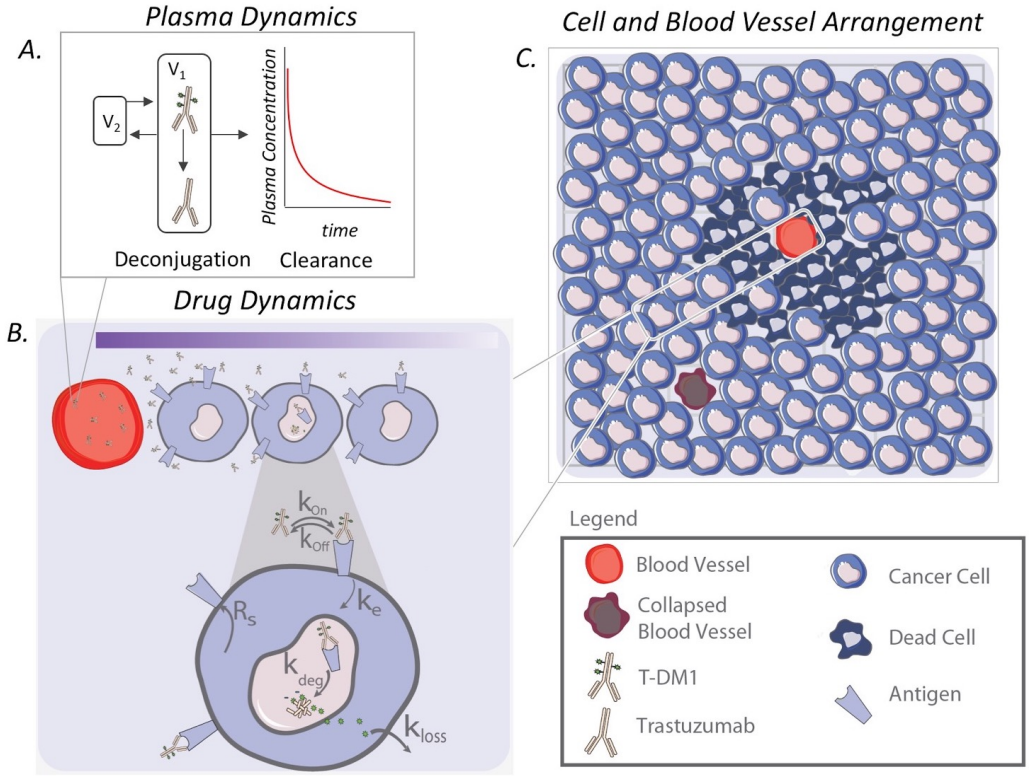

Figure 2.1 Model schematic
(A) Plasma dynamics describe the intact ADC concentration in the blood as a result of local and systemic clearance, including deconjugation. (B) ADCs in the blood extravasate from the blood vessel, diffuse through the interstitial tissue, bind to HER2 antigens, and are internalized. After ADC degradation in lysosomes, cytotoxins are released to kill the cell. (C) Individual cells and blood vessels are placed on a 2D lattice, forming the tumor environment.

Trastuzumab and T-DM1 Plasma Dynamics

The concentrations of trastuzumab and T-DM1 in the blood are a function of dosing, total antibody clearance rate, and payload deconjugation rate (rate at which the cytotoxin detaches from the antibody). A simplified ordinary differential equation (ODE) model from[22] to describe DM1 deconjugation was implemented here:

$$\frac{d[TDM1]}{dt} = -\left(\frac{CL_{TT}}{V_1} + \frac{CL_2}{V_1} + \frac{CL_{DEC}}{V_1}\right)[TDM1] + \frac{CL_2}{V_2}[TDM1_{p2}] \quad (3)$$

$$\frac{d[TDM1_{p2}]}{dt} = \frac{CL_2}{V_1}[TDM1] - \frac{CL_2}{V_2}[TDM1_{p2}] \quad (4)$$

$$\frac{d[Tras]}{dt} = -\left(\frac{CL_{TT}}{V_1} + \frac{CL_2}{V_1}\right)[Tras] + \frac{CL_2}{V_2}[Tras_{p2}] + \frac{CL_{DEC}}{V_1}[TDM1] \quad (5)$$

$$\frac{d[Tras_{p2}]}{dt} = \frac{CL_2}{V_1}[Tras] - \frac{CL_2}{V_2}[Tras_{p2}] \quad (6)$$

where $[TDM1]$ is the T-DM1 concentration in the central or plasma compartment (nM), $[TDM1_{p2}]$ is the T-DM1 concentration in the compartment 2 (peripheral tissue) (nM), $[Tras]$ is the unconjugated antibody concentration in the central compartment (nM), $[Tras_{p2}]$ is the unconjugated antibody concentration in the peripheral compartment (nM), CL_{TT} is the total antibody clearance (L/s), CL_2 is the antibody clearance for the peripheral compartment (L/s), CL_{DEC} is the deconjugation rate (L/s), V_1 is the volume of the central compartment (L), and V_2 is the volume of the peripheral compartment (L) as seen on Figure 2.1.A at clinical doses. CL_{TT} and CL_2 were calibrated to experimental data[115] as seen in appendix Fig A.1, and CL_{DEC} was set to be the same as CL_{TT}, making T-DM1 clearance twice as fast as trastuzumab clearance.[22]

Trastuzumab and T-DM1 Extravasation and Diffusion

Trastuzumab and T-DM1 extravasate from the blood vessels into the tumor, and this is described by a Robin boundary condition at the vessel boundary:

$$-\mathrm{D_{eff}}\frac{\mathrm{d[TDM1]}}{\mathrm{dx}} = \mathrm{P}([\mathrm{TDM1}]_{\mathrm{plasma}} - \frac{[\mathrm{TDM1}]}{\varepsilon}) \quad (7)$$

$$-\mathrm{D_{eff}}\frac{\mathrm{d[Tras]}}{\mathrm{dx}} = \mathrm{P}([\mathrm{Tras}]_{\mathrm{plasma}} - \frac{[\mathrm{Tras}]}{\varepsilon}) \quad (8)$$

where *x* is distance from the blood vessel (μm), P is permeability (μm/s), ε is fraction of free interstitial tissue, and D_{eff} is the effective diffusivity ($\mu m^2/s$), which describes the diffusion within the tissue.[6, 116] Because ADCs are large molecules that cannot traverse cell membranes, the use of ε here accounts for the accessible interstitial volume that ADCs diffuse through. This parameter also adjusts for the relative higher concentration of these molecules in the interstitium compared to an average tumor volume concentration.[12]

Diffusion of trastuzumab and T-DM1 on the 2D grid occurs according to Fick's law:

$$\frac{\partial C}{\partial t} = D(\frac{\partial^2 C}{\partial x^2} + \frac{\partial^2 C}{\partial y^2}) \quad (9)$$

where C is trastuzumab or T-DM1 concentration in (nM), t is time (s), D is the effective diffusivity ($\mu m^2/s$), x and y are the Cartesian coordinates. A zero net-flux boundary condition at the edges of the tissue was used since this is a subsection of a large tumor where edge effects are minimal.[117]

Trastuzumab and T-DM1 Binding, Internalization, and Degradation

Within the tumor, ADCs bind target molecules, are internalized, and after degradation in the lysosomes, payloads are released to kill the cancer cells through apoptosis as seen in Figure 2.1B. These drug dynamics are described by the following reactions:

$$\mathrm{TDM1} + \mathrm{HER2} \overset{\mathrm{k_{on}/k_{off}}}{\longleftrightarrow} \mathrm{B} \overset{\mathrm{k_e}}{\rightarrow} \mathrm{B_e} \overset{\mathrm{k_{deg}}}{\longrightarrow} \mathrm{Cytotoxin} \overset{\mathrm{k_{loss}}}{\longrightarrow}$$

$$\mathrm{Tras} + \mathrm{HER2} \overset{\mathrm{k_{on}/k_{off}}}{\longleftrightarrow} \mathrm{B_{Tras}} \overset{k_e}{\rightarrow}$$

$$\mathrm{HER2} \overset{k_e}{\rightarrow} \mathrm{HER2_e} \overset{k_{deg}}{\longrightarrow}$$

This results in the following equations:

$$\frac{d[TDM1]}{dt} = -k_{on}\frac{[TDM1]}{\varepsilon}[HER2] + k_{off}[B] \quad (10)$$

$$\frac{d[HER2]}{dt} = -k_{on}\frac{[TDM1]}{\varepsilon}[HER2] + k_{off}[B] - k_{on}\frac{[Tras]}{\varepsilon}[HER2] + k_{off}[B_{Tras}] + Rs - k_e[HER2] \quad (11)$$

$$\frac{d[B]}{dt} = k_{on}\frac{[TDM1]}{\varepsilon}[HER2] - k_{off}[B] - k_e[B] \quad (12)$$

$$\frac{d[B_e]}{dt} = k_e[B] - k_{deg}[B_e] \quad (13)$$

$$\frac{d[DM1]}{dt} = k_{deg}[B_e]\,DAR - k_{loss}[DM1] \quad (14)$$

$$\frac{d[Tras]}{dt} = -k_{on}\frac{[Tras]}{\varepsilon}[HER2] + k_{off}[B_{Tras}] \quad (15)$$

$$\frac{d[B_{Tras}]}{dt} = k_{on}\frac{[Tras]}{\varepsilon}[HER2] - k_{off}[B_{Tras}] - k_e[B_{Tras}] \quad (16)$$

All variables are listed on Table I and model parameters on Table II. Both free and bound HER2 receptors are assumed to be internalized with the same rate constant. We also assume that the total number of receptors on the cell surface remains constant due to new receptor synthesis and unbound receptor recycling. Thus, $R_s = k_{in}\,[HER2]_o$. Because the binding and dissociation reactions between the trastuzumab backbone and HER2 receptors are fast in comparison to internalization, we assumed a pseudo-steady state for binding in each compartment to reduce computational time.

Table 2.1 Drug Dynamics Variables

Variables	Unit	Description
TDM1	nM	Free T-DM1
HER2	nM	Free HER2
$HER2_e$	nM	HER2 in endosome
B	nM	T-DM1 bound to HER2
B_e	nM	T-DM1 bound to HER2 in endosome
DM1	nM	DM1
Tras	nM	Trastuzumab

Table 2.2 Model Parameters

Parameter	Value	Unit	Description	Reference
CL_{TT}	1.74×10^{-9}	L/s	Total antibody clearance	Estimated [115]
CL_2	2.31×10^{-8}	L/s	Antibody clearance for compartment 2	Estimated [115]
CL_{DEC}	1.74×10^{-9}	L/s	Deconjugation rate	Estimated [22]
V_1	1.2×10^{-3}	L	Volume central compartment	Estimated [115]
V_2	1.5×10^{-3}	L	Volume peripheral compartment	Estimated [115]
k_{on}	7.1×10^{5}	$M^{-1}s^{-1}$	T-DM1 binding rate constant	[13]
K_d	0.5	nM	T-DM1 dissociation constant	[13]
k_{off}	3.5×10^{-4}	s^{-1}	T-DM1 dissociation rate constant	[13]
k_e	3.3×10^{-5}	s^{-1}	Internalization rate constant	[7]
k_{deg}	8×10^{-6}	s^{-1}	T-DM1 lysosomal degradation rate constant	[111]
k_{loss}	3.94×10^{-5}	s^{-1}	Cytotoxin loss rate constant	Estimated [30]
DAR	3.5	-	DM1 to antibody ratio	[118]
R_s	2.75×10^{-11}	M/s	Target synthesis	[6]
$HER2_o$*	5×10^{4}-2×10^{6}	receptors/cell	Total targets per cell	Varied
ε	0.24	-	Intracellular void fraction	[119]
D	1×10^{-11}	m^2/s	Diffusivity	[6]
P	3×10^{-9}	m /s	Vascular permeability	[120]
P_{max}	0.014	-	Maximum probability for cell killing	Calibrated
K_m	800	nM	Michaelis-Menten constant	Calibrated
t_d (*in vivo*)	5-17	days	*In vivo* doubling time	Calibrated
t_d (*in vitro*)	1-2.5	days	*In vitro* doubling time	Estimated

*1 million receptors per cell corresponds to 833nM receptors where each cell occupies about 2×10^{-12} L.

Cell Division and Death

Tumor volume is proportional to the number of cancer cells in the simulation. Cancer cells proliferate depending on the tumor doubling time (t_d) assigned at the beginning of the simulation, and t_d is assumed to account for natural cell death. All cells in the same simulation are given the same doubling time but a different (random) birthtime to avoid synchronization. At cell division, two identical cells are created, and their bound drug and internalized drug are evenly divided between them. One of the daughter cells is placed in the original grid compartment, and the other daughter cells is placed on a neighboring grid compartment. If there is no space in the neighboring compartment, cells shuffle to make space for the new cell (see Appendix Fig. A.2).

Cancer cells die only depending on the payload concentration inside the cells, and they are then removed from the simulation grid. The probability for cell killing (P_{kill}) during each agent

time step (i.e., the integral of the cell killing rate over the time step) is given by the Michaelis-Menten equation:

$$P_{kill} = \frac{P_{max}\,[DM1]}{K_m + [DM1]} \tag{17}$$

where P_{max} is the maximum probability for cell killing, [DM1] is the concentration of cytotoxin inside the cells in nM, and K_m is the Michalis-Menten constant. P_{max} and K_m were calibrated to experimental data.[31] The overall probability for cell killing becomes the integration of all the probabilities for cell killing over the simulation time. While Eqn. 17 always has a probability of death > 0 for a non-zero payload concentration, in practice, low concentrations of drug typically exhibit a threshold effect below which no discernable difference between treated and untreated cells is seen. Therefore, we estimated the minimum concentration for cell killing (a cell killing threshold) to be 120 nM based on experimental data (Appendix Methods A.1).[31] If the payload concentration inside the cell is below this threshold, the probability for cell killing is set to zero. Trastuzumab was assumed to have no effect on cell killing, although very high doses of trastuzumab might have an impact on efficacy in an NCI-N87 xenograft model system. Dead cells were estimated to stay on the grid for 2.5 days (Appendix Fig. A.3.) before they are removed from the grid. Neighboring cells shuffle from the outer border to fill the empty grid space caused by the removal of the dead cell (Appendix Fig. A.2).

In Vitro Simulations

To model *in vitro* toxicity experiments, we assumed that all cells are exposed to the same external concentration of trastuzumab and T-DM1 present in the media. For this reason, ε is set equal to 1 in Eqns. 8, 9, 10, 13, and 14, as ADC diffusion is not hindered by the tumor tissue. For the toxicity assays, cells in each simulation are exposed to a constant T-DM1 concentration, and

cell viability was calculated at 6 days. For the coincubation of trastuzumab and T-DM1, cells were exposed to a total concentration of 10nM and various ratios of the concentrations of trastuzumab to T-DM1. For all *in vitro* simulations, cell doubling time was varied from 1 to 2.5 days.

Computational Environment and Numerical Methods

The model was constructed in C++ with Boost (distributed under the Boost software license – available at www.boost.org). The graphical user interface (GUI) was built using the Qt framework (open-source, distributed under GPL – available at qt.digia.com). Efficient linking and solution of our hybrid multiscale ABM followed the principles described in [104]. We used a molecular time step of 2 seconds, a diffusion time step of 4 seconds, and an agent time step of 10 minutes. The diffusion equation was solved using the alternating-direction explicit (ADE) method and ODEs were solved using the 4th order Runge-Kutta method.

Vessel Density Determination

To determine the number of vessels to include in simulations, we analyzed images of mouse tumor slices that were stained *ex-vivo* with CD31-AF555 to show blood vessels. Images were processed in MATLAB to find the vessel density.[31] Briefly, random lines are placed on the images, and the number of cuts is counted. Based on that, we can find the surface of the blood vessel over tumor volume ratio (S/V) from [121]:

$$\frac{S}{V} = \frac{2c}{Ln} \tag{18}$$

where c is the number of cuts, L is the length of the line (μm), and n is the number of the lines placed. Here we used $75\,\mu m$ for L and 10000 lines. To match experimental data, we determined 18 to 36 blood vessels per initial simulation area (S/V range from 23/cm to 45/cm) is

appropriate. In this model, the relationship between doubling time and vessel density was estimated as shown in appendix Fig A.4.

Fluorescence Histology

Methods for fluorescence histology have been published previously by our lab [31]. Briefly, for mouse tumor xenografts, $5x10^6$ NCI- N87 cells, purchased from ATCC, were injected in the rear flanks of 4-8-week-old female nude (Foxn1nu/nu) mice from Jackson Laboratories. Kadcyla was conjugated with AlexaFluor 680 NHS Ester (AF680, Thermo Fisher Scientific, A37567) with antibody to dye ratio of 0.3 or less and given intravenously. The mice were then sacrificed 24 hours after injection and histology slices were labeled ex-vivo with anti-mouse CD31 conjugated with AlexaFluor 555 (Thermo FisherScientific, A37571) and mouse antihuman IgG Fc antibody conjugated with AlexaFluor 488 (Thermo Fisher Scientific, A20000). All animal studies were conducted according to University of Michigan Institutional Animal Care and Use Committee.

2.5 Results

Simulating Heterogeneous Distribution of Antibodies in Tumor Slices

Our model captures the heterogeneous distribution of ADCs and antibodies seen in NCI-N87 tumor xenografts.[14] Here, vessel density varies between simulations following a normal distribution with an average blood vessel density of 28 functional vessels per simulation. At clinical doses (3.6 mg/kg), T-DM1 localizes perivascularly, but coadministration with trastuzumab competes for the perivascular binding sites, allowing more T-DM1 to penetrate farther in the tissue. Therefore, a constant dose of T-DM1 is ‘diluted’ in the tumor tissue to reach more cells as seen in images of mouse tumors (Figure 2.2.A). With the same image contrast for the same drug

regimens, our model also captures this dilution and spreading of ADCs in the simulation with T-DM1 reaching all cells at regimens of 8:1 ratio, Figure 2.2.

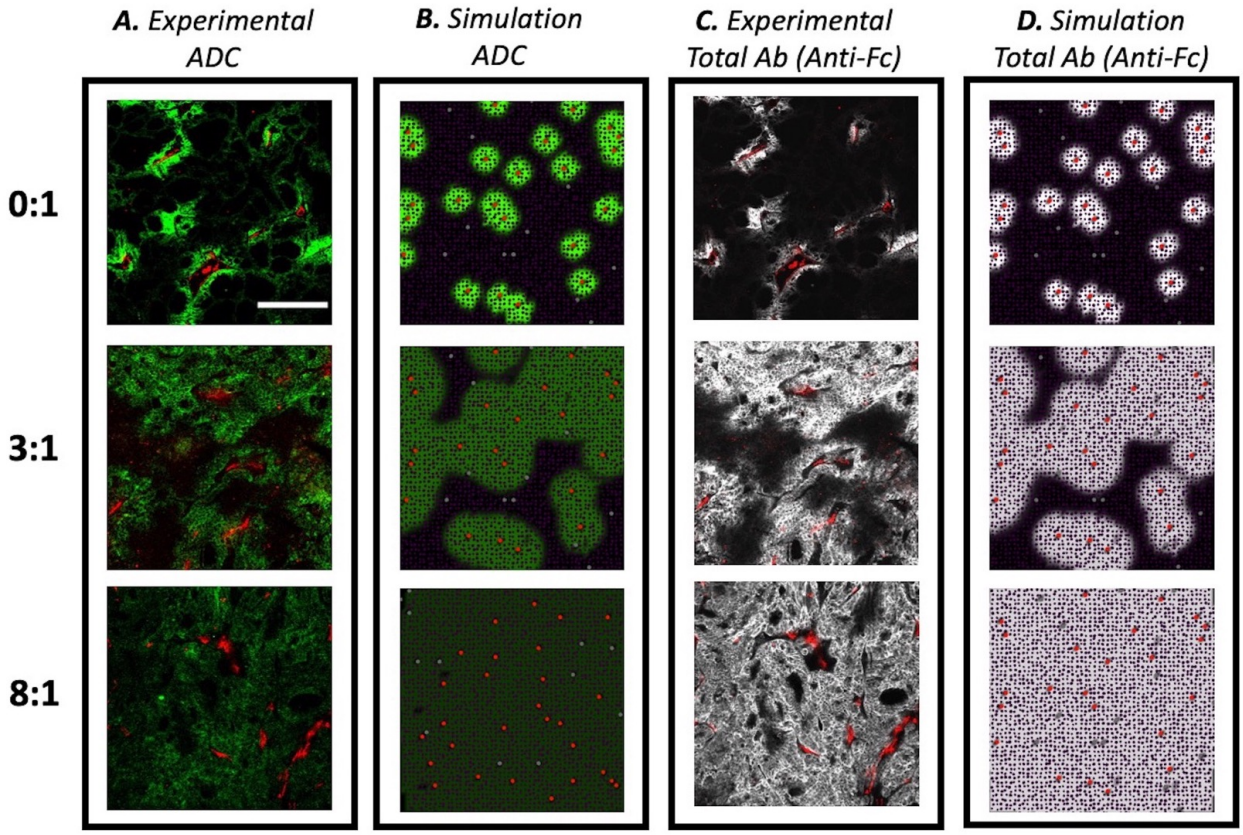

Figure 2.2 Comparison between experimental and simulated drug distributions in tumor tissue
(A) Tumor sections from mice bearing NCI-N87 xenograft tumors dosed with 3.6 mg/kg of AlexaFluor680 labeled T-DM1 and different ratios of trastuzumab:T-DM1 were imaged after 24 hours using the same settings and then set to the same window level for different carrier dose (trastuzumab) concentrations. T-DM1 intensity decreases as it is "diluted" with trastuzumab at higher ratios and spreads out to reach more cells. (B) Simulation results showing bound T-DM1. (C) The same tumor sections were stained with anti-Fc labeled antibody and window-leveled the same to show total drug penetration in tumor. (D) Simulation results show total antibody (T-DM1 + trastuzumab) penetration into the tumor. For all figure portions, scale bar = 200 μm.

Likewise, our model captures the total antibody uptake as seen in mouse tumor slices stained with antihuman-Fc labeling that targets all antibody backbones (T-DM1 and trastuzumab), methods found in previous work.[31] Here, although the concentration of T-DM1 is diluted through the tumor tissue, higher antibody concentrations are achieved with coadministration of

trastuzumab along with T-DM1 to improve tumor penetration. As seen on Figure 2.2.C and 2.2.D, our model also captures this total antibody uptake by the tumor reaching receptor saturation at the 8:1 ratio.

Calibrating Tumor Growth Kinetics and In Vivo Cell Killing

After demonstrating that the ABM can capture the heterogeneous distribution of antibodies and ADCs around vessels, we moved to capture the pharmacodynamics within the tumor. To understand how the drug microenvironment impacts efficacy, our model was calibrated to *in vivo* data[31] on cell proliferation and cell killing due to drug action to capture the tumor growth dynamics. The tumor growth rate for the simulations was calibrated by fitting the average tumor cell doubling time and range to capture tumor volume growth curves from experimental control (untreated) mice as seen in Figure 2.3.A and 2.3.B. The calibrated tumor volumes have a doubling time range from 5 to 17 days. In this model, the doubling time for each tumor is defined at the initialization based on a normal distribution in which tumors with higher vessel density have a higher probability to grow faster (i.e., a smaller doubling time, appendix Fig. A.2). This was implemented to account for the blood vessels as the source for nutrients and oxygen that enables cell proliferation.[122] The proliferation rate constitutes the net cell division above the level needed to replace intrinsic cell death within the tumor.

The probability of cancer cell killing due to drug action was also calibrated to the *in vivo* experimental data for T-DM1 treatment at the clinical 3.6 mg/kg dosing. Using the Michaelis-Menten equation for the killing probability, the average efficacy in 10 experimental mouse tumors was matched to the average efficacy of 100 simulations. P_{max} and K_m are highly correlated and are mostly in the linear range of Eqn. 17 for these simulations, so we set K_m to 800nM based on

the likely range of payload concentration inside of the cell and calibrated P_{max} to 0.014. Using these two parameters, cell killing results matched the range and average as seen of Figure 2.3.C and 2.3.D.

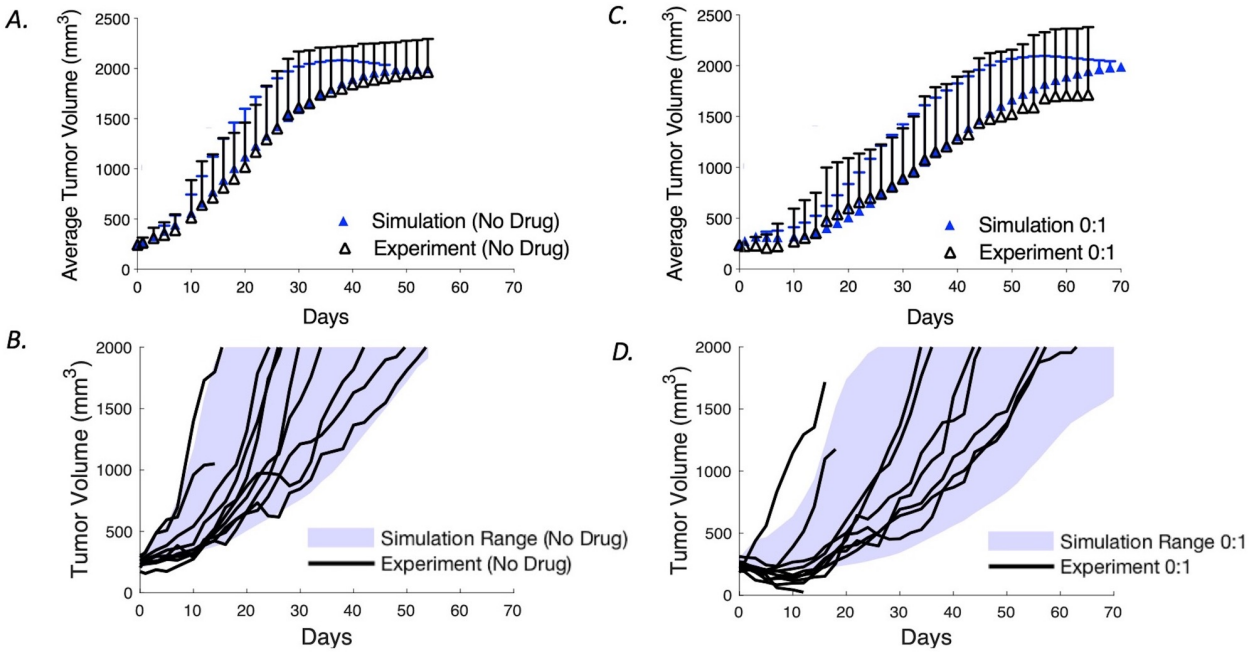

Figure 2.3 Model calibration of tumor growth rate and cell killing using average and variability of NCI-N87 xenograft efficacy
(A) The average experimental data and SD are plotted with the average and SD of simulated tumor sizes from 100 computational runs for the control group. (B) The range of growth rates for the simulations (shaded area) is shown together with individual tumor curves in the absence of drug treatment. (C) The average experimental data and SD are plotted with the average and SD of calibrated tumor sizes for a single dose. To calibrate cell killing in vivo, the growth curves for tumors treated with 3.6 mg/kg of T-DM1 were used to calibrate the probability of individual cell death as a function of intracellular payload concentration (Eq. 15). (D) The range of growth rates for the simulation (shaded area) is shown together with individual experiment curves for a treatment with a single dose.

Simulation Accurately Predicts the Effect of Coadministration of Trastuzumab with T-DM1 on Tumor Growth

Previously, our lab demonstrated that coadministration of trastuzumab and T-DM1 improved efficacy. Using the model that was calibrated to data from a single dose of T-DM1, we

next simulated regimens for 1:1, 3:1, and 8:1 ratio and compared the results to the experimental curves for model validation (Figure 2.4.A-C). The mean tumor volumes and SD of the simulations (n=100) agree closely with the experimental data (n=10). Figure 2.4.D-F shows the simulation range achieved with the 100 simulations (blue shading) and the experimental tumor curves (black lines).

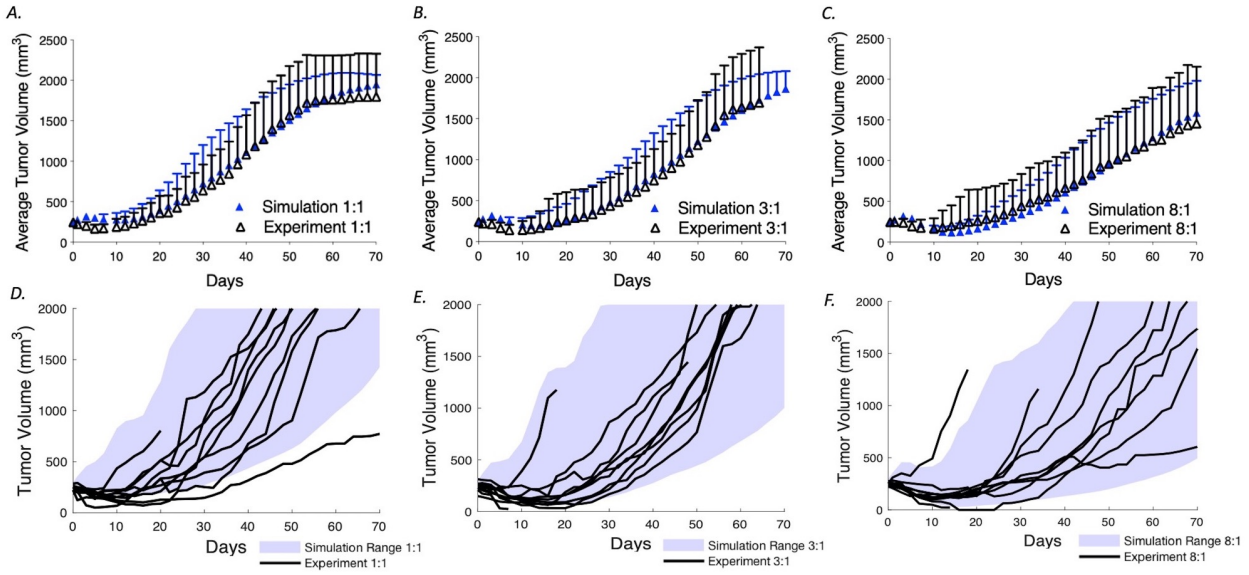

Figure 2.4 Coadministration of T-DM1 with trastuzumab
Using the calibrated tumor growth and cell killing probabilities determined in Fig. 2.4, the model was used to predict the tumor growth curves for mice treated with 3.6 mg/kg T-DM1 with trastuzumab to T-DM1 ratios of 1:1, 3:1, and 8:1. These independently generated simulations were then compared with the experimental data from Cilliers et al. (A–C) Mean and SD of the experimental and simulation data. (D–F) Simulation ranges (shaded area) and the experimental tumor volume curves (black lines).

Reaching Maximum Number of Cells with Lower but Lethal Concentrations of Payload Results in the Greatest Tumor Efficacy

We next simulated drug regimens with different ratios of trastuzumab to a fixed clinical dose (3.6 mg/kg) of T-DM1 to identify which dose regimen gives the best treatment outcome. Figure 2.5.A-D shows the efficacy of regimens with trastuzumab to T-DM1 ratios ranging from 0:1 to 24:1 and over the course of 21, 30, 40, and 50 days. Increasing the ratio results in greater

competition of the unconjugated antibody to ADC. At a regimen of 8:1, the tumor approaches saturation by the antibody, and the maximum tumor uptake of T-DM1 reaches all of the cells within the tumor. At higher than saturating (super-saturating) doses, the unconjugated antibody competes with T-DM1, decreasing the uptake of payload into individual cells, while not reaching any more regions of the tumor. Both total tumor uptake of ADC and individual cell uptake decrease beyond this point. When graphing the fraction of cells receiving a given intracellular payload concentration for increasing carrier doses at 48 hrs, both the number of cells with very high levels of payload and those with no payload are reduced (Figure 2.5.E) while more cells receive a moderate dose of payload (i.e., reducing the heterogeneity of drug distribution). Importantly, even at the 8:1 carrier dose, ~60% of the targeted cells have greater than the 120 nM intracellular concentration needed for cell death. However, as the carrier dose increases, the concentration of the payload decreases below 120 nM, resulting in reduced efficacy. In summary, despite competition of T-DM1 uptake by the large antibody dose, the model predicts a better prognosis when more cells are reached at a lower (but still lethal) number of T-DM1 payloads per cell than when fewer cells receive high doses (‘overkill’).

The Potency of the Payload Affects the Influence of a Carrier Dose

The simulations indicated that a carrier dose improves efficacy when the increased number of cells reached by T-DM1 outweighs the reduced killing due to fewer payloads per cell. Implicit in this statement is that adding a carrier dose beyond the level needed for tumor saturation will lower efficacy since no new cells are reached. In the system studied here (T-DM1 with NCI-N87 xenografts), the payload is very potent relative to the number of payloads delivered per cell, and the doses are below tumor saturation. However, for moderately potent payloads, there are

examples where concentrating the payload on fewer cells results in greater efficacy[14] such as seen with sacituzumab govitecan.[123] If the concentration of the payload delivered by pure ADC is just enough to kill these cells (i.e., there is no 'overkill'), decreasing the concentration of the payload per cell with a carrier dose would lead to lower treatment efficacy because no cells would receive a toxic dose even though the new regimen is reaching more cells. To determine when a carrier dose might decrease efficacy even prior to tumor saturation, we used the simulations to examine the role of the minimum concentration needed for cell death (C_{min}).

The presence of a minimum threshold payload concentration for cell death has a significant impact on efficacy, particularly when the dose range is high enough to saturate the first cell layer but lower than required for tumor saturation. In this range, such as simulated in this work, the dose has a major impact on tissue penetration. We simulated tumor efficacy with a C_{min} of 500nM, 10nM, and no minimum threshold in toxicity needed for cell death (Appendix Fig. A.5). The latter scenario assumes a pure Michaelis-Menten relationship where any drug concentration, no matter how small, has some impact on cell viability. If this were the case, the carrier dose is virtually always beneficial prior to saturation of the tumor. This can be explained in terms of the number of cells reached and probability of cell death. If efficacy is the product of the number of cells targeted by the ADC multiplied by the fractional cell killing, the number of cells reached increases linearly with the total antibody dose. The fractional cell killing for payload concentrations well below the K_m results in close to, but always slightly less than, a linear decrease. Therefore, a carrier dose would always improve the overall product under these assumptions. However, most drugs exhibit some threshold below which there is no detectable response, so it was important to explicitly define a minimum concentration needed for cell death regardless of the pharmacodynamic model used

(including the Michaelis Menten model in this work). If a carrier dose reduces the payload uptake below this amount, a dramatic loss in efficacy is seen.

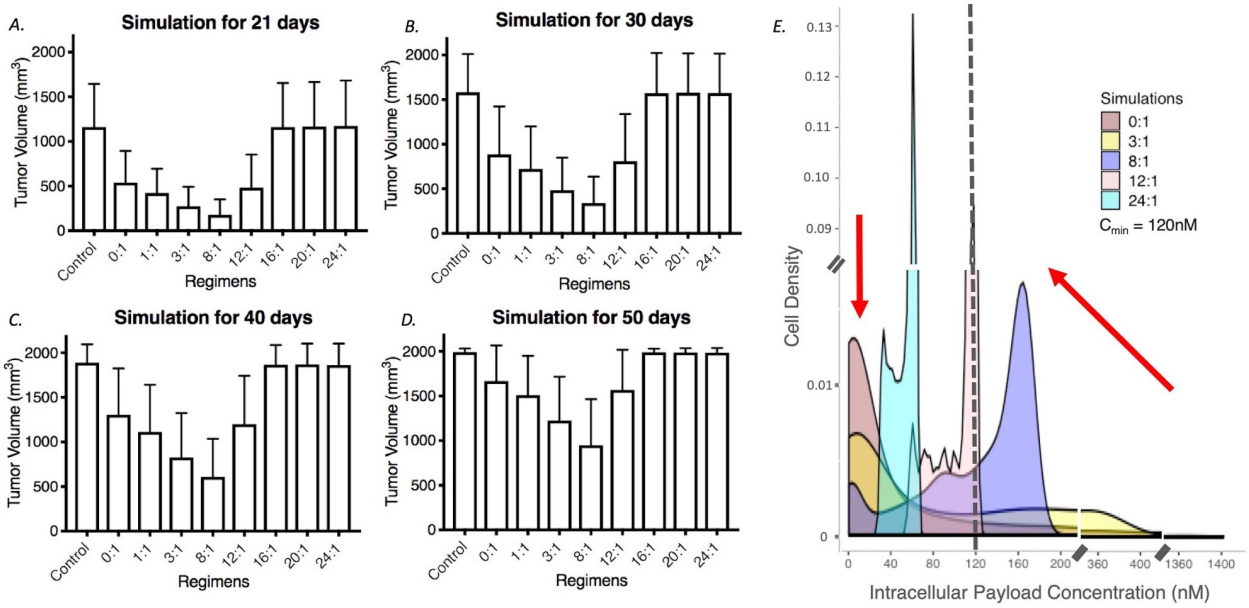

Figure 2.5 Influence of carrier dose on tumor efficacy
(A-D) The simulated efficacy of coadministration of trastuzumab with T-DM1 at 21, 30, 40, and 50 days, respectively, is shown for 3.6 mg/kg T-DM1 and trastuzumab to T-DM1 ratios from 0:1 to 24:1. Efficacy drops at higher concentrations of trastuzumab due to tumor saturation and/or reducing the number of payloads per cell below the threshold needed for cell death. N = 100 simulations for each bar. (E) Density plot for cells in the simulation (live or dead) receiving particular intracellular payload concentrations was calculated at 48 hours. Here, the area under the curve of the density function represents the probability of getting an intracellular payload concentration value between a range of payload concentration values. The number of cells that receive no drug decreases (arrow on the left) with an increasing carrier dose increase evidencing an improvement in distribution. However, the payload concentration per cell decreases with an increasing carrier dose (arrow on the right)

To simulate cells that are more resistant to the payload (i.e. the potency is decreased), C_{min} was set to a 500 nM intracellular concentration needed to induce some cell death. In this case, even a 1:1 carrier dose starts to decrease overall efficacy (appendix Fig. A.5). This highlights how diluting the ADC to achieve better drug penetration depends on the potency of the payload to reach a minimum threshold while reaching the largest number of cells.

The Impact of the Carrier Dose is Dependent on the Average Tumor Expression of HER2

ADC distribution within a tumor also depends on the number of receptors per cell.[89, 31, 30] As seen in previous work, a higher number of receptors decreases drug penetration into the tumor, and for those tumors, higher doses of coadministrated trastuzumab are needed to improve efficacy compared to tumors with lower receptor density. For this reason, the optimal drug regimen is dependent on the average number of receptors per cell in the tumor.

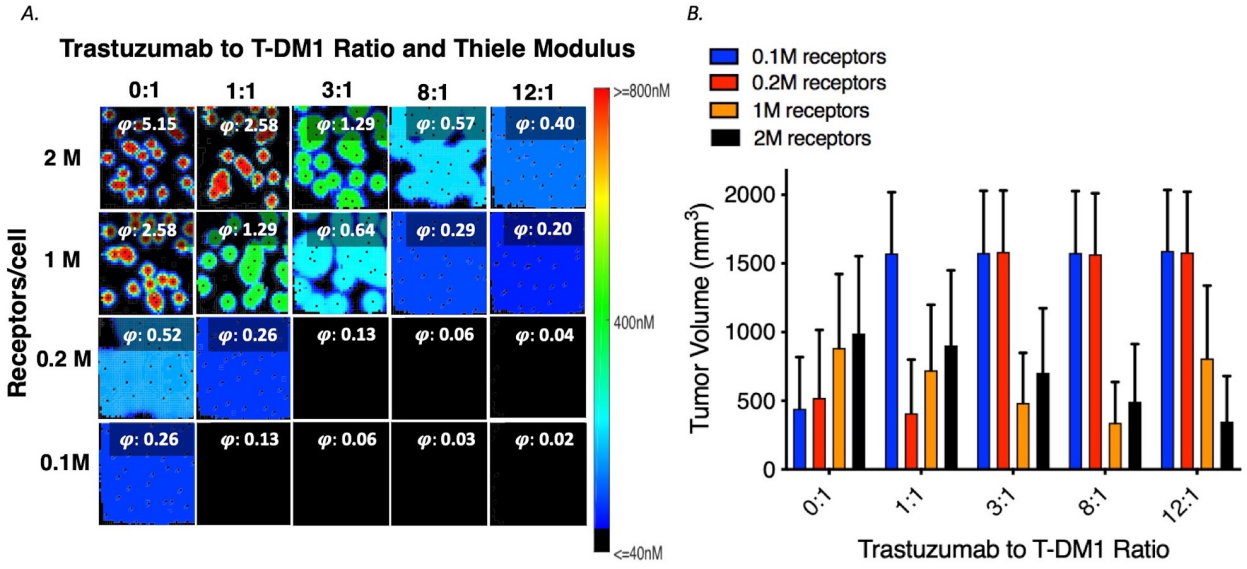

Figure 2.6 Interplay of dose and receptor density.
(A) Bound concentration of T-DM1with coadministration with trastuzumab (ratios trastuzumab to T-DM1 from 0:1 to 12:1) for tumors with different receptor densities. The Thiele modulus (calculated using total antibody dose) shows saturation when the value is less than ~ 0.2. (B) Average tumor volume at 30 days for different treatment regimens and tumors with different average receptor densities. The optimal carrier dose is dependent on receptor expression with higher trastuzumab doses needed for higher receptor expression. With the potency of this ADC, no efficacy is seen below 50,000 HER2/cell (Appendix Fig A.6).

Tumors with different HER2 receptor expression levels were simulated with various drug regimens, and the results are shown in Figure 2.6.A. Regimens with doses of trastuzumab and T-DM1 at 0:1, 1:1, 3:1, 8:1, and 12:1 were simulated for tumors with average of 0.1, 0.2, 1, and 2 million receptors per cell. The Thiele modulus, a dimensionless number that predicts the antibody

saturation level in tumors [7] is listed in each box. For levels below ~0.2 the tumor is saturated.[2] For tumors with lower HER2 expression, e.g. an average of 0.1 million receptors per cell, the best efficacy occurs at lower total antibody concentrations. However, at very low receptor expression levels, such as < 50,000 HER2 per cell, no response was observed as the minimum accumulation of payloads inside the cell to lead to efficacy is not reached (appendix Fig A.6). For tumors with higher expression density (e.g., 2M receptors per cell), the best treatment with coadministration occurs at higher doses of total antibody. However, at lower receptor expression, increasing the total antibody coadministered can actually decrease efficacy (Figure 2.6.B).

Single Dosing with Coadministration is Better than Coadministration with Fractionated Dosing

Previous work has demonstrated that fractionated doses can lead to similar efficacy, but better tolerability compared to single dosing. We simulated fractionated dosing treatment with 3 weekly doses of 1.2 mg/kg of T-DM1 and compared it with a single dosing (3.6 mg/kg). The maximum concentration (C_{max}) of single dose antibody in the plasma (3.6 mg/kg) is much higher than the C_{max} of fractionated dosing as shown in Figure 2.7.A. However, the area under the curve (AUC) for these two regimens is the same. With the same total administered dose at the end of 3 weeks, the efficacy of fractionated dosing is reduced but not significantly different than a single dose as shown on Figure 2.7.C. This is in agreement with reports by Hinrich et al. and Jumbe et al. showing lower efficacy when fractionating an ADC dose,[109, 110] but not significant differences in the case of Hinrich *et al*.

We also simulated single dosing and fractionated dosing for different carrier dose regimens of 1:1, 3:1, and 8:1 as shown in Figure 7.B-F. Here, for example, an 8:1 fractionated dose is equal to 3 weekly doses of 1.2 mg/kg T-DM1 coadministered with 9.6 mg/kg of trastuzumab. Our results

predict that at higher carrier doses (e.g. 8:1), dose fractionation results in much lower efficacy than for single dosing regimens with the same carrier dose. Although more cells are reached by the higher total antibody dose, e.g. 8:1 regimen, the lower T-DM1 concentration in each dose plus the dilution that occurs by adding a carrier decreases payload concentration per cell below the minimum needed for efficacy

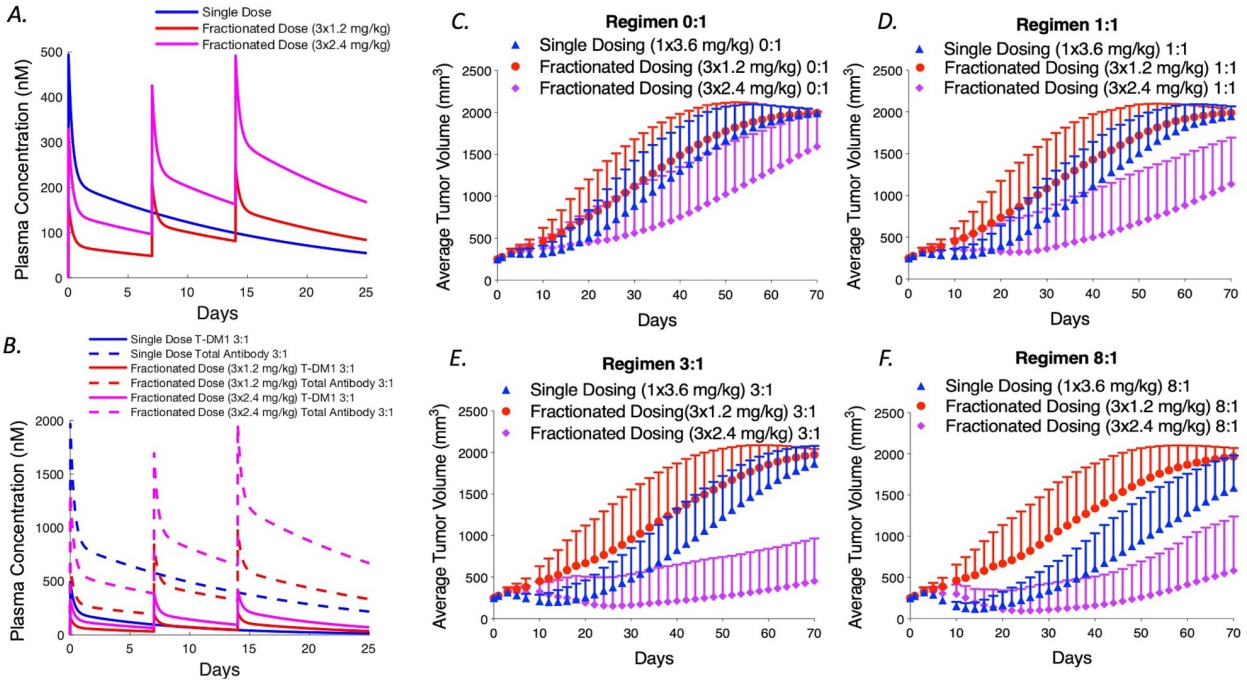

Figure 2.7 Simulations of fractionated dosing with and without a carrier dose for NCI-N87 tumor xenografts.
(A) Plasma concentration of T-DM1 for a single 3.6 mg/kg dose or 3 fractionated doses at 1.2 and 2.4 mg/kg. (B) Single T-DM1 versus total antibody concentration clearance for single and fractionated dosing at 3:1. (C–F) Simulated tumor volumes for the coadministration of trastuzumab to T-DM1 at 0:1, 1:1, 3:1, and 8:1 ratios are shown, respectively. Each plot compares a single bolus dose of 3.6 mg/kg to 3 weekly fractionated doses at 1.2 and 2.4 mg/kg T- DM1. In general, fractionation lowers efficacy due to reduced tissue penetration. This is exacerbated with high carrier doses (e.g., 8:1) because the lower payload delivery is significantly diluted below a threshold needed for cell death. This can be compensated, however, by increased tolerability if a reduction in toxicity allows larger ADC doses to be administered (e.g., 2.4 mg/kg weekly versus 3.6 mg/kg every 3 weeks).

One benefit of dose fractionation is greater tolerability. In the clinic it has been shown that the maximum tolerable dosing for T-DM1 is 3.6 mg/kg every 3 weeks or 2.4 mg/kg every week.[124] We therefore simulated weekly doses of 2.4 mg/kg T-DM1 with different carrier levels, which led to better predicted efficacy. With regimens of 2.4 mg/kg every week for 3 weeks, the total T-DM1 concentration is increased. Therefore, fractionated dosing with a carrier dose can be beneficial if this allows an increase in the total ADC dose reaching more cells with a lethal concentration of payload.

Model Calibration in Vivo Matches Drug Efficacy in Vitro

The pharmacodynamic model, calibrated to the *in vivo* data, also captures the toxicity of *in vitro* experiments (appendix Fig A.7). Originally, the pharmacodynamic model parameters were fit to *in vivo* data (Fig. 2.3.C-D) because it was not clear if the sensitivity of the cells in the tumor microenvironment would be different than in cell culture. Using the same parameters for *in vivo* calibration to simulate toxicity curves *in vitro* (either single-agent or coincubation of trastuzumab and T-DM1), the curves were similar to previously published results in our lab. Therefore, in this system, there did not appear to be a major shift in potency *in vitro* versus *in vivo*.

2.6 Discussion

The complexity of ADC development, encompassing the antibody design, target selection, linker development, payload potency, dosing regimen, along with delivery barriers, tumor heterogeneity, patient variability, and potential for drug combinations, requires tools beyond cellular and animal efficacy-based screening to efficiently identify compounds and drug regimens for clinical success. Agent-based modeling is a powerful tool to capture both the multiscale and

heterogeneous distribution of ADCs within tumors and also single cell responses and overall tumor efficacy (Fig. 2.1). A significant advantage of the current ABM model compared to previous ADC models is the ability to look at individual cellular responses for simulating pharmacodynamics, unlike our previous Krogh cylinder model which mainly captures pharmacokinetics. Here, we simulate the tumor environment in the context of many irregularly placed blood vessels, with some functional while others are not, capturing the irregularity seen in experimental data (Fig. 2.2).

Another advantage of the ABM is the ability to capture the cellular level pharmacodynamic behavior of ADCs. Recent advances in pharmacodynamic modeling of ADCs have started incorporating tissue gradients[89] or cellular heterogeneity (e.g., antigen positive and negative cells).[112, 80] In the current model, by simulating individual cells within tissue-scale drug gradients, we capture both these effects across thousands of cells. An ABM enables direct comparisons between single cell PK/PD data gathered in the lab and the computational model.

Treating a solid tumor as a homogeneous unit could overlook important effects of drug treatment regimens such as adding a carrier dose. Here, our model captures the correct drug distribution and efficacy of different regimens as compared with *in vivo* data from our lab (Fig. 2.2, 2.3, and 2.4), demonstrating that our model is a powerful tool to capture ADC and antibodies administration in the tumor environment.

The simulations also provide a series of predictions (Fig. 2.5, 2.6, and 2.7) that can aid in the development of drugs and design of new experiments. Although achieving greater tissue penetration (up to tumor saturation) has been shown to improve efficacy for tumors with high antigen expression treated with T-DM1, increasing the total antibody dose too much can also diminish cellular cytotoxin uptake and therefore lower efficacy (Fig. 2.5A-D). These results are dependent on the delivery (antigen expression, internalization rate, tumor vascularization, etc.) and

payload efficacy (linker cleavage, payload potency, etc.) necessitating a quantitative analysis for each individual ADC case rather than extrapolating the model results to all systems.

In addition to the payload potency, another important consideration in adding a carrier dose to the regimen is the average tumor target expression. For tumors with lower antigen expression, adding a carrier dose results in no improvement, and potentially lowers the efficacy. This is seen for regimens in tumors with lower antigen expression such as ≤ 100,000 receptors per cell. In these tumors, single-agent ADC dosing at 3.6 mg/kg already saturates the tumor, delivering the maximum cytotoxin potency to the tumor cells (Fig. 2.6). Adding a carrier dose to those tumors can only reduce the concentration of payload per cell. However, for even lower antigen expression such as 50,000 receptors per cell, even with ADC alone, there is not enough payload per cell to cause a tumor response (appendix Fig A.6). For this reason, administering a carrier dose must be considered in the context of the target's average tumor expression and payload potency.

A major consideration in the development of ADCs is the drug to antibody ratio.[125] T-DM1 has an average DAR of 3.5, but adding a carrier dose reduces the average DAR in circulation (e.g., DAR 3.5 at 3.6 mg/kg compared to DAR 1.75 at 7.2 mg/kg dose – or 1:1 regimen). Lowering the DAR allows higher antibody doses because toxicity is typically driven by the payload dose. In the absence of DAR-dependent effects (such as DAR-dependent clearance and DAR-dependent deconjugation),[126] lowering the average DAR by adding unconjugated (DAR 0) antibody is equivalent to lower the DAR of the ADC alone. However, DAR-dependent effects could lead to higher ADC exposure (AUC) for a lower DAR on the ADC compared to adding a carrier dose. The lower ADC DAR could improve efficacy by increasing tumor exposure from a higher AUC, but it also has the potential to change the toxicity profile (e.g., less deconjugation resulting in higher exposure to tissues such as the eye). Conversely, increasing the DAR of an ADC is expected

to increase the toxicity (at a constant antibody dose), lowering the maximum tolerated dose (MTD). The lower antibody dose can result in challenges such as target-mediated drug disposition and increased intratumor heterogeneity, which can reduce efficacy. Interestingly, some site-specific conjugation strategies result in lower DAR,[127] and lower potency payloads (e.g., topoisomerase inhibitors) also allow higher antibody doses to be administered, which can result in improved tissue distribution at the MTD.

Reaching the maximum number of cells with the minimum payload needed for efficacy is also a subject of attention in fractionated dosing. With single-agent ADC dosing, fractionating the dose only results in slightly lower efficacy, likely because single dosing was probably overkilling perivascular cells. However, fractionated doses with coadministration of the carrier dose significantly decreased efficacy compared to a single bolus dose with a carrier at the same ratio (e.g., 8:1, Fig. 2.7). The lower T-DM1 concentration per dose and dilution of the payload from the carrier dose pushes too many cells below a lethal number of payloads per cell. However, fractionated dosing can increase tolerability, which leads to the possibility of increasing ADC dosing and tumor drug exposure. The coadministration of ADC with carrier and fractionated dosing can provide not only better tumor penetration but also greater AUC and total payload tumor uptake. Therefore, our results show that fractionated dosing can be beneficial if it improves tolerability enough to increase the dose and overcome the decreased tissue penetration caused by a lower C_{max}, consistent with previous publications on fractionating dosing (appendix Fig A.8).[110] This is the approach taken with the clinical dosing for enfortumab vedotin, currently in phase III clinical trials with a 1.25 mg/kg weekly dose.[128]

The current model has several limitations. Although this model is helpful in capturing the tumor growth efficacy of ADCs, it currently does not capture the development of resistance that

could occur when cancer cells are exposed to diluted drug concentrations.[129] All the cells in this model are sensitive to the drug, and the results here have indicated that the best regimens are found with increased drug distribution even at lower payloads per cell. The trade-off in increased efficacy versus increased risk of resistance is complicated by other factors such as tissue-level secondary drug effects (e.g., collapse of vessels in heavily treated areas) and additional mechanisms of action (e.g., immune cell interactions) described below. For this reason, regimens that select resistant cells and stimulate cell mutation should be studied in the future with this model.

We calibrated our model to *in vivo* toxicity, and our probabilities could have overestimated cell killing due to secondary effects from the drug treatment. Cancer cells *in vivo* can die through direct and indirect mechanisms. For example, as cancer cells around a blood vessel die, blood vessels can also collapse, limiting the oxygen and nutrient delivery to other cells nearby. This may alter cell death or proliferation rates locally and could be considered in future work. Further work might also consider other sources of heterogeneity, such as heterogeneous antigen receptor expression, and the simultaneous actions of the immune system toward killing tumor cells. Despite these caveats, our model results reasonably match the toxicity from *in vitro* experimental data (after accounting for a faster doubling time and lack of transport limitations, which are important considerations for *in vitro/in vivo* correlations).[80] In addition, our model results agree with IC_{50} values found in previously publications.[9]

Finally, our current model does not take into consideration the immune system in combating cancer, including multiple mechanisms of action through the antibody Fc domain.[130] In fact, ADCs have been shown to be more effective in immunocompetent animal models.[29] Fortunately, our computational model has the potential to study and incorporate the probabilistic behavior of the immune system in response to these therapies, as already established in our lab for

the study of an infectious disease.[125, 131] Once appropriately calibrated to a particular ADC, the model also has the potential to be used to set preclinical benchmarks for targets with expression levels quantified by immunohistochemistry or even personalizing treatment with individualized dosing.[132] Therefore, this ABM has the capability of addressing the complexities in ADC therapy including the impact of carrier doses and dosing regiments on the heterogeneous tissue delivery and single-cell responses demonstrated here.

2.7 Conclusion

We developed a hybrid ABM to capture heterogenous drug delivery of ADCs and individual cellular responses and to predict tumor growth curves and overall efficacy. The ABM enables detailed depictions of heterogeneous vascularization and ADC delivery, cancer cell death, tumor growth, and treatment efficacy following different drug regimens. The model results demonstrate that a carrier dose of unconjugated antibody can improve efficacy if the number of cells reached by the ADC outweighs the reduction in targeted cell killing, which depends on expression, payload potency, and dosing. This will result in the largest number of cells receiving a lethal dose. Likewise, fractionated dosing can improve efficacy if increased tolerability allows higher ADC dosing to overcome the loss in tissue penetration from a lower C_{max}. By incorporating multiple competing effects within the tumor microenvironment, the simulations can aid in the development of new drugs and targeted therapies.

Chapter 3 A Prediction of the Selection of Resistant Cells by T-DM1 and T-MMAE in Coadministration Regimens with Trastuzumab

The goal of this chapter is to predict distribution and efficacy of coadministration regimens of ADCs with bystander (T-MMAE) or non-bystander payloads (T-DM1) with their unconjugated antibody trastuzumab in heterogeneous tumors. This was achieved by updating the model presented in Chapter 2 to capture intratumor heterogeneity with respect to receptor expression and intrinsic resistant that was used to also predict the selectivity of resistant cells by these regimens.

3.1 Abstract

Intratumoral heterogeneity is one of the main causes of treatment failures leading to tumor recurrence with worse prognosis. For the antibody-drug conjugate ado-trastuzumab emtansine (T-DM1), two major types of resistance include changes in HER2 expression and reduced sensitivity to the payload, often exacerbated by heterogenous HER2 expression and ADC distribution in the treatment. ADCs with bystander payloads such as trastuzumab-MMAE (T-MMAE) have the ability to reach and kill adjacent cells with lower receptor expression that cannot be targeted directly with the ADC. Additionally, coadministration of T-DM1 with its unconjugated antibody (trastuzumab) can improve distribution and minimize heterogeneous delivery. However, the effectiveness of trastuzumab coadministration and ADC bystander killing in heterogenous tumors and the selection of resistant cells are not clear. Here, we use an agent-based modeling platform to predict outcomes with these different regimen combinations. The simulations demonstrate that both T-DM1 and T-MMAE benefit from trastuzumab coadministration for tumors with high

average receptor expression, with greater benefit for non-bystander payloads. However, the benefit decreases as receptor expression is reduced, reversing at very low concentrations for this resistance mechanism that impacts both the ADC distribution and efficacy. For tumors with intrinsic payload resistance, coadministration with both ADCs uniformly exhibited better efficacy than ADC monotherapy. Finally, we demonstrated that several regimens select for resistant cells, highlighting the need to pursue other mechanisms of action for durable treatment responses.

3.2 Background

One of the main causes of treatment failures for therapies that target HER2 receptors is intratumoral heterogeneity, which leads to cancer relapse with a worse prognosis.[133] The combination of incomplete cell killing and tumor heterogeneity is a widespread problem in chemotherapy that can result in selection of resistant cell populations. Residual tumor cells left from previous treatment are the major cause of tumor recurrence as treatments are rarely able to eradicate all cancer cells.[134, 135] Finding approaches to eliminate all tumor cells is a very challenging task in the development of effective treatments that avoid tumor relapse.

Antibody-drug conjugates such as ado-trastuzumab emtansine (T-DM1), commercially known as Kadcyla®, are a type of targeted therapy approved by the Food and Drug Administration (FDA) for HER2 overexpressing breast cancer relapsed from treatment with trastuzumab (Herceptin®).[136] T-DM1 efficacy has been linked closely to HER2 expression, and its efficacy decreases with the decrease in HER2 expression.[33] Recently, Bon *et al* have shown that patients that are previously treated with pertuzumab (also a HER2 monoclonal antibody targeting agent) have reduced HER2 receptor availability making T-DM1 not as effective as a second-line treatment for patients previously treated with trastuzumab/pertuzumab as a first line regimen.[137]

Unfortunately, T-DM1 resistance is not limited to HER2 expression, but other forms of resistance such as binding site barrier, defective internalization, drug efflux pumps, and lysosomal proteolytic activities make both acquired and intrinsic resistance a major problem.[33, 138-140] In this chapter, I will focus on two types of resistance mechanisms: reduced HER2 expression as a mechanism that impacts both tissue distribution and cellular potency, and payload sensitivity, which impacts cell potency alone.

New ADC mechanisms and administration regimens have been shown to potentially overcome some of the barriers and resistance mechanisms to treatment. Some ADCs, for example, may contain linkers and payloads like MMAE that are more lipophilic than the DM1-lysine conjugate released by T-DM1, and have the ability to enter adjacent cells by crossing the cell membranes once they are released inside ADC-targeted cells. This mechanism is known as the bystander effect, and if the payload reaches sufficient concentration, adjacent cells that cannot be directly targeted by the ADC may be killed. This has been one approach proposed to kill cells that are resistant due to lower receptor expression.

An approach to improve heterogenous drug distribution, also known as the binding site barrier, during T-DM1 administration is coadministration with its deconjugated antibody trastuzumab. ADC monotherapy with T-DM1 at a clinical dose (3.6 mg/kg) shows that the drug is localized around blood vessels in solid tumors, and most of the tumor does not receive the treatment.[16] As shown by Cilliers *et al*, coadministration of trastuzumab and T-DM1 can improve penetration and efficacy of these in solid tumors.[31] At the same time, this co-administration reduces the number of payload for the targeted cells, thereby making these cells theoretically more susceptible to continued growth and division. However, it is not clear how antibody

coadministration can influence the selection of more resistant cells alongside bystander effects, which can potentially alter the risk of tumor relapse.

Quantifying the distribution, uptake, and efficacy of ADCs with and without coadministered antibody in heterogeneous tumors treated with bystander payloads in comparison to non-bystander payloads is important but time-consuming work that requires extensive animal experiments. These studies are also compounded by potential growth differences among sensitive versus resistant cell phenotypes and the large tumor growth variability present in animal models, requiring large cohort sizes. Here, we use a validated agent-based model described previously (Chapter 2 and [141]) to quantify how ADCs with bystander payloads modulate efficacy in heterogeneous solid tumors, both with and without coadministered antibody, specifically focusing on overall efficacy and selection of resistant cells. In particular, we focus on three main questions: 1) How do carrier doses and bystander effects (MMAE vs. DM1) impact the distribution, uptake, and efficacy of ADC treatment in tumors with heterogeneous HER2 expression? 2) Do carrier doses and bystander effects show the same result when cell sensitivity to the payload does not impact tumor distribution? And 3) How do different coadministration regimens affect the selection of resistant cells, which could lead to resistant tumor relapse?

3.3 Methods

We extended our hybrid agent-based model framework, introduced in [141] and Chapter 2, to incorporate additional physical and biological phenomena. Briefly, the model is comprised of cells and blood vessels that behave based on probabilistic rules and their microenvironment. The previous model described: plasma dynamics (clearance), drug dynamics (ADC mechanism for non-bystander payloads), and cell dynamics (e.g., cell division, death) that impact the tumor volume in our simulations. Here, the model is extended to include: 1) angiogenesis, allowing us to

look at treatment over longer periods of time, 2) heterogeneous receptor expression and/or internal sensitivity of cancer cells to payloads, and 3) bystander payloads. These additional features allow us to compare coadministration of T-DM1 and T-MMAE with trastuzumab in different tumor environments (Figure 3.1).

Simulation Environment and Framework

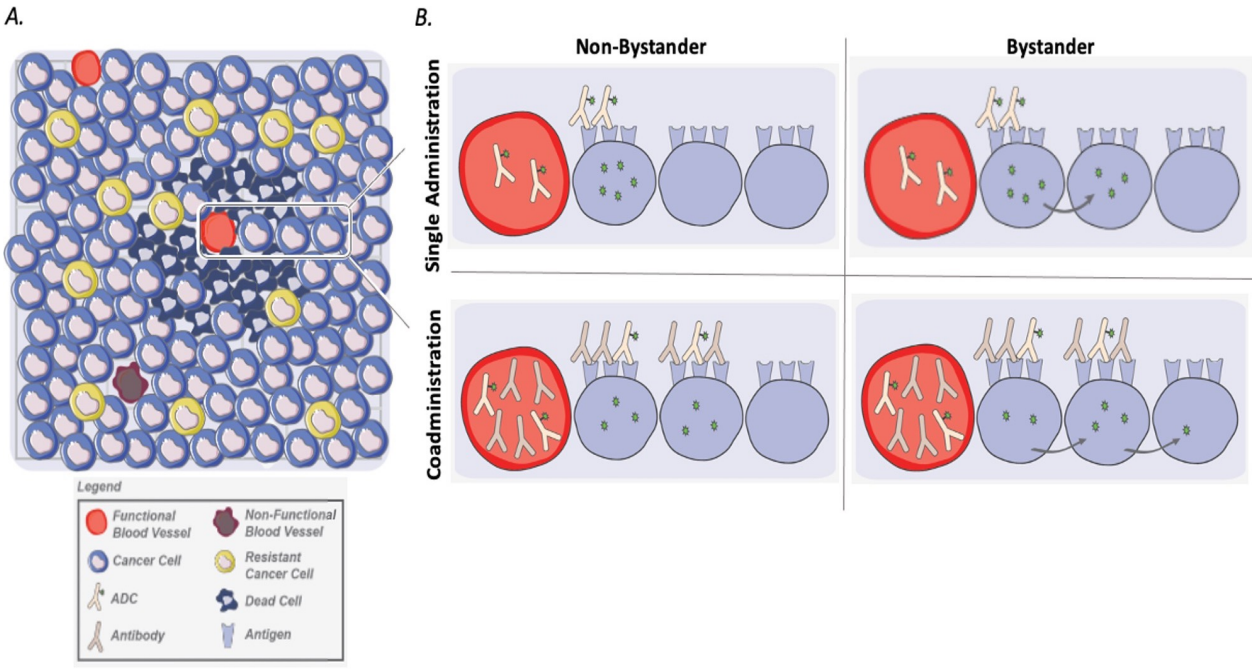

Figure 3.1 Model Schematic
(A) ABM environment is composed of cancer cells with different characteristics (e.g. different number of receptors or sensitivity to treatment). B) The model will test different regimens: 1) single agent administration (top panel) vs coadministration (bottom panel) and 2) bystander (right column) vs non-bystander payloads (left column). The model can be used to examine these regimens for cell populations containing resistant cells.

The model is a 2D representation of a tumor section that contains cells and blood vessels on a lattice of several thousand cells. The cells and blood vessels have different states, i.e., alive or dead for cells and functional and non-functional for vessels, and they occupy specific positions on the simulation grid. Each cell occupies a volume of 2 x 10^{-12} L (12.6 μm on a side), and the initial tumor, which has about 1940 cells, is assumed to represent an initial tumor volume range of

200-300 mm^3. ADCs enter the tumor through active blood vessels, and the functional vessel density changes based on the tumor size. Cells change their state from alive to dead based on the concentration of payload bound to microtubules inside of the cells. The plasma dynamics, drug dynamics, and agent dynamics (cancer cell and blood vessel dynamics) are synced as described previously.[104] Cells were assigned either 1 million receptors/cell or 50K receptors/cell, and the fraction of cells in each category could be varied. Placement of cells with either receptor number was random on the grid.

ADC Dynamics with Bystander Effects

For distribution studies, drugs are administered as a single administration on day 0, and their dynamics inside the host is described with ordinary and partial differential equations. Drug dynamics with bystander effects were previously published using a Krogh cylinder model in our lab.[30] The same equations, also shown in Appendix B.1-B14, were added to ABM model. Briefly, as shown in Appendix Figure B.1.A and B.1.B, T-DM1, T-MMAE, and trastuzumab are cleared from the plasma biexponentially, while they can at the same time extravasate into the tumor, diffuse through the interstitial tissue, bind to HER2 receptors, and be internalized. After ADCs are degraded in lysosomes, the payloads Lys-SMMC-DM1 (referred to as "DM1" henceforth) and MMAE, from T-DM1 and T-MMAE respectively, enter the cytoplasm and either bind to microtubules or leave the cell. Both payloads in the interstitial tumor tissue also have the ability to enter cancer cells directly, but at different rates determined by their individual properties. All parameters and rate constants for model dynamics are shown in Table 3.1.

Table 3.1 Model Parameters

Parameter	Value	Unit	Description	Reference
k_{10}	4.55×10^{-6}	s^{-1}	Total antibody clearance	114
k_{12}	8.06×10^{-6}	s^{-1}	Antibody clearance for compartment 1 to 2	114
k_{21}	1.33×10^{-5}	s^{-1}	Antibody clearance for compartment 2 to 1	114
V_1	1.2×10^{-3}	L	Volume central compartment	141
k_{on}	7.1×10^{5}	$M^{-1}s^{-1}$	ADC binding rate constant	13
K_d	0.5	nM	ADC dissociation constant	13
k_{off}	3.5×10^{-4}	s^{-1}	ADC dissociation rate constant	13
k_e	3.3×10^{-5}	s^{-1}	ADC internalization rate constant	7
k_{deg}	8×10^{-6}	s^{-1}	ADC lysosomal degradation rate constant	111
$k_{in,DM1}$	5.95×10^{-5}	s^{-1}	DM1 rate constant from the lysosome to cytosol	30
$k_{in,p\ DM1}$	5.95×10^{-5}	s^{-1}	DM1 cell internalization rate constant	30
$k_{out\ DM1}$	3.94×10^{-5}	s^{-1}	DM1 rate constant from the lysosome to cytosol	30
$k_{in,MMAE}$	1.41×10^{-3}	s^{-1}	MMAE rate constant from lysosome to cytosol	30
$k_{in,p\ MMAE}$	1.41×10^{-3}	s^{-1}	MMAE cell internalization rate constant	30
$k_{out\ MMAE}$	6.87×10^{-4}	s^{-1}	MMAE rate constant from lysosome to cytosol	30
$k_{on,p}$	8.33×10^{-6}	nMs^{-1}	DM1 and MMAE binding rate constant to intracellular target	86
$k_{off,p}$	0.003	s^{-1}	DM1 and MMAE unbinding rate constant	86
DAR_{DM1}	3.5	-	DM1 to antibody ratio	118
DAR_{MMAE}	4	-	MMAE to antibody ratio	114
R_s	2.75×10^{-11}	M/s	Target synthesis	117
T_{total}	5×10^4 - 1×10^6	receptors/cell	Total targets per cell	Varied
ε	0.24	-	Intracellular void fraction of ADC and Ab	119
ε_{pay}	0.44	-	Intracellular void fraction of payload	15, 30
D_{ADC}	1×10^{-11}	m^2/s	Effective Diffusivity of ADC and Ab	6
D_{DM1}	9.8×10^{-12}	m^2/s	Effective Diffusivity of DM1	30
D_{MMAE}	1.4×10^{-11}	m^2/s	Diffusivity of MMAE	30
P_{ADC}	3×10^{-9}	m /s	Vascular permeability of ADC and Ab	120
P_{pay}	1×10^{-4}	m/s	Vascular permeability of the payload	6
$P_{max,\ DM1}$	0.0014	-	Maximum probability for cell killing for MMAE	Calibrated
$K_{m,\ DM1}$	800	nM	Michaelis-Menten constant for DM1	Calibrated
$P_{max,\ MMAE}$	0.006	-	Maximum probability for cell killing for MMAE	Calibrated
$K_{m,\ MMAE}$	600	nM	Michaelis-Menten constant for MMAE	Calibrated
t_d (*in vivo*)	5-17	days	*In vivo* doubling time	Calibrated
t_d (*in vitro*)	1-2.5	days	*In vitro* doubling time	Estimated

*1 million receptors per cell corresponds to 833nM receptors where each cell occupies about 2×10^{-12} L.

Vessel Dynamics

While tumors form new blood vessels to sustain tumor growth (angiogenesis), the functional or active vessel density is also known to decrease in tumors. In this model, locations on the grid blood vessels (functional and non-functional) were placed before the start of the simulations. The initial densities of total blood vessels and active blood vessels were calibrated as

shown in [141]. At each agent time step, new blood vessels become functional as tumor size increases, but the overall vessel density decreases. This is done by calculating the fraction of active blood vessels at each agent time step and comparing it with the tumor volume at that exact time and with its initial fraction of active blood vessels set at the beginning of the simulation as shown in Equation 18.

$$f_a = fr_o(aV^{-b}) \tag{18}$$

where f_a is the active fraction of blood vessels at the agent time step, fr_o is the active fraction of blood vessels assigned at the beginning of the simulation, V is tumor volume at the agent time step (mm^3), and a and b were fit to experimental data and has values of 4.64 and 0.28 respectively, (Appendix Fig B.2).[142] With this method, the overall decrease in active vessel density that occurs at the same time that a new blood vessels are formed with the increase in tumor volume is captured. As shown in Appendix Fig B.3, the addition of angiogenesis better fits the experimental data with fractionated doses as compared to our previous version of the model with static vessel distribution.

Cell Dynamics and Model Calibration

Cells proliferate and die during the simulation progression. All cells in the tumor in each simulation proliferate with the same doubling time, and each simulation has a different doubling time calibrated to experimental data with values from 5 to 17 days. Cancer cells change their states from alive to dead based on the concentration of payloads bound to the microtubules inside of the cell. The probability of cell killing per agent time step are represented by the Michaelis-Menten Equation (Appendix B.15). The maximum probability for cell killing and the Michaelis-Menten constant for DM1 (T-DM1) and MMAE (T-MMAE) were calibrated and validated to experimental

data from Cilliers *et al*[31] and Singh, *et al*[143, 144] using *CaliPro*, a calibration protocol for parameter estimation.[145] Results are shown in Appendix Fig. B.4 and B.5.

In vivo efficacy in xenograft model

All animal studies were conducted according to University of Michigan Institutional Animal Care and Use Committee. NCI-N87 cells were purchased from ATCC and grown at 37°C with 5% CO in RPMI1640 growth medium supplemented with 10% (v/v) FBS, 50 U/mL penicillin, and 50 µg/mL streptomycin. Mycoplasma testing was performed yearly using the Mycoalert Testing Kit (Thermo Fisher Scientific, NC971983). Cells were cultured 2 to 3 times per week up to passage number 40 (approximately 2.5 months). For the xenograft studies, 5 x 10^6 NCI-N87 cells were inoculated in the rear flank of 4-8 weeks old female nude (Foxn1mu/mu) mice from Jackson Laboratories. Tumors were measured with calipers every other day, and the tumor volume was calculated as length x width^2 / 2. When tumors reached approximately 250 mm^3, 3 doses of T-DM1 at 2.4mg/kg were given at days 0, 7, and 14. Tumors were monitored until the tumor reached 2000 mm^3, or until the tumor ulcerated.

3.4 Results

Bystander Payload Reaches More Cells Although at Lower Concentration

First, the payload concentration of MMAE and DM1 was quantified by simulating the distribution and uptake of ADCs and their respective payloads for 3.6 mg/kg of T-DM1 with DAR 3.5 (clinical dose) and 1.8 mg/kg of T-MMAE with DAR 4. The results shown in Figure 3.2 reflect the maximum peak that occurs at 24 hours for the ADCs bound on the surface of the cells and at day 4 for microtubule-bound payload. As seen in Figure 3.2A and 3.2.B, T-DM1 at 3.6 mg/kg

reaches more cells than T-MMAE at 1.8 mg/kg, consistent with increased penetration of a higher antibody dose. Appendix B.6 also shows the comparison between these two ADCs for the same dose and DAR where both ADCs reach the same number of cell receptors. However, for both of these doses, the payload MMAE reaches more cells than DM1 (Fig 3.2.C, Fig 3.2.D, Appendix Fig B.6.C and Fig B.6.D), consistent with previous results from the Krogh cylinder model and as expected given the bystander effects for MMAE.[30]

The single cell analysis capabilities of the ABM were used to quantify the penetration of MMAE in comparison to DM1, measured by percentage of cells with concentrations greater than150nM (>150nM), in between 150nM and 1nM (150nM > x > 1nM), and smaller than 1nM (< 1nM) for all the four scenarios (3.6mg/kg T-DM1 with DAR 3.5, 3mg/kg T-DM1 with DAR 3, 1.8mg/kg T-MMAE with DAR4, and 3mg/kg T-MMAE with DAR 3), as shown in Fig 3.2.E and Appendix Fig B.6.E. For T-MMAE administration, all cells are reached by MMAE, and the majority of the cells receive concentrations between 150nM and 1nM. In contrast, DM1 reaches fewer cells, and the majority of targeted cells receive concentrations higher than 150nM. Many cells in T-DM1 administration receive very little DM1, demonstrating a more heterogeneous distribution. These data capture the bystander effect of payloads such as MMAE that reach more cells with lower concentrations than the non-bystander payload, which is a consequence of the payload's lipophilicity and ability to diffuse into adjacent cells.

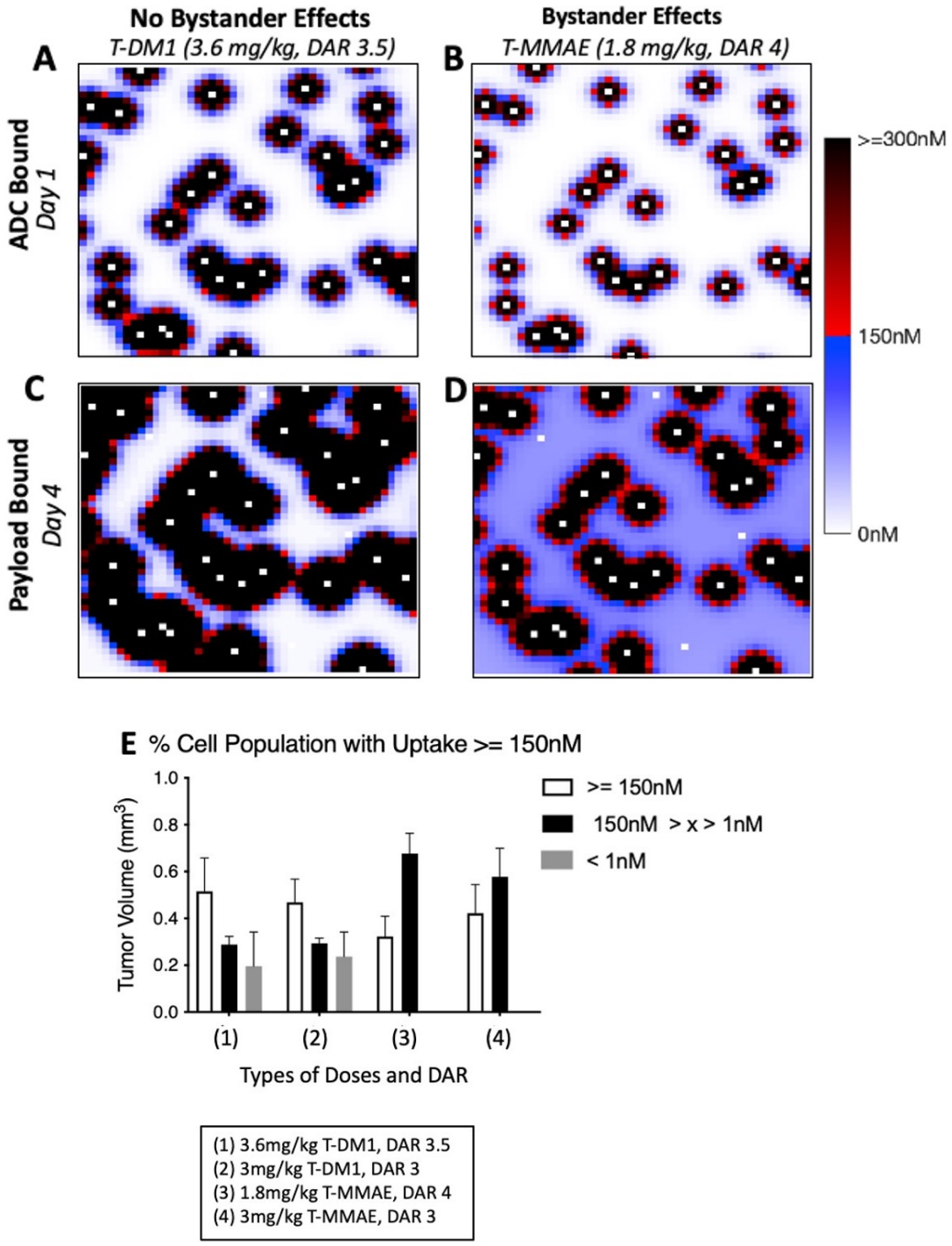

Figure 3.2 ADC and payload distribution
(A-B) Distribution of T-DM1 (3.6mg/kg with DAR 3.5) and T-MMAE (1.8 mg/kg, DAR 4) bound on the surface of the cancer cells. (B-C) Distribution of DM1 and MMAE bound to microtubules inside the cells. (E) Percentage of cells with >= 150nM, between 150nM and 1nM, and below 1nM at day 4 which refers to the day with maximum payload uptake for n=10. TMMAE has no cells with payload concentration lower than 1nM.

Antibody Coadministration Can Reduce Efficacy for Tumors with Low Receptor Expression

To compare how coadministration of trastuzumab with T-DM1 or T-MMAE impacts the efficacy in tumors with cell populations with different receptor expression of 1 million, we simulated tumors with varying fractions of cells with 1 million or 50,000 receptors per cell (ranging from 100% to 0% with 1M) and treated with trastuzumab to ADC dose ratios of 0:1, 3:1, and 8:1. The average tumor volumes at 50 days for administration of T-DM1 at 3.6 mg/kg (DAR 3.5) and T-MMAE at 1.8 mg/kg (DAR 4) are shown on Figure 3.3. In tumors with 60% - 100% of cells expressing 1M receptors, adding a carrier dose improves the efficacy for T-DM1 and for T-MMAE. In tumors with a majority of cells having lower receptor numbers (20% to 0% with 1M receptors), coadministration reduces efficacy, and administration of ADC only is more efficacious. The reason for the poor efficacy of coadministration is as follows. When most cells express only a low number of receptors, ADCs distribute more evenly in the tumor than for high receptor expression, increasing efficacy. Adding unconjugated antibody to the regimen (coadministration) puts the unconjugated antibody in competition with ADCs, and cells with fewer receptors do not internalize sufficient ADC for cell killing, lowering efficacy. As a control, Appendix B.7. shows the same regimens using cells with 1M receptors per cell versus cells with zero receptors/cell, demonstrating that there is no efficacy for tumors lacking receptor expression.[146]

The trade-off between improved tissue distribution (pharmacokinetics) and targeted cell killing (pharmacodynamics) is highlighted in the shift of cell populations with high, moderate, and low levels of payload uptake. Appendix B.8 shows the percentage of cells with payload concentration greater than 150nM, between 150nM and 1nM, and below 1nM for co-administration of T-DM1 and T-MMAE with trastuzumab for tumors with 100%, 70%, 30%, and 0% of cells expressing 1M receptors/cell. For example, in the Appendix Figure B.8.A, fewer high

expression cells allow the ADC to reach more cells at concentrations >150 nM. In contrast, in Figure B.8.C, high coadministration (8:1) leads to fewer cells with >150 nM payload concentration.

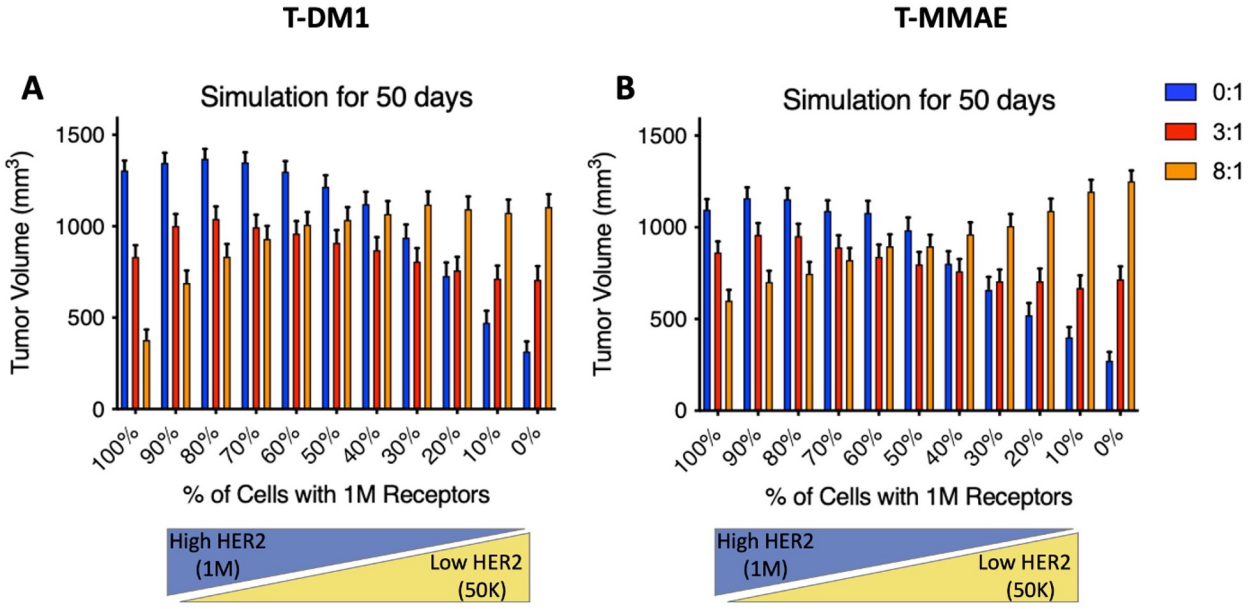

Figure 3.3 Treatment efficacy at 50 days for tumors with heterogeneous receptor expression. (A) T-DM1 regimens (3.6 mg/kg and DAR 3.5). (B) T-MMAE regimens (1.8 mg/kg and DAR 4) for tumors with changing percentage of 1M or 50K receptors per cell. Data is shown n=100 and SEM. SD is shown in Appendix B.7.

Bystander Effects Mitigate Loss in Efficacy from Coadministration at Low Receptor Expression

To better understand the role of MMAE bystander effects on T-MMAE efficacy, we simulated the distribution and efficacy of T-MMAE while artificially removing the payload's ability to enter adjacent cells. For simulations varying receptor expression, similar to Fig 3.3, we set the internalization rate constant of MMAE to enter adjacent cells to zero (k_{inp}=0) as shown on Figure 3.4. Comparing the distribution of Figure 3.4.E with control (Figure 3.4.B), the elimination of payload entering adjacent cells reduces the MMAE uptake in bystander cells, as expected. The tumor growth curves show modestly improved responses in general, with significant improvement for high co-administered doses with low receptor expression, where bystander effects help retain

payload concentrations at an effective concentration. Similarly, efficacy requires that sufficient payload must remain inside the original cell to cause killing (Appendix Figure B.10).

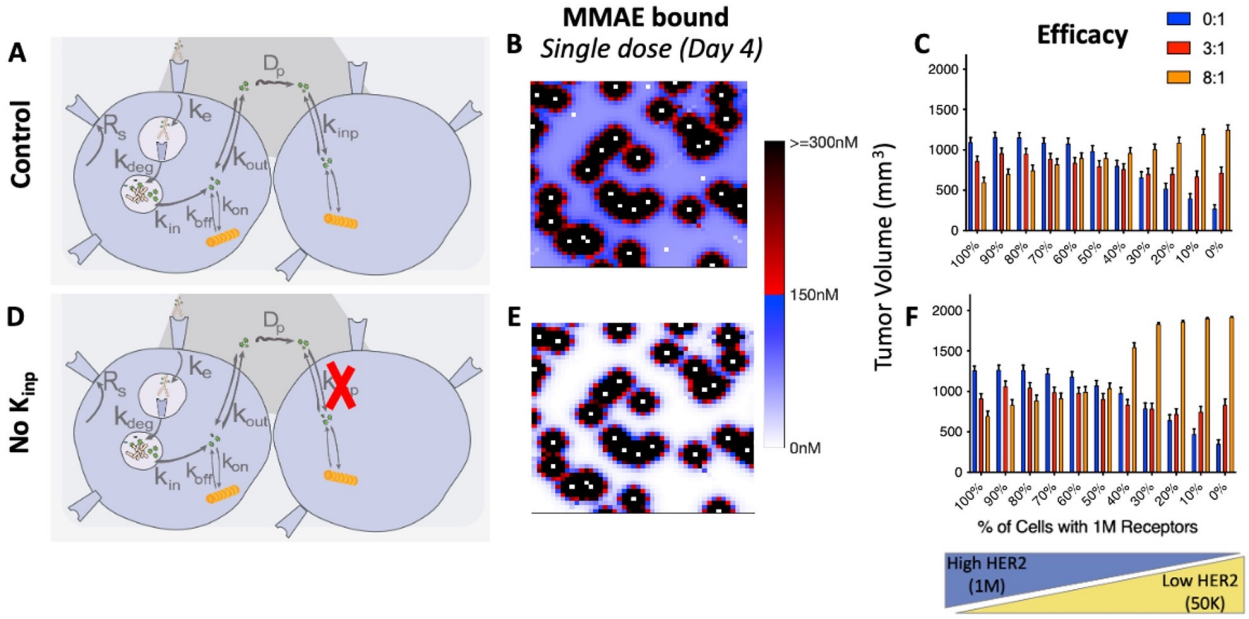

Figure 3.4 Spatial distribution of payload with bystander or non-bystander effects.
A-C) Control distribution and efficacy for regimens for T-MMAE. D-F) Distribution and Efficacy for regimens of T-MMAE eliminating k_{inp} rate constant. Simulations show mean and SEM with n=100. The same data is shown in Appendix Fig B.11 with SD.

Coadministration Improves Efficacy with Intrinsic Resistance

Not all mechanisms of drug sensitivity impact distribution. We simulated tumors with cell populations with higher Km parameter from the probability of cell killing (Appendix Eq. B15) to mimic cells that are naturally more resistant to treatment and predict how coadministration affects those tumors. For these cells, Km was doubled (Km=2x) and quadrupled (Km=4x), and simulations with varying percentages of more sensitive cell populations, with and without coadministration, are shown in Fig 3.5. For T-DM1, all the regimens with coadministration improve efficacy compared with ADC alone, and for these regimens, increasing the percentage of resistant cells worsen efficacy of all the regimens as expected (Fig 3.5.A and B). For T-MMAE,

coadministration for tumors with high fraction of sensitive cells also clearly show the benefit of the carrier dose. However, as the percentage of cells with intrinsic resistance increases, the benefit of the carrier dose is less evident. This is due to the high 'dilution' of T-MMAE with trastuzumab, which affects the ability to kill those more resistant cells that require a higher concentration of the payload despite better tissue penetration reaching more cells.

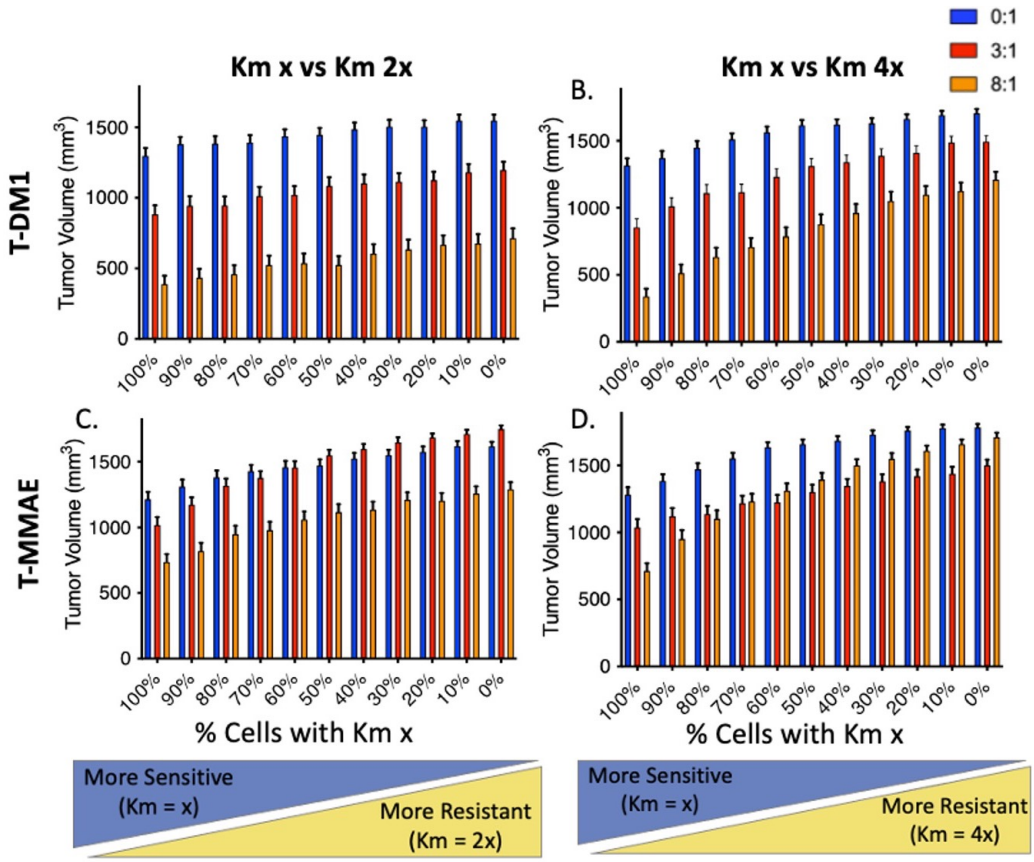

Figure 3.5 Regimens with intrinsic resistance and comparison with sensitive cells.
(A-B) Regimens with T-DM1 and TMMAE (C-D) with higher K_m=2x and K_m=4x to representing intrinsic resistance.

The percentages of cells with high, medium, or low payload concentration does not change as the percentage of resistant cells increase. The payload uptake between 100% to 0% is similar as expected (data not shown), and variations are only due to the stochasticity of the ABM. This confirms the lack of impact on tumoral distribution despite changes in drug sensitivity. Without

the ‘benefit’ of reduced receptor expression increasing tissue penetration, coadministration to achieve increased penetration generally results in better efficacy.

Regimens with Greater Efficacy Can Select for More Resistant Cells

We performed simulations to determine whether bystander or non-bystander payloads and/or different coadministrations could select for a small number of less sensitive cells to repopulate the tumor. Simulations were performed in which the initial tumor size was composed of 1% of cells with lower receptor expression (Fig 3.6.A-F), or with intrinsic resistance (value of Km 2x) (Fig 3.6.G-L). The average number of cells for 100 simulations are shown for coadministration of T-DM1 and T-MMAE with trastuzumab. In general, as the ratio of trastuzumab to ADC increases, efficacy is increased in T-DM1 administration and in T-MMAE administration in heterogenous receptor expressing tumors. However, resistant cells become a larger percentage of the tumor in several scenarios, showing the selection of resistant cells. Notably, the selection is highest for a non-bystander payload (T-DM1) at the highest coadministration dose (8:1). As observed in the Appendix Figure B.11, the percentage of the more resistant cell increases significantly. T-MMAE also had improved efficacy with higher coadministration for tumors with difference in receptor expression, but it showed no change in efficacy with coadministration for more intrinsically resistant tumors (Fig 3.6.J-L).

MMAE presents bystander payload that allows the drug to diffuse more homogeneous through the tumor, but it also decreases the single-cell uptake. For intrinsic resistance that requires a higher concentration of the payload, T-MMAE here at 1.8mg/kg dose was not effective. Since bystander effects result in lower concentrations in cells than directly targeted cells, many of the intrinsically resistant cells distant from vessels do not receive a lethal dose.

Another important observation in these data was that with only 10 simulations, as shown in Appendix Figure B.13, the trends seen here in Figure 3.6 are lost in the tumor variability. This suggests that many samples must be taken to identify the most effective treatment, which may not be feasible with animal experiments alone.

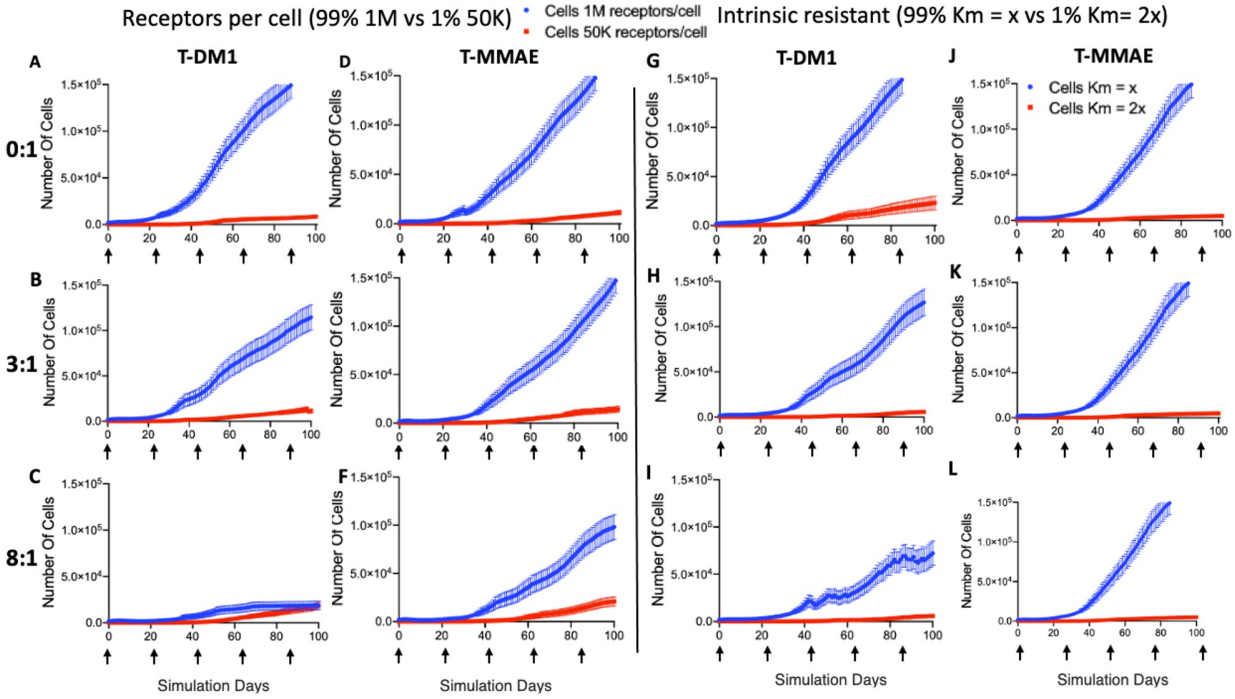

Figure 3.6 Tumor cell growth with initial composition of 1% more resistant cells vs sensitive cells for different regimens with T-DM1 or T-MMAE.
(A-F) Coadministration of trastuzumab 0:1, 3:1, 8:1 with T-DM1 (A-C) and T-MMAE (D-F) regimens with 1% of cells with 50K receptors per cell vs 99% of 1M receptors per cell. (G-L) Coadministration of trastuzumab 0:1, 3:1, 8:1 with (T-DM1 (A-C) and T-MMAE (D-F) regimens with 1% of cells with higher intrinsic resistance (Km=2x) vs 99% of cell with Km=x. Km=800nM for T-DM1 and Km=600nM for T-MMAE. All simulations were n=100, and SE is plot.

3.5 Discussion

The development of ADCs has improved in the past few years, including the increased reliance on bystander payloads and higher antibody doses. The main goal of next generation ADCs is to improve the therapeutic index of these drugs by increasing efficacy while maintaining relative

safety.[106] This could be achieved by: 1) increasing the delivery to more cells within the tumor, 2) balancing bystander payload physicochemical properties to reach adjacent cells with sufficient concentrations to induce cell killing while avoiding extensive tumor washout, and 3) driving immune responses to leverage alternative mechanisms of cell killing aside from the payload. In this work, we focused on the first two approaches. Overcoming ADC delivery challenges such as the binding site barrier and heterogeneous receptor expression requires strategies including the use of bystander payloads and coadministration regimens in order to reach cells that may not be directly targeted by ADCs like T-DM1. [33, 37] [36] Here, we used our updated hybrid agent-based model to predict the various modalities of administration of ADCs with bystander or non-bystander payloads in heterogeneous tumors (specifically heterogeneous receptor expression and intrinsic resistance). This model presents an advantage to previous models because it includes single-cell heterogeneity, drug responses, high-resolution tuning of cancer cell and blood vessel dynamics, and heterogeneous ADC and payload delivery that are not achievable with commonly used compartmental or Krogh cylinder models.

Bystander payloads vary in lipophilicity and potency, affecting both the ADC's PK and PD. For example, MMAE has a larger lipophilicity compared to Lys-SMCC-DM1, clogD 2.01 and 1.21 respectively.[30] This changes how easily payloads cross cell membranes, how well they stick to proteins inside and outside the tumor cells, and the effective diffusion through the tumor tissue. As seen in Figures 3.4.C and 3.4.D (and Appendix B.6.C and B.6.D), this helps MMAE to penetrate deeper and more homogeneously into the tissue, while DM1 has a more heterogeneous distribution influenced entirely by the penetration depth of the intact ADC. MMAE, on the other hand, does not accumulate to sufficient levels inside cells reached via the bystander effect at the

doses given here (1.8mg/kg), but for higher doses like 3.6mg/kg, the payload reaches cells with higher concentrations shown to be very effective.[86, 144]

Due to MMAE's relatively high potency, the bystander scape of the payload and loss in the concentration are only evident in high trastuzumab ratios and in tumors with lower total receptor expression (e.g. 30%-0% 1M, Fig 3.4F). Other very toxic bystander payloads such as PBD and DGN (DNA alkylators) are also very lipophilic and have demonstrated more optimal bystander efficiency by balancing the difference between retention and diffusion through cells.[30, 147] However, these potent payloads must be administered at lower doses than microtubule inhibitors due to their toxicity.

In general, T-MMAE and T-DM1 efficacy benefits from coadministration with trastuzumab for tumors with high receptor expression, but the benefit of coadministration is reduced and eventually lost for tumors with lower receptor expression as shown in Figure 3.3. Consistent with previous work by Khera et al, coadministration offers advantages for T-MMAE in high expression tumors, since the efficiency of direct cell targeting is greater than bystander killing.[30] Because of the higher potency of MMAE compared with DM1, by artificially trapping the payload inside of the cell, MMAE benefits from higher accumulation of payload per cell (Appendix B.10). Figures 3.3 and 3.4 highlight the need for a balance between fast escape of the payload versus accumulation in cells to mediate cell death. Approaches that enable fast endosomal/lysosomal escape but prevent cellular escape (similar to the dolaflexin payload) could increase potency by locking the toxic payload inside of the cell.[148] The higher efficacy of T-DM1 and T-MMAE with increasing numbers of low-expressing cells may seem counter-intuitive. However, this result, where lower receptor expression improves efficacy due to better tissue penetration, has been observed experimentally.[21, 146]

Other diverse mechanisms of resistance can lead to intrinsic resistance wherein cells require a higher concentration of drug for cell killing.[149] We performed simulations to understand how coadministration of antibody with ADCs carrying bystander and non-bystander payload in the presence of these resistant cells modulates efficacy. In general, the results on Figure 3.5 show that coadministration is better for the vast majority of tumor compositions when the resistance mechanism does not influence tumor distribution. A few tumor compositions with very high concentration of resistant cells (right side of Figures 3.5.C and D) show similar efficacy regardless of carrier dosing, but these regimens are ineffective overall. The benefit of the carrier dose is greater for T-DM1 than T-MMAE due to the ability of bystander payloads to partially compensate for heterogeneous tissue penetration. When the resistance mechanism doesn't influence distribution, the carrier dose is more consistently beneficial with fewer trade-offs.

In our study, we also saw that the regimens that lead to better efficacy, also lead to selection of more resistant cells (Fig 6.C) in comparison with other regimens. These dynamics highlight fundamental limitations in improving efficacy by only taking into consideration changes in dosing regimens of ADCs. Although these approaches are beneficial for a period of time, the reoccurrence of the tumor can lead to an even more resistant tumor composition which is often is seen in the clinic to lead to a worse prognose than from the beginning of the patient treatments. This work highlights the need to utilize other mechanisms of action and/or treatments, similar to combination therapy used with current chemotherapeutics. This could include efforts to mitigate specific mechanisms of resistance, such as selecting payloads that are less susceptible to drug exporters, or more broadly effective approaches including the stimulation of an immune response.

The ability of the hybrid ABM to add other cells such as immune cells, in additional to the benefits of simulating regimens that would be impractical otherwise, make this a powerful tool to

study the development of this drug class. Many ADCs have already been used because of their immunostimulatory effects, such as combination therapy with checkpoint inhibitors and immune cell agonists, and these characteristics could be studied computationally to assist animal experiments. In addition, computational approaches provide additional power to discern trends that may be lost in the noise during animal studies with small cohort sizes (Appendix Fig B.15) These mechanistic trends may not appear until later during development when larger studies and/or clinical trials are conducted. For example, when we tested the selection of resistant cells for n=10 (Appendix Fig. 12), we could not see the trends as clear as with n=100 as shown on Figure 6. This supports the use of computer simulations, especially with ABMs, as an approach to help hasten the development of ADCs.

3.6 Conclusions

Using an updated hybrid ABM[141] we tested the impact of carrier dosing and bystander payloads on treatment efficacy with heterogeneous cell populations and the selection of resistant clones. In addition to heterogeneous cell populations, the updated model included dynamic functional vessels to account for changes in vessel density due to angiogenesis and vascular collapse during repeated dosing. Finally, bystander payload effects were simulated where the payload can diffuse into adjacent cells or wash out of the tumor. Two scenarios were simulated: changes in receptor expression, which impact both drug distribution and cellular potency, and intrinsic resistance that only impacts cell potency. The model demonstrated the benefit of a carrier dose with high receptor expression for both T-MMAE and T-DM1, with the greater benefit for non-bystander payloads. As the average receptor expression decreased, the benefit diminished until no carrier dose was more effective at low receptor density. When the resistance mechanism

only impacted cell potency, co-administration was more uniformly beneficial. Finally, we showed that several regimens efficiently selected for resistant clones, highlighting the need to pursue additional mechanisms of action or treatments to improve the durability of treatment response. In summary, by adding additional dynamics in the tumor microenvironment, these simulations can help guide the overall development of ADC therapies.

Chapter 4 Evaluating the PK/PD of Coadministration of TAK-164 with 5F9 in Heterogenous Tumors

The goal of this chapter is to predict distribution and efficacy of coadministration regimens of the anti-GCC ADC TAK-164 with its unconjugated antibody 5F9 in primary human tumor xenograft (11C PHTX). The work in this chapter was in collaboration with Dr. Eshita Khera and Dr. Cornelius Cilliers who provided the experimental data. In Chapter 2, we demonstrated that tumors that receive heterogeneous distribution of ADCs can be improved through coadministration with their respective antibody. Here, we evaluated the mechanisms that modulate distribution and efficacy as they relate to TAK-164 and 5F9 coadministration in 11C PHTX tumors.

4.1 Abstract

The development of new antibody-drug conjugates (ADCs) has led to the approval of 5 new ADCs by the FDA in the past two years. The ADC's main components, the antibody, payload, and linker, have been designed to improve the overall delivery and efficacy of these therapeutics in solid tumors. Bystander payloads, for example, are of major interest in these new ADCs as these payloads have the potential to leave the targeted cell and diffuse into neighbor cells. This mechanism could improve the efficacy of ADC treatments in heterogeneous tumors (Chapter 3). TAK-164, an ADC composed of an anti-GCC antibody (5F9) conjugated to a DNG payload, has been demonstrated to have bystander effects. In this chapter, my colleagues and I evaluated the distribution and efficacy of the coadministration of TAK-164 and 5F9 in primary human tumor xenografts (PHTX11C) which are considered more complex than single cell xenograft models.

Here we combined experimental and modeling approaches to understand the outcome of the coadministration regimens of this ADC.

4.2 Background

Antibody-drug conjugates (ADC) have seen significant growth in the past few years with a total of 9 ADCs approved and many more in the pipeline. Although ADCs have been explored in pursuit of a 'magic bullet' for about 30 years, progress has been slow until recently, with 5 of the ADCs were approved just within the past two years.[3] However, the development of ADCs for solid tumors is still a challenge that depends on many complex physiochemical properties of its components and the complex tumor microenvironment. ADCs are composed of 1) an antibody that targets the receptors overexpressed in cancer cells, 2) a cytotoxic payload that leads to apoptosis, and 3) a linker that connects the payload to the antibody. Optimizing each of these ADC components individually and in concert is critical for the development more efficacious ADCs.[8]

Many ADCs have a heterogenous distribution in solid tumors at clinical doses. Once given intravenously, ADCs extravasate blood vessels, diffuse into the interstitium, bind to receptors on cancer cells, and are internalized. After the ADC is degraded in the cell lysosome, the payload is released to kill the cell. However, because ADCs are permeability-limited and extravasate into the tumor slowly, little of the injected dose reaches the tumor. In addition, binding rates are much faster than diffusion in the interstitium (often resulting in a binding site barrier), so most of the ADC administrated at clinical doses is localized on tumor cells close to the blood vessels. As seen in Chapters 2 and 3, coadministration of ADC and its unconjugated antibody have been proposed as an approach for better distribution and therefore better efficacy.[14, 31, 108, 141, 144]

The efficacy of the treatment is also dependent on the tumor microenvironment, which is not only composed of malignant cancer cells, but also many other cells and structures such as

immune cells, tumor vascular, stroma, and fibroblasts.[46] Primary human tumor xenografts (PHTX) or other patient derived tumor models are known to be useful for fast preclinical screening.[150] These tumors have greater complexity and clinical relevance in comparison with cell derived tumor xenografts. In this chapter we will evaluate the distribution and efficacy of TAK-164 in these more complex tumor environments.

TAK-164 is an ADC currently under clinical evaluation that targets guanylyl-cyclase C (GCC) receptors in colorectal and gastrointestinal cancers.[151, 152] It consists of a 5F9 antibody backbone and a DNA-alkylating DGN-549 payload. Previous evaluation of TAK-164 shows heterogeneous distribution in some PTHX models at an estimated clinical dose (based on other DNA-alkylating agents) of 0.4 mg/kg.[153] It has also shown strong bystander effects that could potentially compensate for ADC heterogenous distribution.[147]

Bystander payloads have been heavily explored in the next generation of ADCs, as these payloads have the ability to leave the cell targeted by the ADC and enter adjacent cells. As discussed in Chapter 3, the efficiency of bystander payload killing depends on its ability to diffuse through cell membranes (lipophilicity) and kill the cells (potency) prior to washing out of the tumor. For example, monomethyl auristatin E (MMAE) has a higher lipophilicity (clogD 2.04) compared to a larger and more charged non-bystander payload like Lys-SMCC-DM1 (clogD 1.21), which imparts to MMAE the ability to escape the cell via diffusion across cell membranes. However, as shown in Chapter 3, MMAE's absolute lipophilicity is not as high as lipophilic payloads (clogD ~3-6) such as pyrrolobenzodiazepine (PBD) and indolinobenzodiazepine (IGN), resulting in MMAE washing out from the interstitial tissue more easily. The highly lipophilic payloads are predicted to possess optimal properties that balance their ability to diffuse across the tumor interstitium and accumulate inside cells.[30] However, these payloads are ultra-potent with

very high toxicities causing their maximum tolerable dose (MTD) in the clinic to be limited, e.g. ~ 0.3mg/kg for PBD-based ADCs compared to 3.6mg/kg for Kadcyla®.

In this study, we used a combination of experimental and computational work to evaluate ADC modalities and the most important properties of TAK-164 that explains the results from the coadministration of this ADC. Next, I will present the experimental data that led to our research questions.

Distribution and Uptake in Vivo and Comparison with Toxicity in Vitro

Experiments showing the distribution of TAK-164 in histology tumor slices using fluorescence microscopy performed by Dr. Eshita Khera demonstrate better penetration with higher dose (1.5mg/kg compared to 0.4mg/kg) (Fig 4.1.A). In this experiment, mice bearing PHTX 11C tumors were intravenously administrated 0.4 mg/kg or 1.5mg/kg of TAK-164 conjugated to the fluorophore Alexa Fluor 647. Stromal macrophages and untargeted receptors were stained *ex vivo* using anti-Mac-3 antibody conjugated to Alexa Fluor 488 and 5F9 conjugated to Alexa Fluor 750 respectively. As seen in Figure 4.1.A, for lower dose (0.4 mg/kg on the left panel) TAK-164 in green is distributed very heterogeneously, and 5F9 in cyan shows high prevalence of untargeted receptors and acinar pockets throughout the tumor. The higher dose (1.5 mg/kg on the right panel) penetrates deeper in the tumor tissue showing an improvement in distribution. The *ex vivo* staining for unbound receptors, however, reveals that there are still many receptors unbound at this higher dose, including a few acinar pockets, supporting that 1.5 mg/kg of TAK-164 is still sub-saturating. Additionally, the persistence of acinar pockets with high densities of receptors suggests that some fraction of receptors in cells in clinical tumors may have reduced accessibility by the *in vivo* administered dose (either due to physical barriers in the form of tight junctions or a dynamic

binding site barrier).[151]

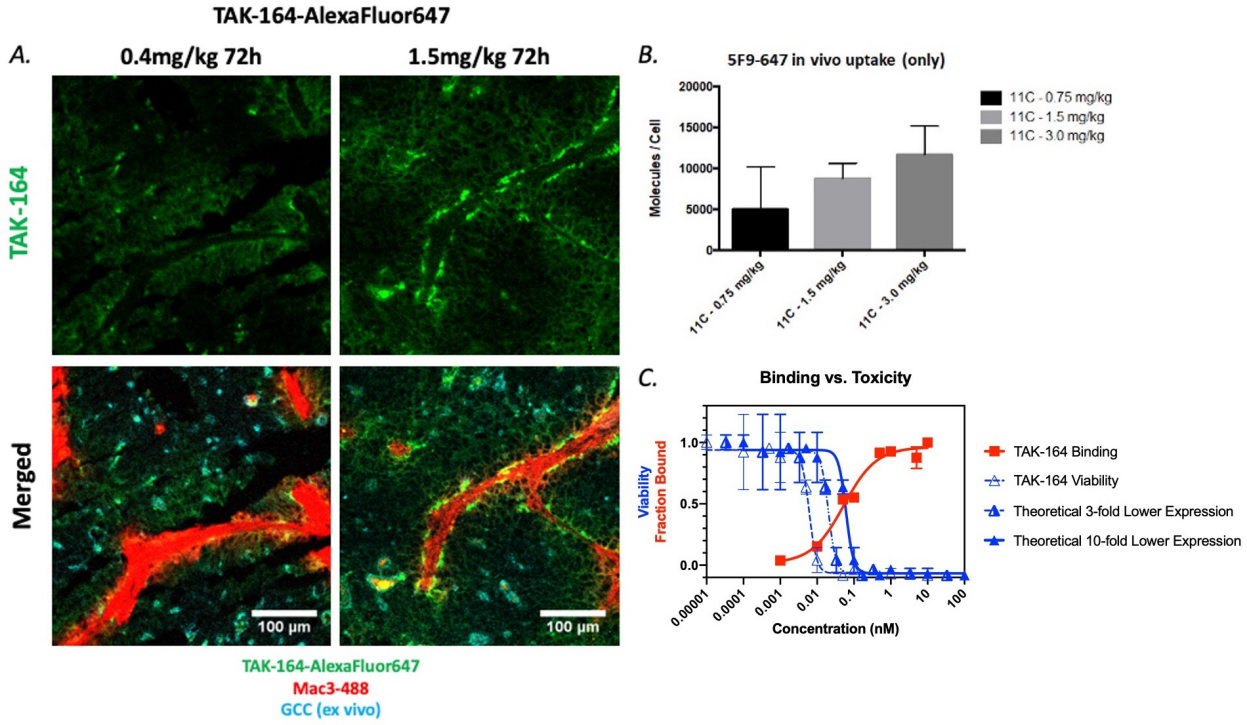

Figure 4.1 Increased distribution of TAK-164 with increase of the dose.
(A)The increased antibody dose increases tissue penetration and antibody uptake while still at a subsaturating dose. Blood vessels (not shown) are exclusively in regions of macrophages (Mac 3 in red). The TAK-164-Alexafluor 647 (green) distributes in a perivascular distribution reaching most cells at a 1.5 mg/kg dose at 3 days. More regions of untargeted antigen (cyan) are seen with the lower dose. Unpublished data collected by Dr. Eshita Khera. (B) 5F9 conjugated with Alexa Fluor 647 were giving to in vivo xenograft model at doeses 0.75, 1.5, and 3 mg/kg. Unpublished data collected by Dr. Cornelius Cilliers. (C) Viability and binding affinity of TAK-164 in HEK-293-GCC cells reveal that the potency in HEK-293-GCC cells in vitro is higher than expected in the lower expressing PHTX models.

Experimental uptake of the antibody 5F9 in xenograft models was measured by Dr. Cornelius Cilliers, and results are shown in Figure 4.1.C. In this experiment, the 5F9-AF647 was injected intravenously at 0.75, 1.5 and 3 mg/kg into PHTX 11C tumor bearing mice that were euthanized 24 hours post injection. The tumor was digested into a single cell suspension that was analyzed by flow cytometer, and the median fraction of receptors targeted was estimated as shown in Figure 4.1.B. As the dose increases, the uptake of antibodies per cell also increases. However,

doubling the dose from 0.75 to 1.5 mg/kg almost doubles the number of molecules per cell, but doubling the dose from 1.5 mg/kg to 3mg/kg only increases the number of molecules per cell approximately 25%. This uptake data suggests that saturation occurs when approaching doses of 3mg/kg doses.

The efficacy of TAK-164 was determined in vitro using HEK-293-GCC cells (since the PHTX models cannot be grown as cell lines) and compared with the binding affinity of the antibody 5F9 to GCC cells. HEK-293-GCC with ~10^5 GCC receptors per cell was used to test the toxicity of TAK-164 and binding affinity of 5F9 to the antigen as shown in Figure 4.1.C. The results demonstrate that the IC_{50} in these cells are 4.6 pM while the binding affinity was about 51 pM. Since potency is typically proportional to payload delivery, a 10-fold lower expression would result in ~10-fold lower potency (~46 pM). Despite the similar potency and binding affinity, the sub-saturating dose and heterogeneous distribution led us to test whether a carrier dose could improve efficacy in vivo.

Coadministration of 5F9 and TAK-164 Does Not Improve Efficacy as Expected

Dr. Eshita Khera evaluated the benefit of the coadministration of 5F9 antibody and TAK-164 in primary human tumor xenograft model 11C PHTX with 20,000 to 30,000 GCC receptors per cell when analyzed for receptors expression *ex vivo*.[147] When tumors reached ~ 100mm^3, the mice were injected with 1.5 mg/kg dose of 5F9 (4:0), 0.4 mg/kg of TAK-164 (0:1), coadministration of 1:1 and 3:1 of 5F9 with TAK-164, and only saline for the control. As seen in Figure 4.2, coadministration of 5F9 and TAK-164 did not improve the efficacy. Given the multiple demonstrations of higher antibody doses and improved distribution increasing efficacy, this was unexpected. [14, 21, 31, 146]

There are multiple mechanisms that could explain a lack in improved efficacy, which are difficult to test exclusively with animal experiments. Here, I use the computational platform presented previously (Fig. 4.3) in conjunction with the experimental data to determine the reason for a lack of improvement in efficacy despite improved tissue penetration. The mechanisms tested include: 1) a more diffuse binding front at low expression levels, 2) less 'overkill' in the PHTX models, 3) diminishing tumor uptake close to saturation, or 4) efficient bystander effects mitigating the benefit of a carrier dose. Conceptually, these mechanisms equate to 1) 'filling up' the first cell layer rather than increasing tissue penetration with a carrier dose, 2) the loss in potency on targeted cells compensating for the increase in the number of targeted cells, 3) a reduction in the total amount of payload in the tumor due to tumor saturation (blocking binding), and 4) the bystander payload reaching all cells regardless of the antibody dose.

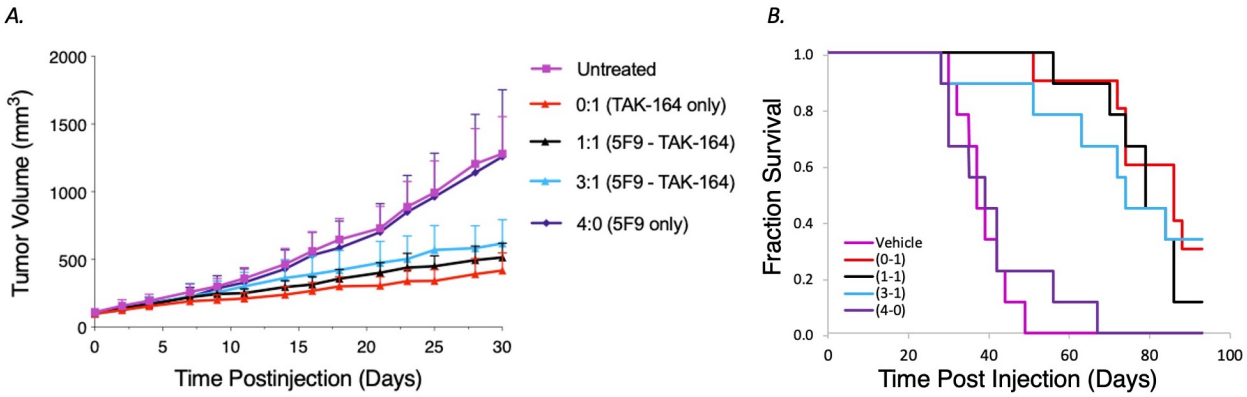

Figure 4.2 TAK-164 Efficacy and Survival with Carrier Dose
Despite previous reports of heterogeneous uptake of TAK-164 in 11C PHTX tumors, a carrier dose does not improve tumor growth (A) or survival (B). Unpublished data collected by Dr. Eshita Khera.

4.3 Methods

As mentioned earlier, this work was performed in collaboration with Dr. Cornelius Cilliers and Dr. Eshita Khera who provided all experimental data that were explored with the computational model presented in Chapters 2 and 3 and updated here. In this chapter, I only

mention the most important aspects of the experimental methods and results. For more information on the experimental methods, the reader can find it in [15, 21, 115, 146]. The model is a 2D representation of a tumor section that contains cells and blood vessels, as described previously. The cells and blood vessels have different states, i.e., alive or dead for cells and functional and non-functional for vessels, and they occupy specific positions on the simulation grid. Each cell occupies a volume of 2 x 10^{-12} L (12.6 μm side grid), and the initial tumor (~1940 cells) is assumed to be representative of an initial tumor volume range of 75-150 mm^3. ADCs enter the tumor through active blood vessels, the density of which changes based on vessel dynamics presented in Chapter 3. Cells change their state from alive to dead based on the concentration of payload bound to DNA inside the cell. The computational model was updated from the model in Chapter 2 and 3 to capture the specific TAK-164 internalization, uptake, and payload kinetics.

Computational model

. The model is a 2D representation of a tumor section that contains cells and blood vessels, as described previously. The cells and blood vessels have different states, i.e., alive or dead for cells and functional and non-functional for vessels, and they occupy specific positions on the simulation grid. Each cell occupies a volume of 2 x 10^{-12} L (12.6 μm side grid), and the initial tumor (~1940 cells) is assumed to be representative of an initial tumor volume range of 75-150 mm^3. ADCs enter the tumor through active blood vessels, the density of which changes based on vessel dynamics presented in Chapter 3. Cells change their state from alive to dead based on the concentration of payload bound to DNA inside the cell. The computational model was updated from the model in Chapter 2 and 3 to capture the specific TAK-164 internalization, uptake, and payload kinetics.

Simulation Environment

We extended our hybrid agent-based model of Chapters 2 and 3 to incorporate additional physical and biological phenomena that occur for TAK-164, its payload DGN549, and the tumor environment. Briefly, our model is comprised of cells and blood vessels that behave based on probabilistic rules and their microenvironment. The previous model described: plasma dynamics (clearance), drug dynamics (ADC mechanism for bystander payloads), cell dynamics (e.g., cell division, death, expression type), and blood vessel dynamics that impact the tumor volume in our simulations. Here, we extended the model to include: 1) internalization of the antibody 5F9 and TAK-164, 2) uptake dynamics *in vivo*, and 3) payload with bystander effects which binds irreversibly. These additional features allow us to test how different mechanisms impact the efficacy of coadministration.

To independently test these different mechanisms, we updated our computational model to include the parameters relevant for TAK-164 in the PHTX-11C model. All the parameters and rates constants for the model dynamics are shown in Table 4.1.

Bystander Mechanism for DNA Alkylating Payloads

Drug dynamics with general bystander effects have been published previously using the Krogh cylinder model[30] and introduced in Chapter 3. The equations of the same are shown in appendix C.1-C14, with the slight modification in the binding kinetics (reversible for payloads such as MMAE and DM1, irreversible for DGN549). Briefly, as shown in Figure C.1.A and C.1.B, TAK-164 and the antibody 5F9 are cleared from the plasma, leave the blood vessels, diffuse through the interstitial tissue, bind to GCC receptors on cancer cells, and are internalized. After

TAK-164 is degraded in the lysosomes, the payload DGN549 enters the cytoplasm, irreversibly binds to DNA or escapes the cell and enters into neighboring cells.

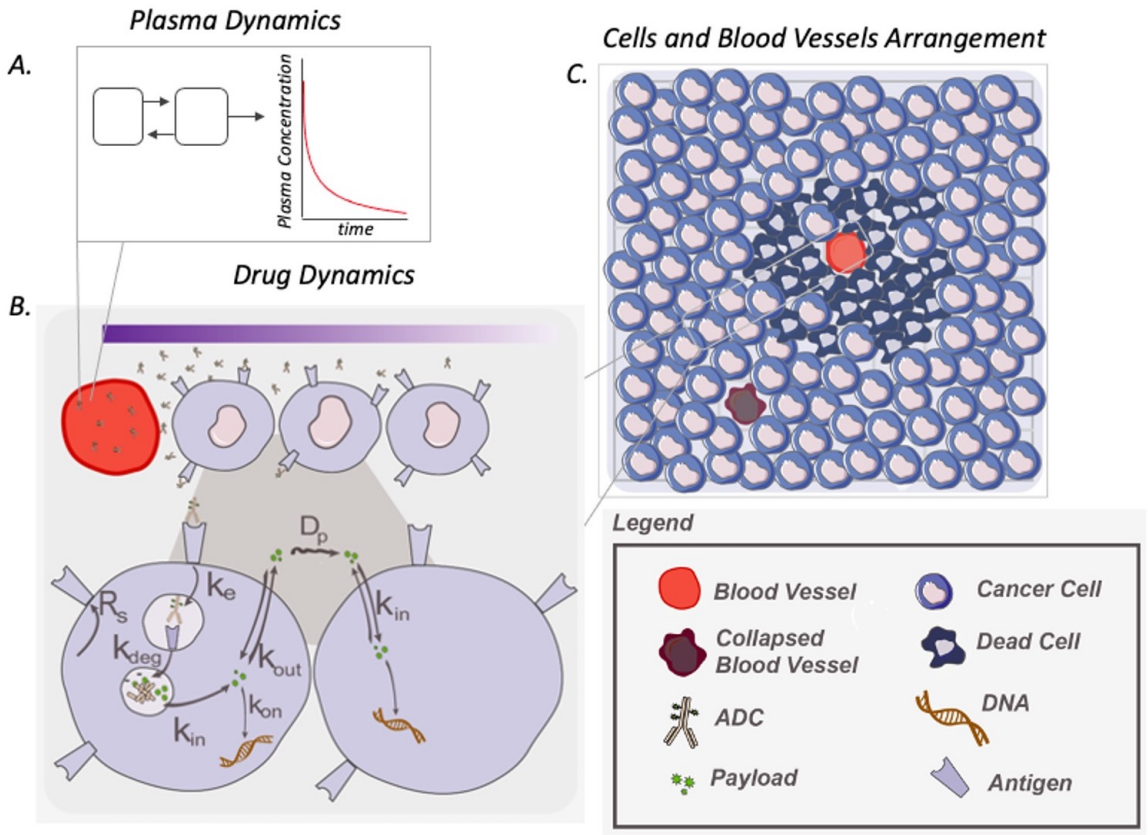

Figure 4.3 Model Schematic
(A) Plasma Dynamics for TAK-164 and 5F9. (B) Drug dynamics unreversible reaction of the payload DGN -549 and DNA. (C) Cells and blood vessels act as agents to capture the 11C dynamics and efficacy.

Model of in Vitro Internalization of 5F9

Internalization of 5F9 produces a rapid downregulation followed by recovery of the GCC receptors[147]. The same internalization was incorporated in a cellular model where it is assumed that all cells are exposed to 30nM of 5F9, and the internalization of free and bound receptors are different ($k_e < k_{eBound}$) and change from the first phase of the internalization dynamics (downregulation) to a second phase (recovery). In the ABM when agents are solved, the fraction

of receptors bound (fb) on each cell is calculated. If the cell being solved has a fraction of receptors bound greater than fb, an internal clock starts for that cell. Once the internal clock reaches the time to change the phases (t_{change}), the internalization k_e and k_{eBound} changes to the slower k_{e2} and $k_{eBound2}$.

Table 4.1 Model Parameters

Parameter	Value	Unit	Description	Reference
k_{TT}	1.47 x 10^{-5}	s^{-1}	Total antibody clearance^	measured
k_{12}	4.29 x 10^{-4}	s^{-1}	Antibody clearance from compartment 1 to 2^	measured
k_{21}	4.81 x 10^{-4}	s^{-1}	Antibody clearance from compartment 2 to 1^	measured
V_1	1.2 x 10^{-3}	L	Volume central compartment	141
k_{TT}	9.67 x 10^{-6}	s^{-1}	Total antibody clearance*	measured
k_{12}	4.33 x 10^{-4}	s^{-1}	Antibody clearance from compartment 1 to 2*	measured
k_{21}	4.79 x 10^{-4}	s^{-1}	Antibody clearance from compartment 2 to 1*	measured
K_d	60	pM	TAK-164 dissociation constant	147
k_e	$3x10^{-4}$	s^{-1}	5F9 Internalization rate constant free Rec (phase 1)	
k_{eBound}	$4.6x10^{-4}$	s^{-1}	5F9 Internalization rate constant bound Ab (phase 1)	
k_{e2}	$4.8x10^{-5}$	s^{-1}	5F9 Internalization rate constant free Rec (phase 2)	
$k_{eBound2}$	$4.8x10^{-5}$	s^{-1}	5F9 Internalization rate constant bound Ab (phase 2)	
k_{deg}	$8.0x10^{-6}$	s^{-1}	TAK-164 lysosome degradation rate constant	
k_{in}	$1.05x10^{-3}$	s^{-1}	DGN549 Payload rate constant entering cell membrane	
k_{out}	$5.53x10^{-5}$	s^{-1}	DGN Payload rate constant leaving cell membrane	
k_{on}	$3.2x10^{-11}$	nMs^{-1}	DGN Payload binding rate to microtubules	
k_{off}	0	s^{-1}	DGN Payload unbinding rate to microtubules	
DAR	2.9	-	Drug to antibody ratio	
R_s	Ke*To	M/s	Target synthesis	
ε	0.24	-	Intracellular void fraction	
ε_p	0.44	-	Intracellular void fraction for payload	
D_p	1.4 x 10^{-11}	cm^2/s	Diffusivity	
D	1 x 10^{-11}	cm^2/s	Diffusivity	
P	3 x 10^{-9}	m /s	Vascular permeability	
P_p	1 x 10^{-6}	m /s	Vascular permeability payload	
R	18	m /s	Payload partition coefficient	
GCC_o	3 x 10^3-3 x 10^5	rec/cell	Total number of targets per cell	-
fb	0.4	-	Fraction of receptors bound before switch internalization	Calibrated
t_{change}	6	hrs	Time for switch from phase 1 to phase 2	Calibrated
P_{max}	0.011	-	Maximum probability for cell killing	Calibrated
K_m	3.5	nM	Michaelis-Menten constant	Calibrated
t_d (*in vivo*)	7-10	days	*In vivo* doubling time	Calibrated
t_d (*in vitro*)	1-2.5	days	*In vitro* doubling time	Estimated

^ for dose 0.4 mg/kg
* for dose 0.75 mg/kg or higher

Model of the uptake in vivo

The *in vivo* uptake was incorporated into the model to mimic the experimental uptake setup. In the experiment, the 5F9-AF647 was injected into nude mice bearing PHTX 11C tumors (~ 250mm^3) at 0.75, 1.5, or 3mg/kg. At 24 hours, the mice were euthanized, the cells digested and processed in flow cytometer. The calculation for uptake for molecules per second is:

$$\text{Uptake} = \frac{\sum_1^n (5\text{F9bound} + 5\text{F9int} + \text{dye}).10^{-9}.V_{cell}.Av}{n} \quad (19)$$

Where Uptake is in $\frac{molecules}{cell}$, $5F9_{bound}$, $5F9_{int}$, and dye are the concentration in nM of 5F9 bound on the surface of the cell, 5F9 internalized, and residual dye respectively. V_{cell} is the volume of the cell ($2x10^{-12}$L), Avg is Avogadro number ($6.022x10^{23}$ molecules/mol), and n is the number of cells in the simulation.

4.4 Results

Calibration to the Experimental Data

The model PK and PD were calibrated to experimental data *in vitro* and *in vivo*. First the model PK was calibrated for average effective receptor per cell, the time to change the phases (t_{change}) for internalization, and fraction of receptors bound (fb) are shown in Appendix Figure C.2. The best fit values were 3000 receptors per cell, t_{change} = 6 hours, and fb = 0.4. Since this model does not grow as a cell line, and it was not possible to evaluate the trafficking and downregulation of the model relative to HEK-293-GCC cells, the expression level was fit to match in vivo cell uptake measurements.

Next, we calibrated the model to the *in vivo* pharmacodynamics. First, cell proliferation was calibrated to the in vivo efficacy of the saline control as shown in Figure 4.4.A, and the doubling time for these tumors were found to range from 7 to 10 days. Then, the probability of

cell killing, given by Equation 15 in Appendix C, was calibrated to give P_{max} equal to 0.011 and K_m = 3.5nM as shown in Figure 4.4.B. The model was validated by comparing the predicted efficacy to that observed with coadministration of 1:1, 3:1, and in vitro potency as shown in Figure 4.4.C-D. The same probability of cell killing were used in vitro and compared to the experimental data (Figure 4.4.E). These results demonstrate that our model was appropriately calibrated and validated.

Benefit of the Coadministered Antibody Is Not Observed in Tumors with Low Receptor Expression

To test if the lack in benefit of coadministration was a function the low receptor availability, we simulated tumors with different average receptor expression. In Figure 4.5 we show the distribution of the payload DGN549 and efficacy of the TAK-164 with different coadministration regimens of 0:1, 1,1, 3:1, and 8:1. Although the ADC distributes heterogeneously at low receptor expression (3K GCC per cell in Appendix Fig. C.3), the bystander abilities of DGN549 help the payload to reach most cells in the tumor, leading to efficacy. When the receptor expression increases to 30K GCC per cell, we see an increasing benefit from coadministration leading to best efficacy at regimens 8:1. However, when the average receptor expression is increased to 300K GCC per cell, coadministration shows no significant changes in the efficacy. This last scenario exemplifies a scenario where the carrier dose is not sufficient to improve tissue penetration and simply increases cell binding within the saturation front.

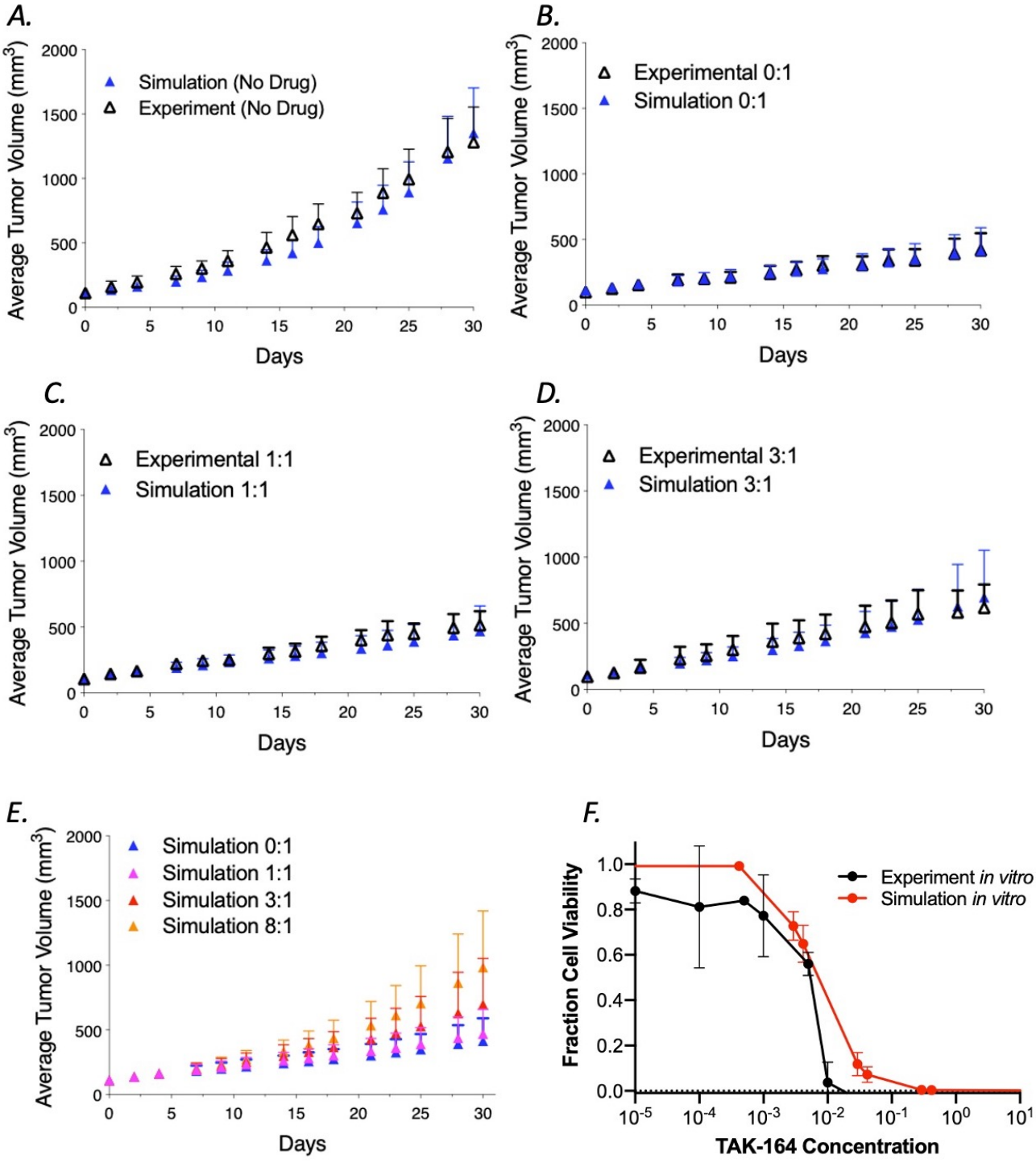

Figure 4.4 Calibration of *in vitro* and *in vivo* pharmacodynamics and validation.
(A) In vivo proliferation (B) *In vivo c*ell death calibration for single administration of 0.4mg/kg of TAK-164 (C -D) Validation *in vivo* for coadministration 1:1 and 3:1 with 5F9 to TAK-164. (E) Comparison between *in vivo* curves. (F) In *vitro* toxicity validation with the parameters calibrated *in vivo* .

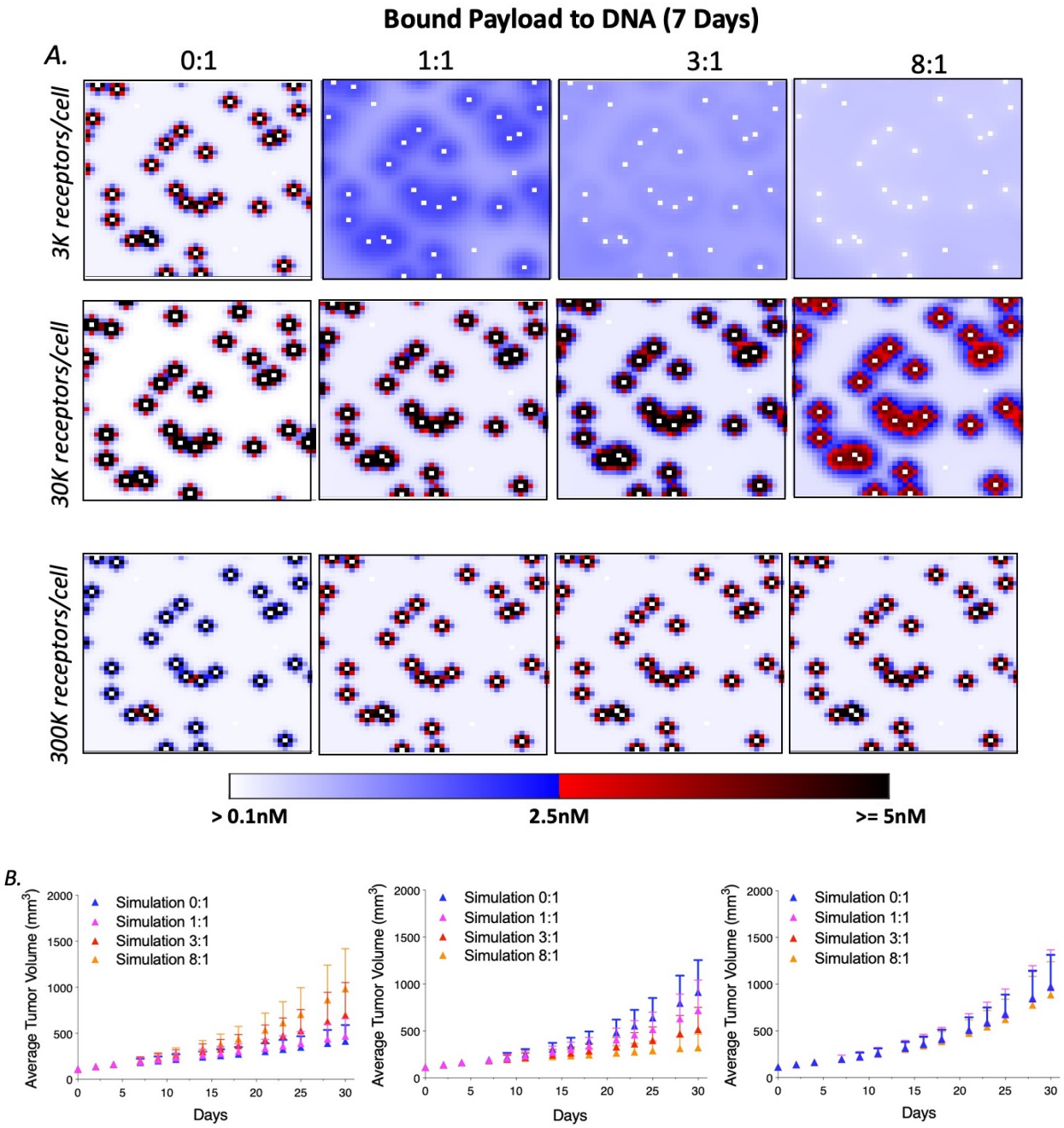

Figure 4.5 Prediction of distribution and efficacy in tumors varying receptor expression: Distribution of the payload DGN549 at day 7 (A) and Efficacy at day 50 (B) of the coadministrations of 5F9 and TAK-164 (0:1, 1:1, 3:1, 8:1) in tumors with an average of 3K, 30K, and 300K receptors/cell.

To test if the lack in benefit of coadministration was a function the low receptor availability, we simulated tumors with different average receptor expression. In Figure 4.5 we show the distribution of the payload DGN549 and efficacy of the TAK-164 with different coadministration

regimens of 0:1, 1,1, 3:1, and 8:1. Although the ADC distributes heterogeneously at low receptor expression (3K per cell in Appendix Fig. C.3), the bystander abilities of DGN549 help the payload to reach all the cells in the tumor with low receptor expression, leading to efficacy. As the receptor expression increases, we see an increasing benefit from coadministration leading to best efficacy at regimens 8:1. However, as the average receptor expression increases to very high levels, coadministration shows no significant changes in the efficacy.

Bystander Effects Improves Efficacy in Heterogeneous Tumors with Higher Receptor Expression

To test the impact of bystander effects in tumors with increasing receptor expression, we compared simulations with bystander effects to those eliminating the ability of the payload to enter adjacent cells (by setting the internalization rate constant to zero ($k_{inp} = 0$)) and administering 0:1, 1:1, 3:1, and 8:1 doses. As seen on Figure 4.6A, regimens with bystander and non-bystander effects have similar efficacy for tumors with low receptor expression. However, for tumors with moderate receptor expression (~30K), eliminating bystander effects worsens the efficacy in these tumors for all coadministrations. This data suggests that the benefit of the carrier dose is more pronounced in the tumors with high expression when administering a carrier dose. Eliminating the bystander effect does not disturb direct cell targeting by the ADC, which is predicted to exhibit better efficacy than bystander effects alone. As a result, the simulations do not show any major effect on efficacy in the low receptor expression tumors. When we look at tumors with moderate receptor expression (30K), the benefit of the bystander effects is more evident. In more heterogeneous tumors, the ADC cannot directly target all the cells in the tumor, and the bystander payloads that reach these cells in the deeper tissue demonstrate a significant impact. However, as noted bystander effects are not predicted to be as efficient as direct cell targeting, which is reflected in the greater

improvement in efficacy with coadministration even when bystander effects are retained. However, comparison between the two groups with and without bystander effects suggests that direct cell-targeting and bystander effects can function in synergy to maximize efficacy.

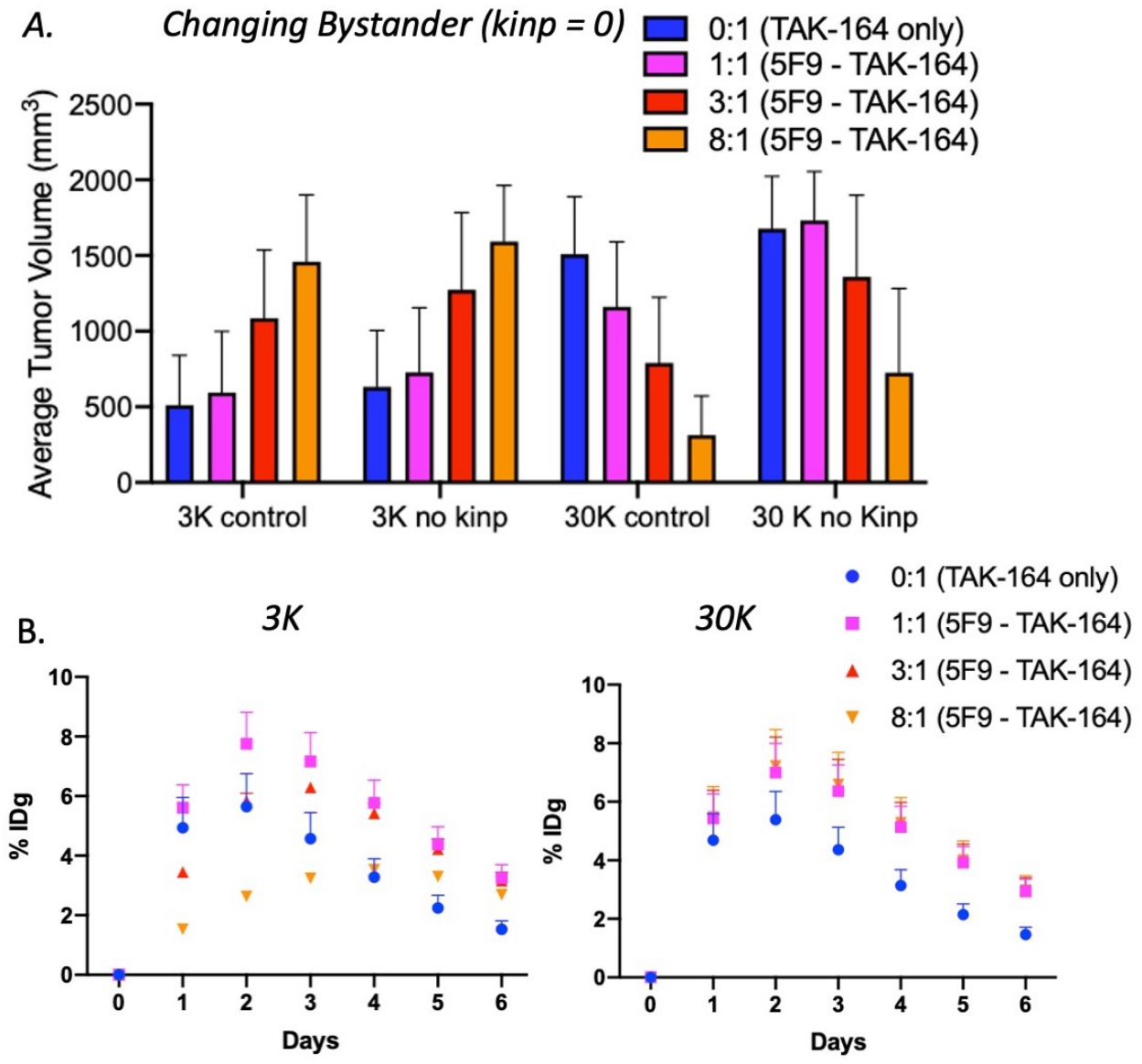

Figure 4.6 Prediction of regimens with no bystander effects and %IDg for tumors changing the receptor expression.
(A) Average tumor volume at 40 days for tumors with 3K and 30K receptors per cell with and without bystander effects. Non-bystander payloads were represented by internalization rate of the payload to adjacent cells set to zero (k_{inp}=0). (B) %IDg for coadministration in tumors with 3K and 30K receptors per cell.

Looking at the total tumor uptake of the ADC (calculated as percentage injected dose per gram of tumor tissue, %ID/g), we see a decrease in uptake at 3:1 and 8:1 coadministration regimens for low receptor expression tumors, suggesting that 3:1 and 8:1 regimes are saturating doses in comparison with 0:1 and 1:1. For tumors with moderate receptor expression, administrations 1:1, 3:1, and 8:1 show the same ADC uptake, which indicate that even at higher coadministration doses, these regimes are non-saturating. Note that for single administration, the %IDg is lower than other coadministration doses, even though ADC uptake in the tumor is dictated primarily by the vascular permeability, which is the same for antibody and ADC. This happens because at very low doses, such as 0.4mg/kg, target mediated drug disposition (TMDD) results in faster systemic clearance that reduces plasma exposure to the tumors as compared to the higher doses where the excess antibody can saturate TMDD sinks.

4.5 Discussion

The development of new ADCs involves understanding and improving the different components of the ADC and ensuring they work in concert to maximize efficacy at tolerated doses. Recently, the impact of heterogeneous delivery from some ADCs has resulted in methods to improve tissue penetration, including the use of bystander payloads and carrier doses of antibody. Bystander payloads have been explored based on the potential to reach cells that were not directly targeted by the ADC, an approach that would benefit the treatments in tumors with heterogeneous receptor expression that are known to cause treatment resistance. Payload physicochemical properties such as the payload lipophilicity and potency can impact the distribution and efficacy in the tumor. The antibody dose, target expression, and ADC internalization all impact the potential benefit of an antibody carrier dose. Understanding the payload properties and antibody tissue

penetration, in combination to that of the antibody and linker, are important for the development of better payloads and ADCs in the next generations of this drug.

TAK-164 is an anti-GCC ADC undergoing clinical evaluation for gastrointestinal cancers which present very poor prognosis. GCC is considered a great target for ADC development as GCC receptors are considered a highly specific marker for GI cancers.[153] However, GCC receptors are heterogeneously expressed between patients with differences that can vary up to 100-fold.[154] This heterogeneity, as shown throughout this chapter, can strongly influence the pharmacokinetics and pharmacodynamics of this ADC.

Understanding which characteristics of TAK-164 and 5F9 impact the efficacy of coadministration regimens can help us understand in which scenarios co-dosing with an unconjugated antibody is beneficial and recommended. Here, we explored the influence of receptor expression on the binding site barrier, uptake at sub saturating and saturating doses, the efficiency of the bystander effects, and overkill in PHTX models.

Despite multiple examples of carrier doses improving efficacy of ADCs, including animal models with only 70K receptors per cell, a carrier dose did not improve efficacy of TAK-164 in the PHTX 11C model even though it improved tissue penetration.[146] To examine the mechanism behind this lack of improvement, computational models were combined with experimental data to test four hypotheses: 1) a more diffuse binding front at low expression levels, 2) less ‘overkill’ in the PHTX models, 3) diminishing tumor uptake close to saturation, or 4) efficient bystander effects mitigating the benefit of a carrier dose.

The lower availability in receptor expression in the calibrated PHTX11C model in comparison to the receptor expression measured ex vivo affects the expected results in coadministration. As shown during the calibration to the uptake of the tumors with 0.75, 1.5, and

3 mg/kg (Appendix Fig. C.1), 3K receptors per cell demonstrated the best fit. This expression corresponds to a 10-fold decrease in the measured receptor expression reported in [147] for the PHTX11C tumor model. This lower receptor expression availability leads to a more homogeneous distribution compared to the tumor if it had 30K receptors per cell (Figure 4.5). In addition, increasing the coadministration to 3:1 and 8:1 regimen, the loss in efficacy occurs.

The lower availability in receptor expression in the calibrated PHTX11C model in comparison to the receptor expression measured ex vivo affects the results of coadministration. As shown during the calibration to the uptake of the tumors with 0.75, 1.5, and 3 mg/kg (Appendix Fig. C.1), 3K receptors per cell best fit the in vivo uptake data. This target expression corresponds to a 10-fold decrease in the measured receptor expression reported in [147] for the PHTX11C tumor model. This lower receptor expression availability leads to less heterogeneity compared to the tumor with 30K receptors per cell (Figure 4.5). A carrier dose does improve tissue penetration even though it does not improve efficacy with 3K receptors/cell. In fact, 300K receptors per cell are needed for the carrier dose to bind within the reaction front, ruling out the first hypothesis. With such a small dose (0.4mg/kg) and high expression, the first cell layer close to the blood vessel is not fully saturated and increasing the antibody dose only saturates the first cell layer with no change in efficacy (Fig 4.5).

Computational models showed that tumors with 30K receptor expression demonstrated an improvement in efficacy, consistent with previous results. Under these conditions, cell death occurs without saturating the receptors on the cell surface (Fig. 4.1), so a carrier dose can reach more cells without an equivalent drop in cell killing, consistent with the second hypothesis.

Another possible explanation for the lack of benefit from a carrier dose is efficient bystander payload penetration compensating for the heterogeneous ADC delivery. To test this

hypothesis, we set the internalization rate constant to zero ($k_{inp} = 0$) in simulations and compared it to the control simulations. Here, the bystander payload can diffuse out of the cell, but it cannot enter adjacent cells. In Figure 4.6, efficacy from bystander effects is more noticeable for tumors with moderate receptor expression than for tumors with lower receptor expression because of direct targeting of the ADC. This data suggests that in tumors with moderate receptor expression, cells that are not directly targeted by the ADC can benefit from efficacy from optimized bystander payloads.[30] However, in tumors with lower expression, the impact of the bystander killing is not important for tissue penetration, ruling out the 3rd hypothesis. Notably, bystander effects can still be important for killing antigen negative cells, and bystander effects should be studied in tumors with cell-to-cell heterogeneity.

Finally, tumor uptake data with 3K and 30K receptors per cell shows that at the 3K receptor expression, increasing the antibody co-dose to supersaturation can cause direct competition with the ADC for binding to the receptor, thus hurting efficacy. However, this does not occur until an 8:1 carrier dose, with 0:1, 1:1, and 3:1 having similar peak uptake. This rules out the fourth hypothesis that super-saturation prevented an increase in efficacy. In contrast, even at high antibody co-doses, saturation was not achieved in 30K tumors, which demonstrates improvement in the efficacy due to maximum uptake and improved distribution.

4.6 Conclusion

Understanding the different ADC properties can help develop better mechanistic approaches to increase the therapeutic window of ADCs. Here, we explored coadministration of TAK-164 with its antibody and explored its influence in a variety of scenarios such as tumors with high receptor expression, bystander efficiency, distribution and saturation, and DGN549 potency.

We found that TAK-164 coadministration only improved efficacy in tumors with increased receptor expression. This resulted from lower cell uptake relative to cell potency, so increasing tissue penetration was compensated by decreased cell efficacy. Therefore, carrier doses are only effective in moderate to high receptor expression systems (e.g. 30K receptors per cell or above under these conditions). At the expression levels found in the primary human tumor xenograft model, the cellular delivery was matched with the cellular potency without the co-administration of additional antibody. These results should help clarify when a carrier dose can improve the therapeutic window of ADCs.

Chapter 5 Concluding Remarks and Future Directions

5.1 Summary of Research Findings

In this dissertation, I have shown how we explored different ranges of ADC properties and predicted their distribution and efficacy in a variety of tumor environments. The development of the new hybrid agent-based modeling approach described here is a powerful framework that captures the mechanistic ADC pharmacokinetics using deterministic equations while also employing stochastic processes involved in drug delivery and efficacy that are not easily represented with continuous equations. This new model was used to evaluate different ADCs and dosing regimens in the complex tumor environments.

In Chapter 2, I described the development of an original framework for this model, which was subsequently updated with additional complexities in Chapters 2 and 3. This model combines continuous and stochastic approaches to capture different aspects of drug delivery that are characterized by widely different sizes (e.g., nanometer sizes of antibodies and payloads, micrometer sizes of cancer cells, and hundreds of micron distances and larger for blood vessels and tumors) and time scales (e.g., weekly doses versus target binding of molecules in seconds). Specifically, we implemented ADC dosing, plasma clearance, diffusion and molecular dynamics (binding, internalization, and degradation) to capture ADC pharmacokinetics. ADC pharmacodynamics were incorporated by including cell proliferation and cell death based on the payload concentration, all in heterogeneous solid tumors with a variety of blood vessel densities. This model helps describe the impact of different dosing regimens with antibody coadministration

and/or fractionated dosing of T-DM1 with trastuzumab in tumors with different receptor expression. We predicted that the benefit of the carrier dose is strongly dependent on average receptor expression, and an optimal co-dose exists that can achieve maximum efficacy. We also demonstrated that fractionated dosing with coadministration is only beneficial if fractionation enables an increase in the total dose administered. This study further demonstrates the potential of this complex hybrid agent-based model to mimic the clinical tumor environment with high resolution and was subsequently used to study ADC delivery with additional tumor microenvironment modifications.

In Chapter 3, we explored how ADC bystander effects can impact efficacy and selection of resistant cells in heterogeneous tumors. The previous chapter examined dosing regimens using T-DM1, which does not exhibit bystander effects. Therefore, the payload was not free to diffuse following release from the antibody. To examine bystander effects, another layer of freely diffusing payload drug was added to the equations. After adding bystander drug dynamics, angiogenesis and intratumor cellular heterogeneity were implemented in the model. Angiogenesis allowed longer-term treatment regimens by enabling tissue remodeling to capture differences in vascular delivery, while cellular heterogeneity enabled variability in target expression and sensitivity. We simulated multiple dosing regimens with bystander (T-MMAE) and non-bystander (T-DM1) ADCs, with or without trastuzumab coadministration. Intratumor heterogeneity was computationally generated with cells varying in either receptor expression or intrinsic sensitivity to the payload. Our simulations showed that coadministration is more beneficial with non-bystander ADCs, but still showing benefit with bystander payloads. This provides evidence for greater efficacy with direct cell targeting by the ADC in comparison to bystander effects of the payload alone in heterogenous tumors. Cells with high intrinsic resistant also responded well to

coadministration treatment, but more effective regimens occur with higher coadministration that also selects for more resistant cells, highlighting a trade-off. Finally, this work demonstrates the power of this highly resolved hybrid model in performing hundreds of simulations to independently delineate trends and treatment response patterns that would normally be difficult to discern due to tumor variability from individual ADC and tissue properties without large animal experiments that would not be feasible.

In Chapter 3, we employed this model to gain a deeper understanding of TAK-164 behavior in patient derived tumors that exhibit an even higher degree of tumor heterogeneity compared to pre-clinical tumor models as shown in Chapter 2. We evaluated the hypothesis that coadministration with the anti-GCC TAK-164 and its antibody 5F9 would improve distribution and efficacy in PHTX11C models. However, in vivo evaluations of efficacy presented no significant difference, despite an improvement in ADC distribution. After our model framework was updated to capture the complex internalization and uptake of TAK-164, we showed that coadministration does change the distribution of this ADC at tumors with 3K receptors per cell, reaching saturation at 3:1 and 8:1 confirmed by %IDg data. We demonstrated using our models that the lack in the benefit of coadministration with TAK-164 in PHTX11C is due to excessive dilution of the payload, resulting in underkill of tumor cells. In effect, the benefit of better penetration is completely countered by the reduction in killing efficiency of targeted cells. We also showed that the impact of the bystander in this tumor tissue is not as important in tumors with low receptor expression as in moderate receptor expression.

In summary, this thesis demonstrates the advantage of combining experimental work with a powerful hybrid agent-based computational model to understand the complexity of ADC delivery and hasten efficient ADC development in the clinic.

5.2 Future Work and Directions

Predicting ADC delivery and efficacy is becoming essential for faster clinical assessment and overall development. Changing the ADC regimens, depending on the tumor environment, can be important to improve efficacy, but it is still not enough to overcome treatment resistance. Hence, we need to continue to explore the potential of the ADC drug class and its vast application with new mechanisms of action. Computational models, such as the one presented here, can help us to avoid wasting resources on ADCs that are poor candidates and ultimately would fail in the clinic. In order to do this, the model developed here should be expanded to include additional important characteristics and dynamics of the tumor environment and ADCs. Examples of features to include are: distribution and uptake of oxygen and nutrients from blood vessels to cancer cells and cell death due to the lack of these resources (e.g. chronic hypoxia), resistant cancer stem cells and their dynamics, necrosis that affects cell growth and drug penetration, stimulation of immune system through Fc region and payload of ADCs, and new engineered antibodies and payloads with new mechanisms of action. All these interactions could be studied with our model and the addition of new cells and dynamics.

Although not the focus of this thesis, ADCs have been purposefully designed in part to help the immune system kill cancer cells. The IgG antibody's Fc region bridges NK cells and macrophages to cancer cells to induce antibody-dependent cellular cytotoxicity (ADCC) and antibody-dependent cellular phagocytosis (ADCP). Some payloads in ADCs are also known to stimulate the immune system. Once these payloads are released into the tumor environment, they activate dendric cells (DCs) to present antigens derived from the payload to T and B cells.[155-157] For example, the microtubule depolymerizing payload MMAE found on Brentuximab vedotin (Ab +MMAE) and the topoisomerase inhibitor, deruxtecan, in trastuzumab deruxtecan have been shown to stimulate DCs and T-cell infiltration in human lymphomas.[158, 159] PNU, a potent

anthracycline payload, has been shown to stimulate CD8+ T cells and their immunological memory formation.[160] These mechanisms can improve the durability of treatment responses by providing alternative mechanisms of action to kill resistant cells.

Antibodies have also been successful in blocking programmed death-1 (PD-1), and its ligand (PD-L1), and regulators of T lymphocyte antigen-4 (CTLA-4) pathways alone or in combination with other checkpoint inhibitors in the clinic.[158, 161, 162] These pathways can modulate killing by downregulating helper T cells, upregulating regulatory T cells (T_{reg}), or causing cytotoxic T cell exhaustion.[163] The discovery of PD-1 and CTLA-4, awarded the Nobel prize in 2018, is considered a groundbreaking discovery in the field, opening a major interest in immune checkpoint inhibitors that can overcome the cancer immunologic suppression and improve cancer treatment.[164] Besides that, these immunotherapies have also shown lower remission rates compared with cytotoxic treatments. Recently new antibodies have been developed to block these receptors and their respective pathways such as the ipilimumab (Yervoy®) against CTLA-4, atezolizumab (Tecentriq®) against PD-L1, and pembrolizumab (Keytruda®) against PD-1 receptors, all FDA-approved to be used alone or in coadministration with chemotherapy.[162, 165, 166] Studies for the coadministration of toxic ADCs, such as T-DM1, with checkpoint inhibitors, such as CTLA-4 inhibitors, have also been pursued and could be studied by expanding the model presented here.[29, 161]

Bispecific antibodies (bsAbs) are another improvement in engineered antibodies allowing two or multiple binding domains to different receptors or epitopes. This occurs through the differentiation of the Fab and/or the Fc region to change the target engagement, forming a variety of types of bsAbs used for both hematological and solid cancers with different functions.[167] BsAbs can vary in size and binding ability with or without an Fc fragment. BsAbs with an Fc region can

have Fc-mediated effector functions such as ADCC and ADCP, and bsAbs that lack the Fc region avoid off-target binding. Some bsAbs resemble an IgG structure while others only have antibody parts such as dimeric molecules (dAbs) that connect only the short variable domains and bispecific T cell engagers (BiTES, also known as Tandem scFvs) that connect different scFvs for multivalency. Some of these bsAbs bind to different receptors, such as HER2 and prolactin on the same cell, and have been shown to improve uptake and efficacy.[168, 169] Others bind to cancer cells and immune cells such as T cells and NK cells forming a trimer to trigger cell killing.[82] For example, AFM-13 which targets both CD16 on NK cells and CD30 on tumor cells, forms a trimer to induce cell killing. In addition, bsAbs that bind to cancer cells and to T-cell receptors (most commonly CD3) on both CD4+ and CD8+ T cells have demonstrated enhanced cell killing while inducing secretion of cytokines and activating other T cells.[170-172]. Finally, bsAb have also been studied as checkpoint inhibitors. For example, bispecific PD-L1 and CD47 (e.g. IGGIL2v) showed significant therapeutic effect as a stimulator for exhausted T cells and NK cells.[173-174]

Another important characteristic that can be studied by expanding the computational model developed here is the coadministration of antiangiogenic drugs and ADCs. Antiangiogenic drugs such as bevacizumab (commercially knows as Avastin®) function by inhibiting angiogenesis and ultimately the supply of oxygen and nutrients to cancer cells. Avastin® is FDA approved for coadministration with chemotherapies for advanced colorectal cancer (CRC), advanced non-small cell lung cancer (NSCLC), metastatic breast cancer (MBC), and advanced renal cell cancer.[175] This antibody mechanism of action consists of reducing tumor interstitial pressure and vascular permeability, favoring apoptosis by scarcity of oxygen and nutrients while improving chemotherapy delivery.[176] The scarcity of oxygen, counterintuitively, can also lead to the formation necrosis and a hypoxic environment that has been associated with cancer stem cells,

resistance, and poor clinical outcome, leading to the search of an important balance for optimal treatment approaches.[177] In addition, the coadministration of bevacizumab with antibodies such as trastuzumab and cetuximab (anti-EGFR) or immune checkpoint inhibitors has also been investigated. Expanding the model here could allow for a thorough examination of potential drug regimens.

The examples highlighted above show the complexity of the tumor microenvironment during treatment, whether it is immune cells trafficking to the tumor and killing cancer cells while they interact with ADCs or therapeutics that modulate the vascular density and permeability impacting delivery. By simulating the results of monotherapy and drug combinations, rational approaches can be used to design preclinical studies in vivo and importantly, scale the results to the clinic. Together, these simulations provide a powerful tool to guide the development of complex therapeutics such as ADCs and beyond.

Appendices

Appendix A Supporting Information for Chapter 2

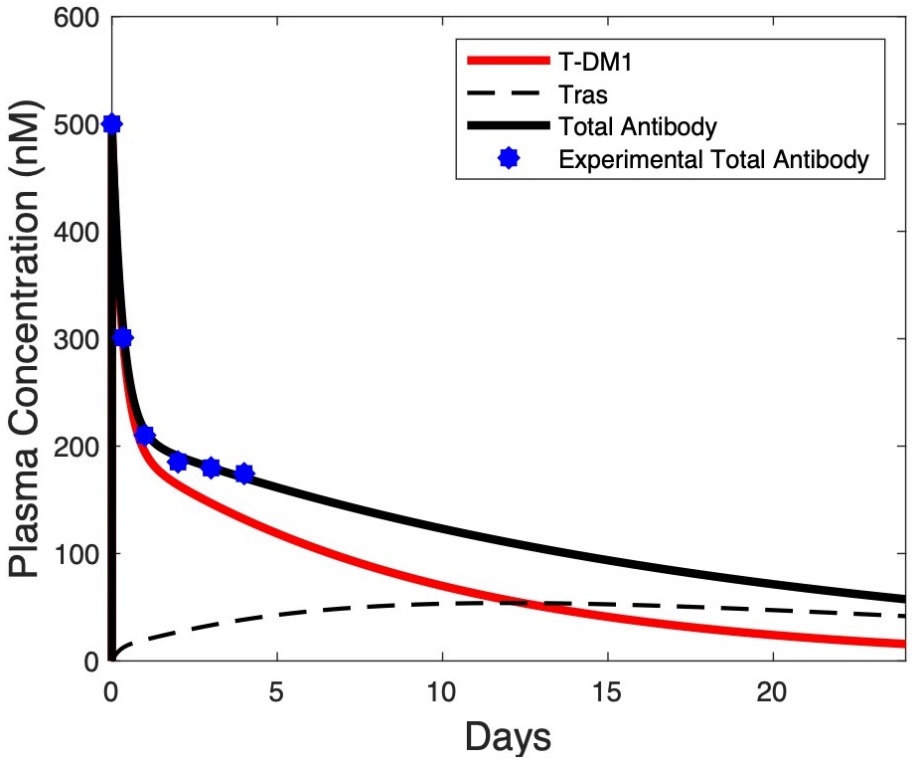

Figure A.1 T-DM1 plasma clearance.
Rates for antibody and T-DM1 clearance (CL_{TT}, CL_2, CL_{DEC}) were calibrated to experimental data [115] and literature [22].

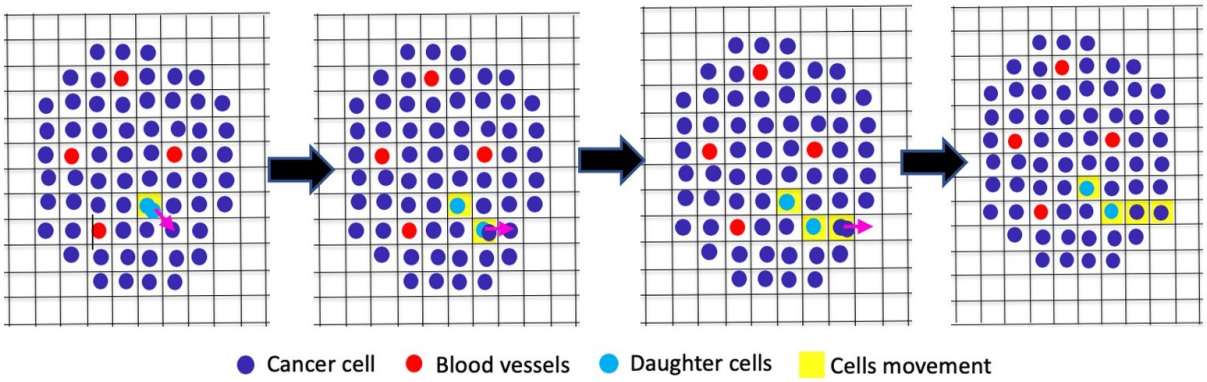

Figure A.2 Cell shuffling algorithm

We assume that at all times cells are close to each other. After cell proliferation and removal of any dead cells from the grid, cells "shuffle" to fill empty grid compartments while also maintaining only one cell per grid compartment. First, cells shuffle to make room for all daughter cells that proliferated on that agent time step, and then the tumor contracts to remove all empty spaces inside the tumor. For the tumor growth/expansion following cell division, two daughter cells are formed. One cell remains in the original grid compartment, and the other displaces the neighboring cell that is closest to an empty grid compartment or border. The newly displaced cell then displaces the next cell that is closest to that same empty grid compartment or border. If there is more than one empty grid compartment with the same distance, one of the compartments is chosen randomly. This shuffling algorithm repeats until only one cell occupies each grid space. Dead cells were estimated to leave the grid at 2.5 days based on observations of our published data, which show that maximum degradation occurs between 2 and 3 days and lower tumor volume decrease around 5 days.[31] Model results have low sensitivity to this parameter (Appendix Fig. A.3). When a dead cell is removed from the grid, an empty grid compartment is left. In this case, cells are shuffled from the farthest point on the border of the tumor (i.e. they collapse from the most protruding region of the tumor edge). This process is similar to the growth/expansion but in the opposite direction with the furthest cell displacing a neighboring cell that is closest to the empty grid compartment until a cell fills that empty grid compartment.

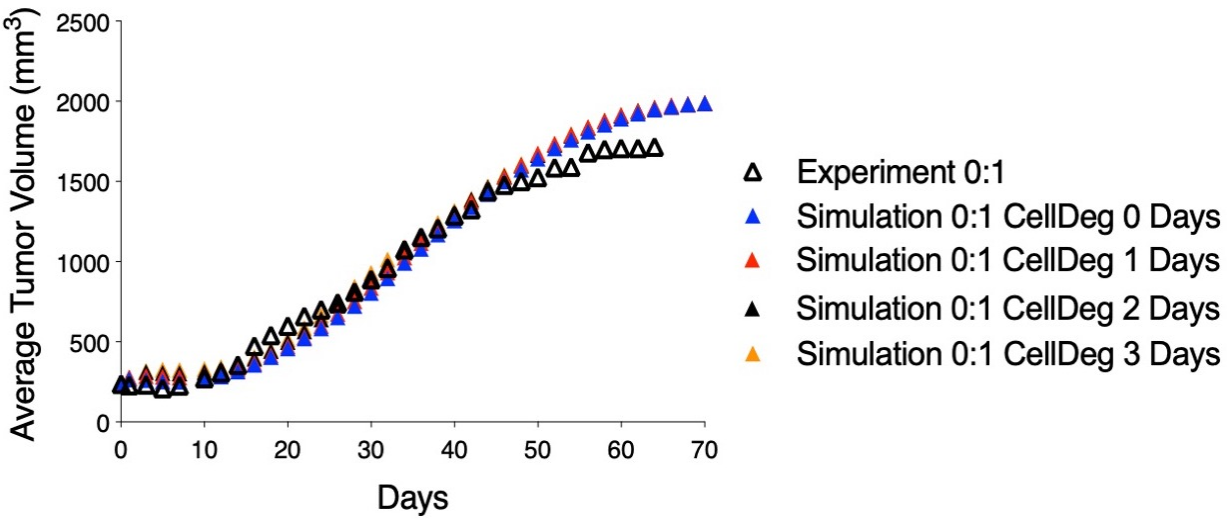

Figure A.3 Effect of cell degradation time parameter on tumor volume
Simulations were run with cell degradation times varying from 1-3 days; the average of 100 simulations is plotted.

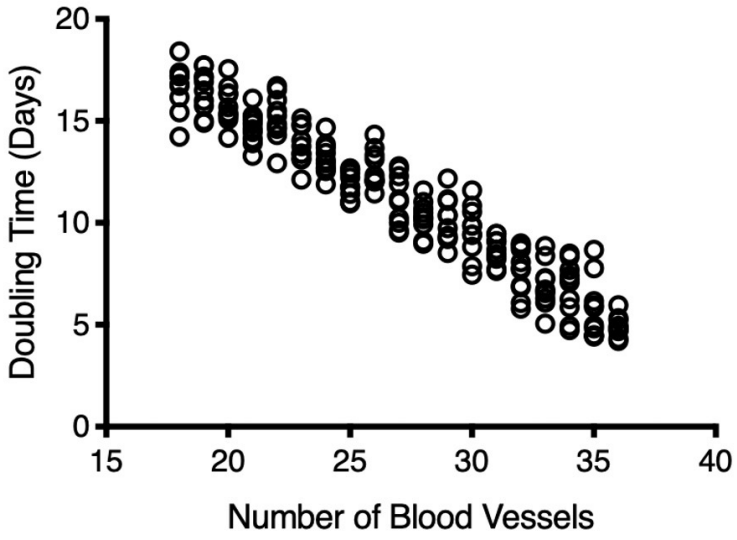

Figure A.4 Relationship between blood vessel density and doubling time.
Tumors with lower blood vessel density should have a higher cell doubling time t_d to account for hypoxic areas which often show lower proliferation [122]. Here, we assume a linear relationship between the ranges of possible number of vessels for the simulation (18 - 36) and the doubling time (5 - 17 days). For each simulation, the doubling time is chosen from a normal distribution in which the mean is provided from this linear relationship, and the standard deviation is 1 day. Ten simulations with each value of blood vessel density are plotted to demonstrate the corresponding doubling time.

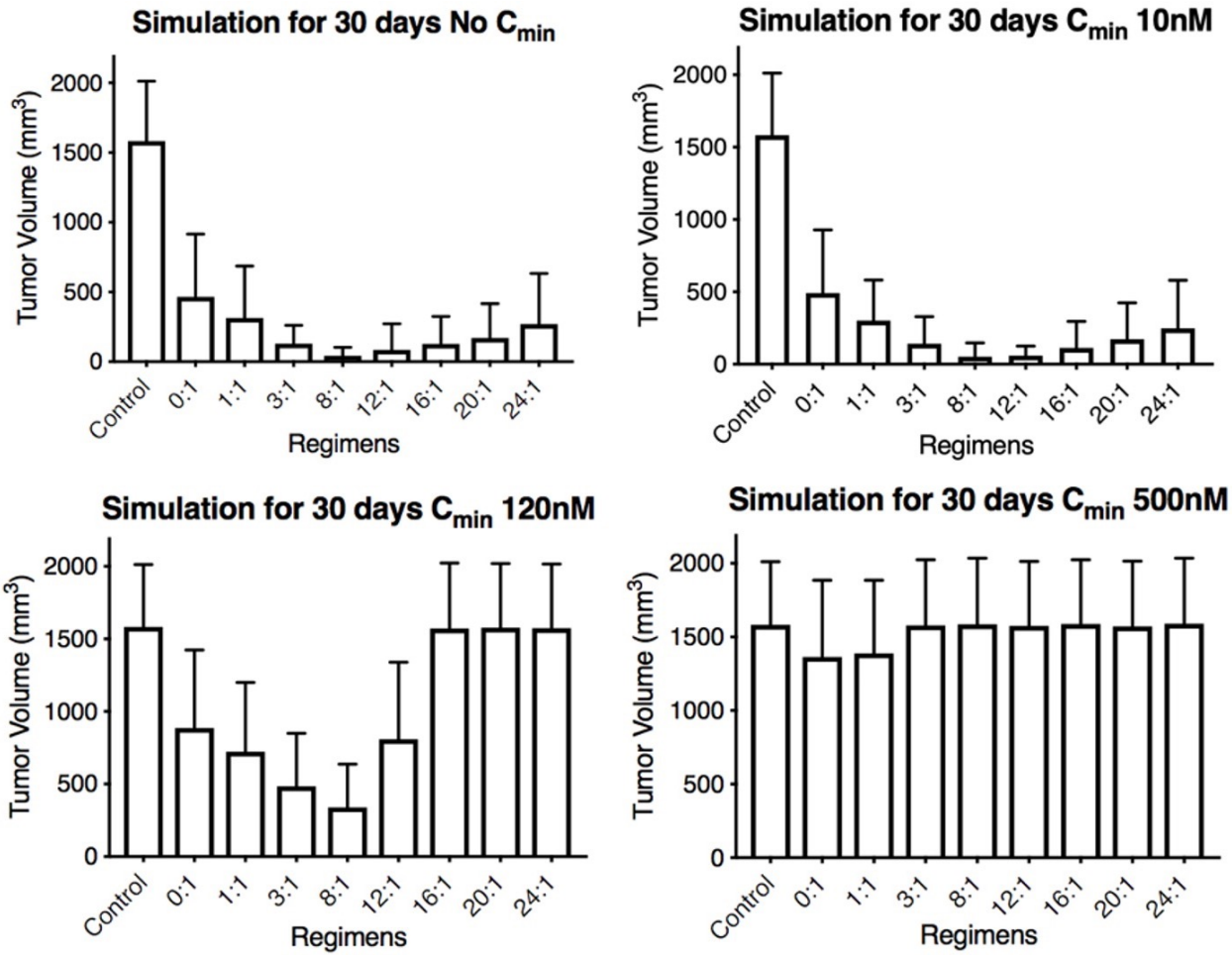

Figure A.5 Comparison of treatment regimens for drugs with different C_{min}.
Prediction of regimens with coadministration of trastuzumab and T-DM1 with a hypothetical without minimum threshold and for 10nM, 120nM, and 500nM C_{min} at 30 days.

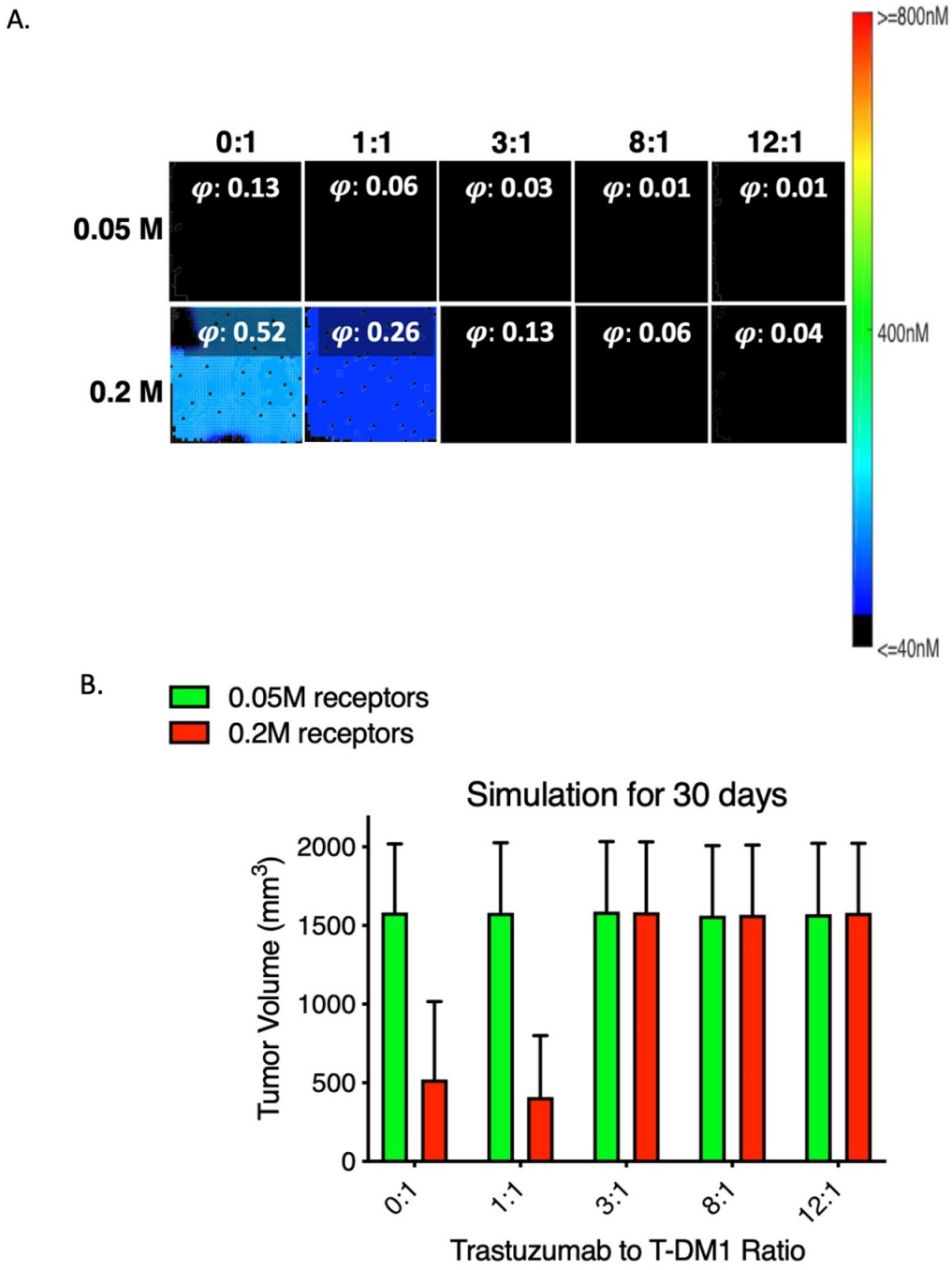

Figure A.6 Distribution and efficacy for tumors with an average of 50,000 receptors/cell and comparison with 0.2M

(A) T-DM1 bound for 0:1, 1:1, 3:1, 8:1, and 12:1 distribution and comparison with distribution 200,000 receptors/cell with Thiele modulus displayed. (B) Efficacy predictions for 50,000 and 200,000 receptor/cell tumors at 30 days. There is no efficacy for tumors with 50,000 receptors/cell even at clinical doses.

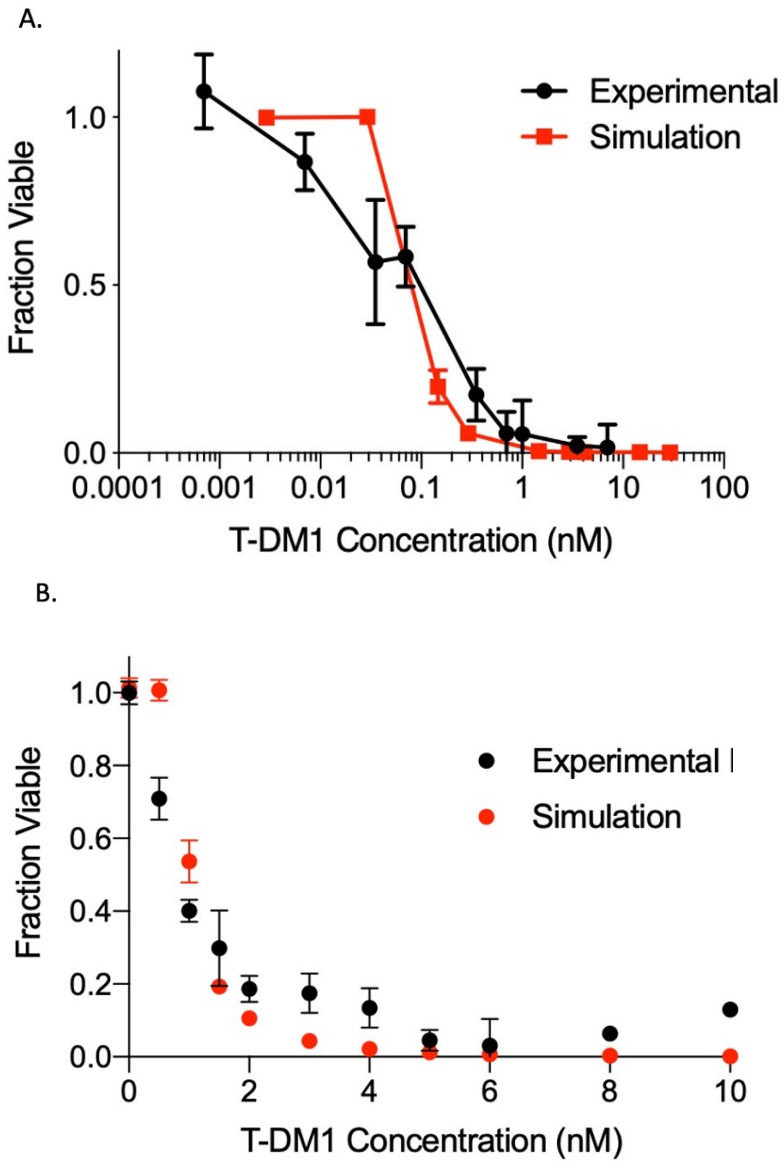

Figure A.7 *In vitro* simulations and comparison with experimental data
(A) Toxicity assay showing the fraction of viable NCI-N87 cells incubated for 6 days with different concentrations of ado-trastuzumab emtansine (T-DM1). (B) Viability of NCI-N87 cells following coincubation of trastuzumab and T-DM1 ratio (kept at a constant total antibody concentration of 10nM and varying the fraction of T-DM1) and comparison with experimental data[31] (normalized to trastuzumab treatment account for the effect of trastuzumab alone). Both of these results indicate that the cell killing parameters fit to the *in vivo* data are similar to the sensitivity *in vitro*.

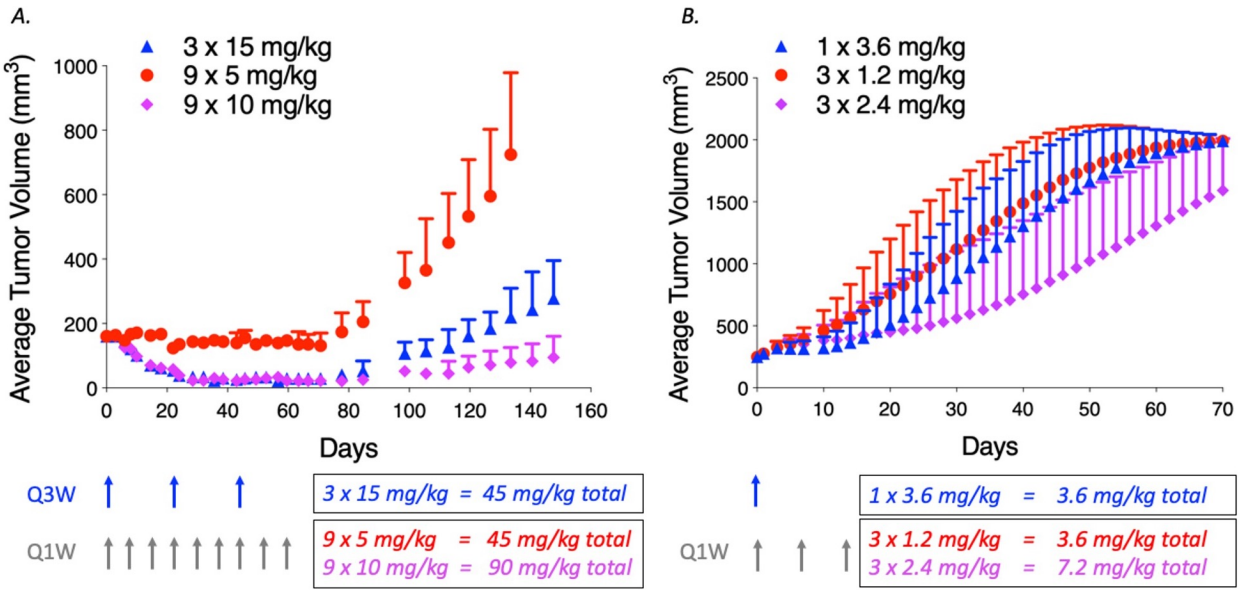

Figure A.8 Fractionation of T-DM1 and qualitative comparison with literature
(A) Results from Jumbe, N. et al. using a BT474EEI xenograft model that is resistant to trastuzumab.[110] Data was extracted using 'Data Thief' software. Fractionated dosing leads to worse overall efficacy, but with higher total doses (enabled by fractionated dosing), the efficacy improves. (B) The model simulation for fractionated dosing in NCI-N87 cells is replotted from the manuscript for convenience. The dose frequency (once weekly 'Q1W' versus every three weeks 'Q3W') and dose escalation enabled by fractionation (2-fold increase) are the same for both studies, but the doses and number of cycles are different. Note that the x and y axes are also different. Despite these differences, the overall trend is the same: fractionation has similar or worse efficacy compared to single dosing, but fractionated dosing can improve efficacy if it enables larger total doses to be administered.

Methods A.1 Estimating the minimum concentration of T-DM1 necessary to kill a cell

We estimated the minimum concentration of T-DM1 necessary to kill a cell, C_{min}, based on the concentration of T-DM1 *in vitro* that causes the first statistically significant drop in viability from *in vitro* data published in [31]. We found that at least 5% of cell receptors on NCI-N87 cells (which have ~1 million receptors per cell) must be bound by T-DM1 for any efficacy. Assuming a steady state process, with internalization (k_e) and loss rate constants (k_{loss}) of 3.3 x 10^{-5} s^{-1} and 3.94 x 10^{-5} respectively:

$DM1_{in} * k_e = DM1_{out} * k_{loss}$ and $C_{min\ is}$ ~ 120nM.

The explicit inclusion of C_{min} in the pharmacodynamic model ensures that the simulations capture the scenario where the ADC is 'diluted' too much with unconjugated antibody, lowering efficacy. Otherwise, the model choice (e.g. using a Hill coefficient less than or equal to one) may eliminate this possibility. In such a scenario, the simulations would always predict maximum efficacy by adding enough antibody to saturate the tumor, regardless of the payload potency, receptor expression, internalization rate, etc. By adding C_{min} to these pharmacodynamic (PD) models, the results are less sensitive to the subjective choice of the PD model and therefore more robust.

Appendix B Supporting Information for Chapter 3

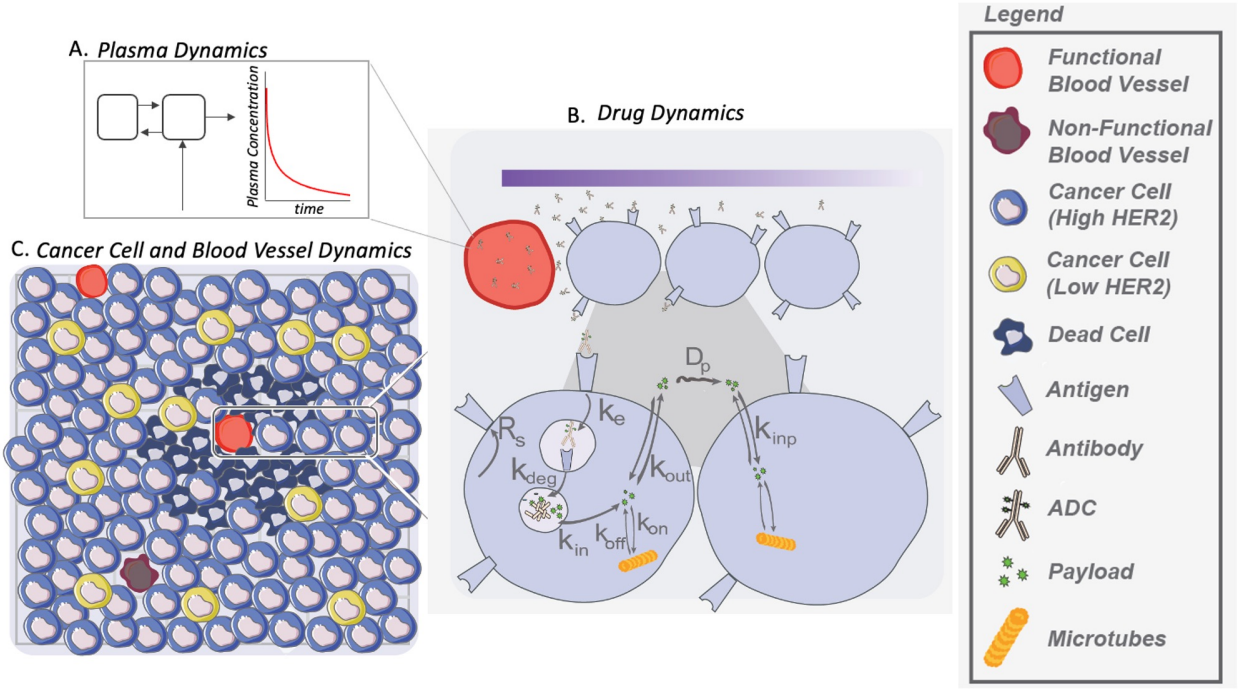

Figure B.1 Model schematic.
(A) Plasma dynamics is described with a two-compartment model (Eq. B.1-2) (B) From the blood vessel, drugs enter the interstitial tissue (Eq. B.3), diffuse through it (Eq. B.4), and bind to HER2 receptors on cancer cells (Eq B.5). There, ADCs are internalized and degraded. After the payloads DM1 and MMAE are released, they either bind to microtubes or escapes the cancer cell. From the interstitial tissue, payloads diffuse and enter adjacent cells or are washed into the blood vessels. (Eq. B.6-14). (C) Cells with high or low receptor expression or different sensitivity and blood vessels behave based on the changes in the environment. The probability of cell killing follows the Michalis Menten equation (B.15).

Plasma clearance:

$$\frac{\mathrm{d[ADC]}}{\mathrm{dt}} = -k_{10}\,.\mathrm{ADC} - k_{12}\,.\mathrm{ADC} + k_{21}.\mathrm{ADC_{p2}} \tag{B.1}$$

$$\frac{\mathrm{d[ADC]}}{\mathrm{dt}} = -k_{21}.\mathrm{ADC_{p2}} + k_{12}\,.\mathrm{ADC} \tag{B.2}$$

Newman boundary condition around the blood vessels.

$$-\mathrm{D_{eff}}\frac{\mathrm{d[ADC]}}{\mathrm{dx}} = \mathrm{P}(\mathrm{ADC_{plasma}} - \frac{ADC_{tumor}}{\varepsilon}) \tag{B.3}$$

Diffusion in 2D Cartesian coordinates

$$\frac{\partial C}{\partial t} = D\left(\frac{\partial^2 C}{\partial x^2} + \frac{\partial^2 C}{\partial y^2}\right) \tag{B.4}$$

Equations for drug dynamics:

$$\frac{d[ADC]}{dt} = -\,k_{on}\frac{[ADC]}{\varepsilon}.\left[T_{free}\right] + \,k_{off}B_{ADC} \tag{B.5}$$

$$\frac{d[T_{free}]}{dt} = R_s - \,k_{on}\frac{[ADC]}{\varepsilon}.\left[T_{free}\right] + \,k_{off}[B_{ADC}] - \,k_{on}\frac{[Ab_{free}]}{\varepsilon}.\left[T_{free}\right] + \,k_{off}[B_{Ab}] - \,k_e[T_{free}] \tag{B.6}$$

$$\frac{d[B_{ADC}]}{dt} = k_{on}\frac{[ADC]}{\varepsilon}.\left[T_{free}\right] - \,k_{off}[B_{ADC}] - k_e[B_{ADC}] \tag{B.7}$$

$$\frac{d[B_{ADC,lys}]}{dt} = k_e[B_{ADC}] - \,k_{deg}\left[B_{ADC,lys}\right] \tag{B.8}$$

$$\frac{d[P_{lys}]}{dt} = \,k_{deg}\left[B_{ADC,lys}\right]DAR - \,k_{in}\left[P_{lys}\right] \tag{B.9}$$

$$\frac{d[P_{int}]}{dt} = \,k_{in}\left[P_{lys}\right] + \,k_{in,p}\left(\frac{1-\varepsilon_p}{\varepsilon_p}\right)[P_{ext}] - \,k_{out,p}[P_{int}] - \frac{k_{on,p}}{(1-\varepsilon_p)(1+R)}\left(P_{target} - \,P_b\right)[P_{int}] + \,k_{off,p}\,[P_b] \tag{B.10}$$

$$\frac{d[P_b]}{dt} = \,\frac{k_{on,p}}{(1-\varepsilon_p)(1+R)}\left(P_{target} - \,P_b\right)[P_{int}] - \,k_{off,p}\,[P_b] \tag{B.11}$$

$$\frac{d[P_{ext}]}{dt} = \,-\,k_{in,p}\left(\frac{1-\varepsilon_p}{\varepsilon_p}\right)[P_{ext}] + \,k_{out,p}[P_{int}] \tag{B.12}$$

$$\frac{d[Ab_{free}]}{dt} = -k_{on}\frac{[Ab_{free}]}{\varepsilon}.\left[T_{free}\right] + \,k_{off}[B_{Ab}] \tag{B.13}$$

$$\frac{d[B_{Ab}]}{dt} = k_{on}\frac{[Ab_{free}]}{\varepsilon}.\left[T_{free}\right] - \,k_{off}[B_{Ab}] - k_e[B_{Ab}] \tag{B.14}$$

Equations for cell killing:

$$P_{kill} = \frac{P_{max}\,[P_b]}{K_m + [P_b]} \tag{B.15}$$

Table B.1: Drug Dynamics Variables

Variables	Unit	Description
ADC	nM	Free ADC
T_{free}	nM	Free Target
B_{ADC}	nM	ADC bound to Target
$B_{ADC,lys}$	nM	Bound ADC in the lysosome
P_{lys}	nM	Payload in the lysosome
P_{int}	nM	Payload not bound to intracellular target
P_b	nM	Payload bound to intracellular target
P_{ext}	nM	Payload free extracellular
Ab_{free}	nM	Free bare antibody
B_{Ab}	nM	Bare antibody bound to Target
P_{kill}	-	Probability of cell killing per agent time step

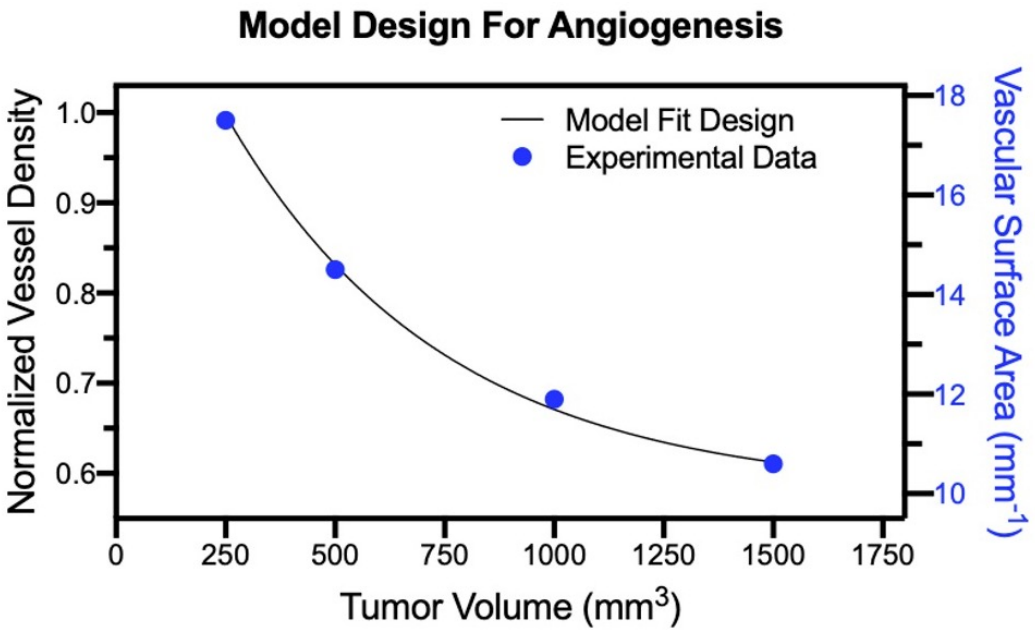

Figure B.2 Model fit to experimental blood vessel density
Assuming the blood vessel density decays with increase in the tumor volume, we approximated the experimental data to an exponential decay function. From the published experimental data, we considered the tumor volumes from 250 mm^3 to 1500 mm^3 and their respective decay in vascular density. The new fraction of active blood vessel is then a function of the simulated tumor volume. As the tumor volume increases, the vascular density decreases following the rate shown in here. At each agent time, if the new fraction of active blood vessel is lower than the vessel density after the decay is calculated, random blood vessel becomes functional in the simulation.

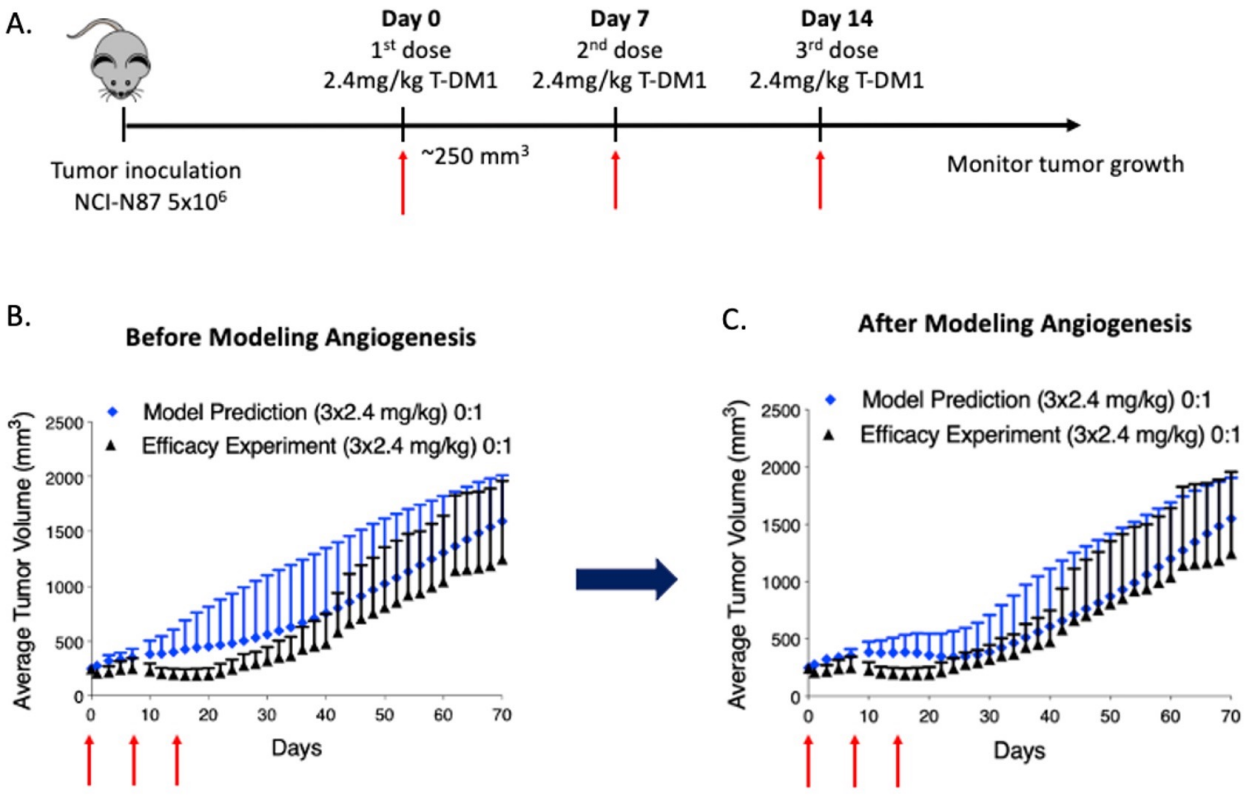

Figure B.3 Fractionated Dosing with or without Angiogenesis and Comparison with Experimental Data.
(A) 5 x 10^6 NCI-N87 cells were inoculated in the rear flank of nude mice. When the tumor reached approximated 250 mm^3, 3 doses of 2.4 mg/kg T-DM1 were given at days 0, 7, and 14. The tumor volume was measured every other day until 70 days or until it reached 2000 mm^3. (B-C) Simulations with the same doses and frequencies were performed before and after the addition of angiogenesis into the model. The inclusion of angiogenesis into the model better predicted the tumor efficacy and tumor uptake (data not shown).

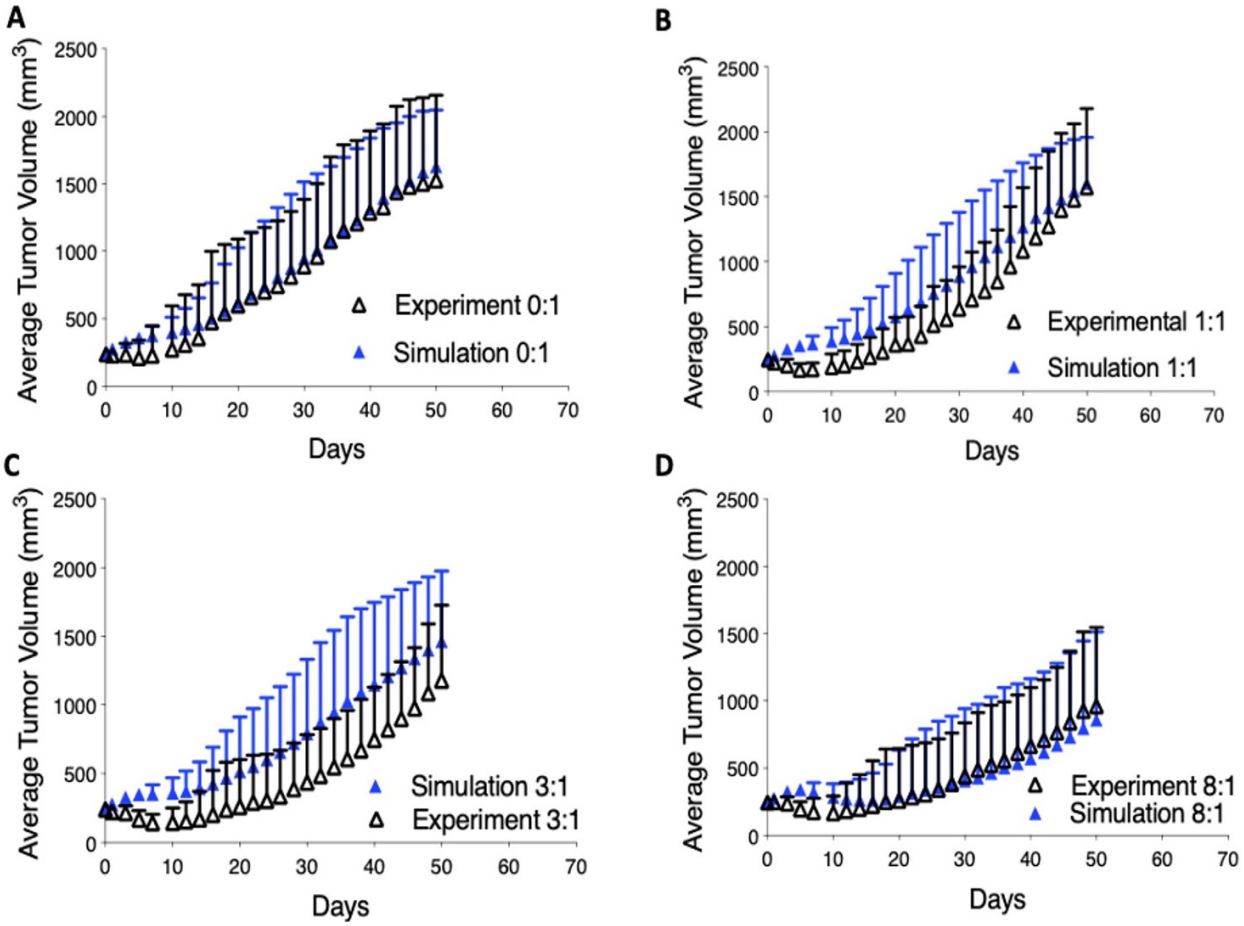

Figure B.4: Recalibration of T-DM1. (A) T-DM1 was recalibrated based on the concentration payload bound instead of the total concentration of the payload inside of the cell and to experimental data in Cilliers, C. *et al*.[31] (B-D) Model was rerun to match with 1:1, 3:1, and 8:1.

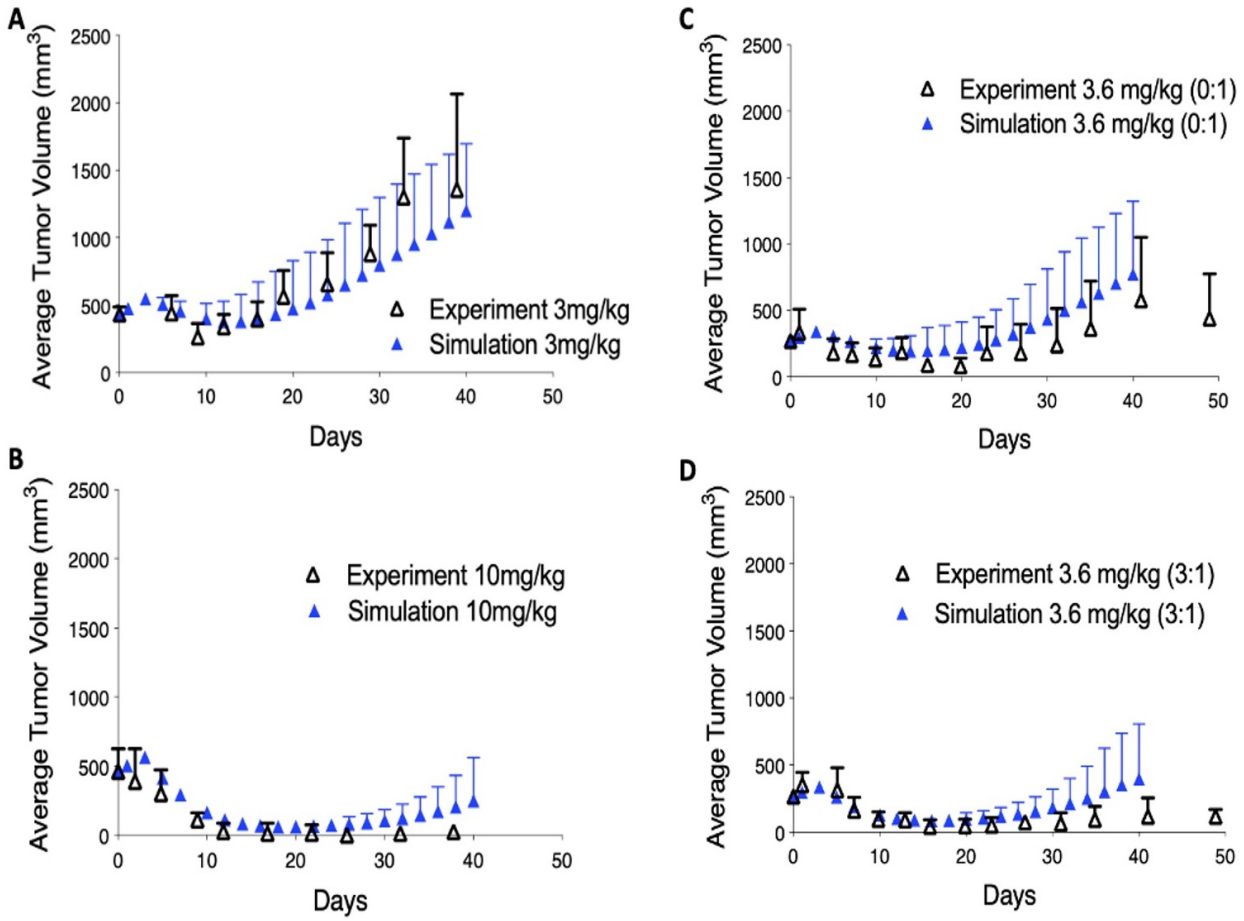

Figure B.5: Calibration of T-MMAE. (A) Model was calibrated to T-MMAE *in vivo* data from Singh, A. et all.[143] (B-D) model was run with dose of 10mg/kg, 3.6mg/kg 0:1, and 3.6 mg/kg 3:1[144] for model validation.

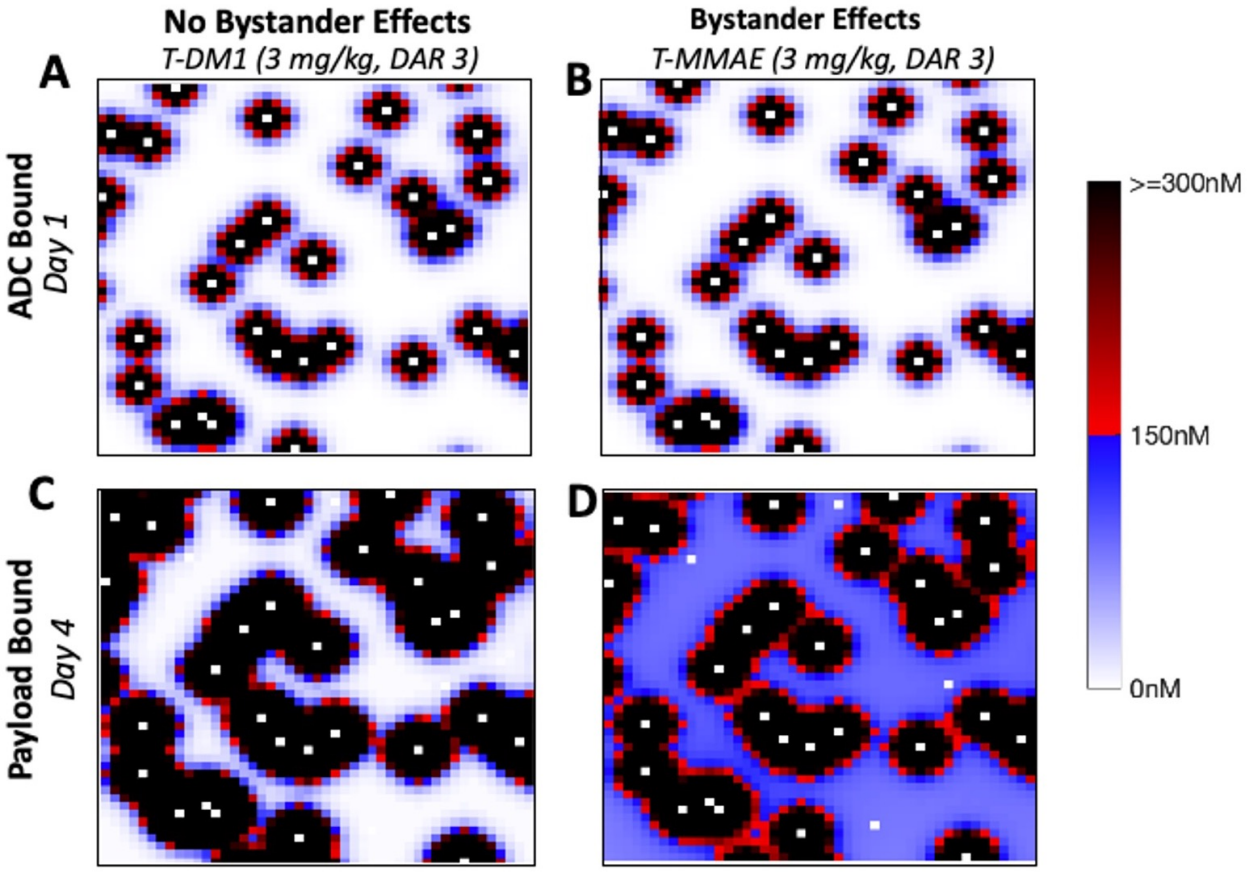

Figure B.6: Distribution of T-DM1 and T-MMAE and their respective payloads at maximum uptake for same dose and DAR (3 mg/kg and DAR 3). (A-B) Distribution of ADCs, T-DM1 and T-MMAE on the surface of the cells. (C-D) Distribution of payload bound for DM1 and MMAE.

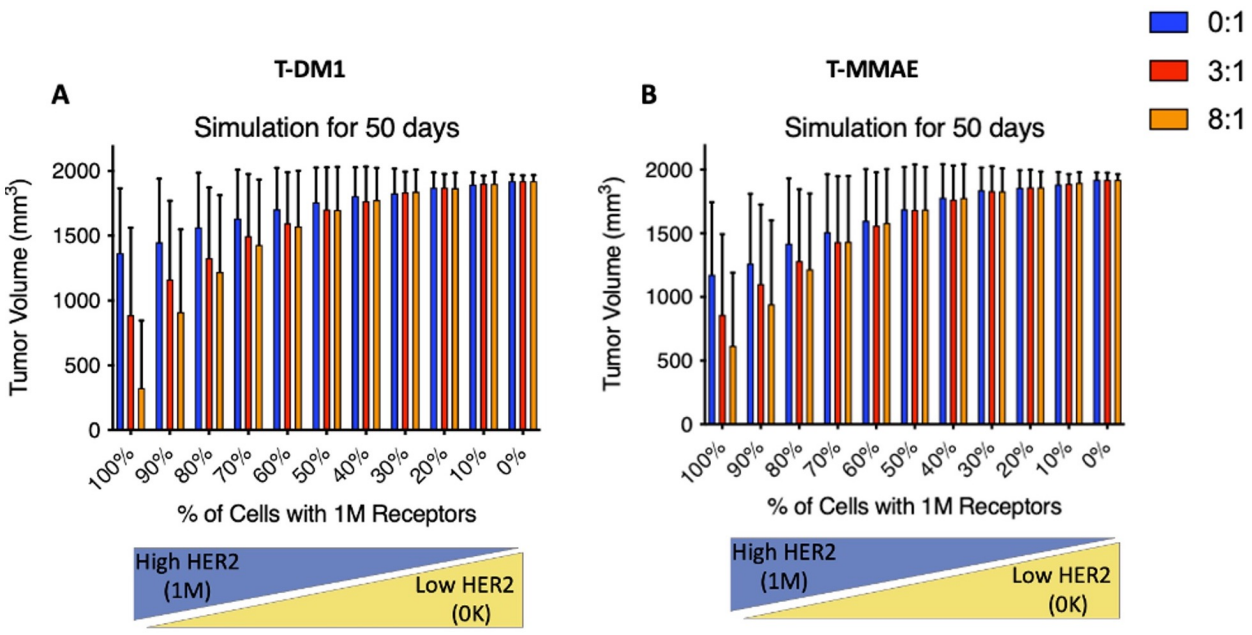

Figure B.7: Tumor efficacy at 50 days for tumors with different receptor expression (1M and 0) (A) T-DM1 regimens (3.6mg/kg and DAR 3.5) B) T-MMAE regimens (1.8 mg/kg and DAR 4).

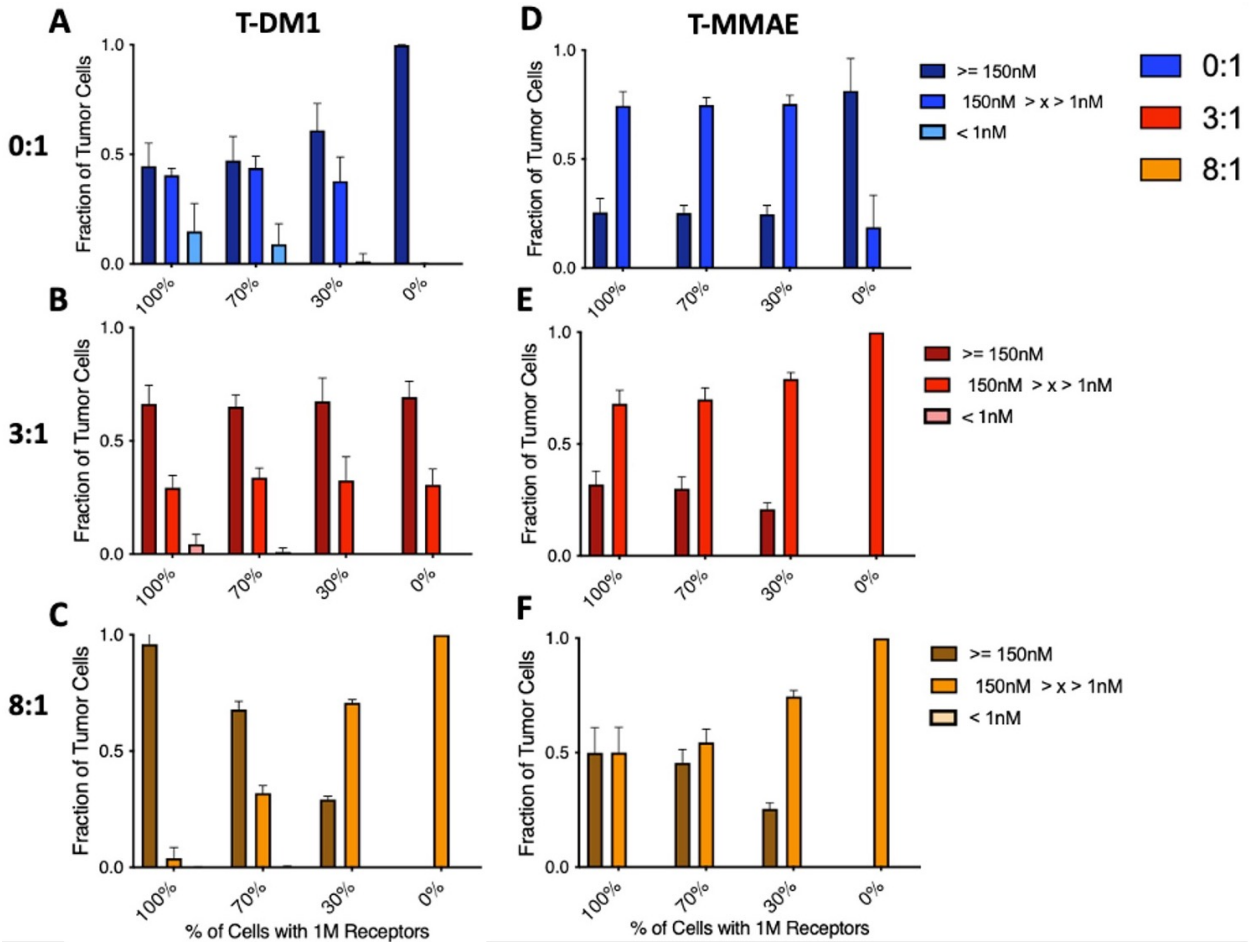

Figure B.8 Percentage of tumor cells with concentration of payload bound. Percentage of tumor cells with concentrations greater or equal to 150nM, in between 150nM and 1nM, and lower than 1nM with coadministration of T-DM1 and T-MMAE with trastuzumab. (A-C) Uptake of DM1 for coadministration of T-DM1 and trastuzumab for tumors with 100%, 70%, 30%, and 0% of cells with 1million receptors per cell vs 50 thousand receptors per cell. (D-F) Uptake of MMAE for coadministration of T-MMAE and trastuzumab for tumors with 100%, 70%, 30%, and 0% of cells with 1 million receptors per cell vs 50 thousand receptors per cell.

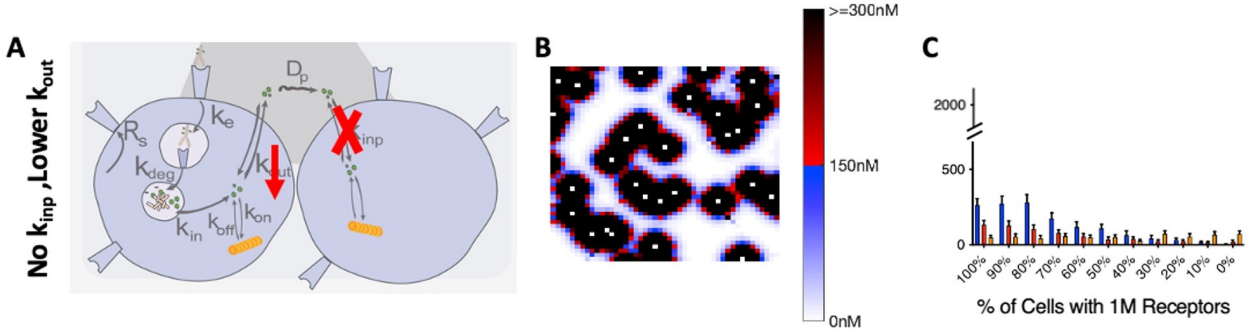

Figure B.9: Distribution and efficacy of regimens with k_{inp}=0 and k_{out}= 6.87x10^{-5}. (A) Schematic of the simulation. B) Distribution of MMAE bound into microtubes. C) Efficacy of regimens with coadministration of trastuzumab and T-MMAE for tumors changing receptor expression.

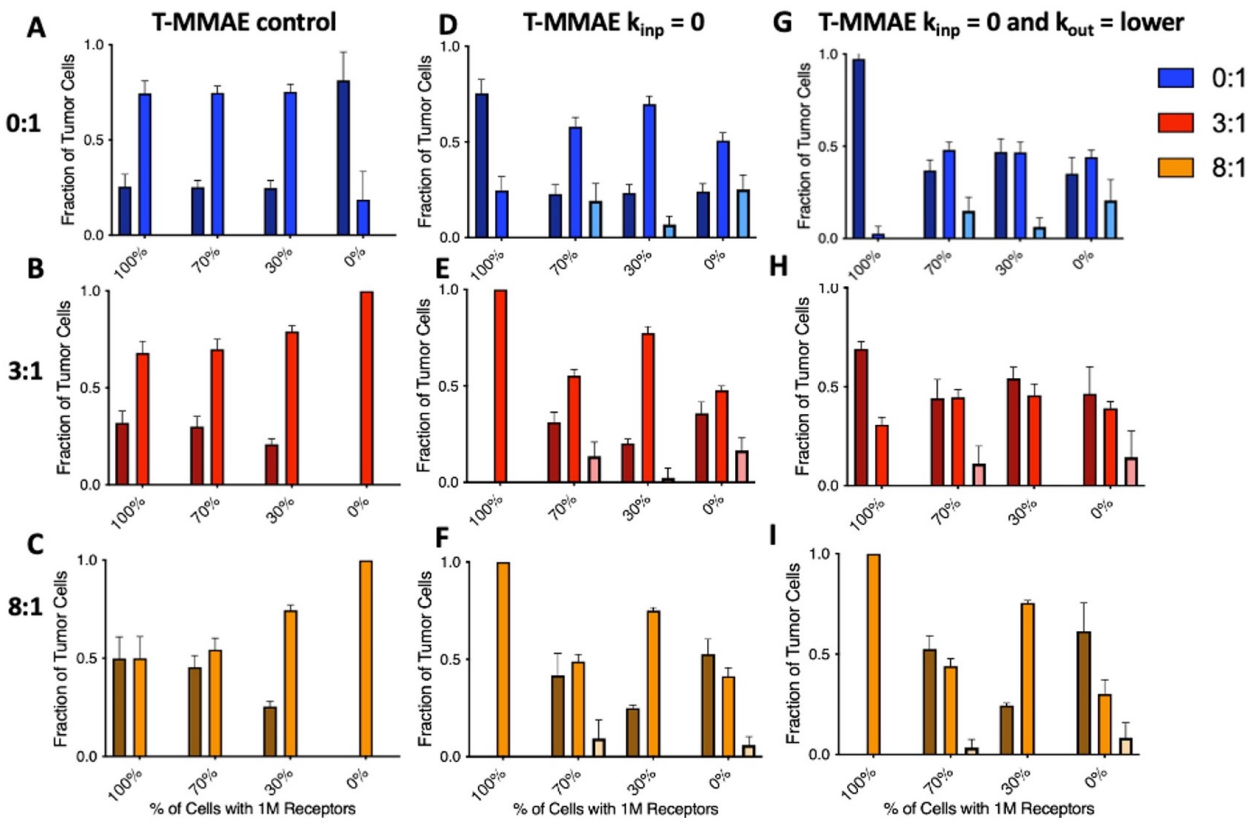

Figure B.10: Percentage of tumor cells with concentration of payload bound with different bystander. Percentage of tumor cells with payload uptake with concentrations greater or equal to 150nM, in between 150nM and 1nM, and lower than 1nM with coadministration of T-DM1 and T-MMAE with trastuzumab. (A-C) Uptake of MMAE for coadministration of T-MMAE and trastuzumab for tumors with 100%, 70%, 30%, and 0% of cells with 1million receptors per cell vs 50 thousand receptors per cell. (D-F) Same regimens but eliminating bystander to adjacent cells by eliminating internalization rate constant (K_{inp}=0). (G-I) In addition to the elimination of bystander to adjacent cells (K_{inp}=0), the scape of the payload rate constant was lowered by one-fold.

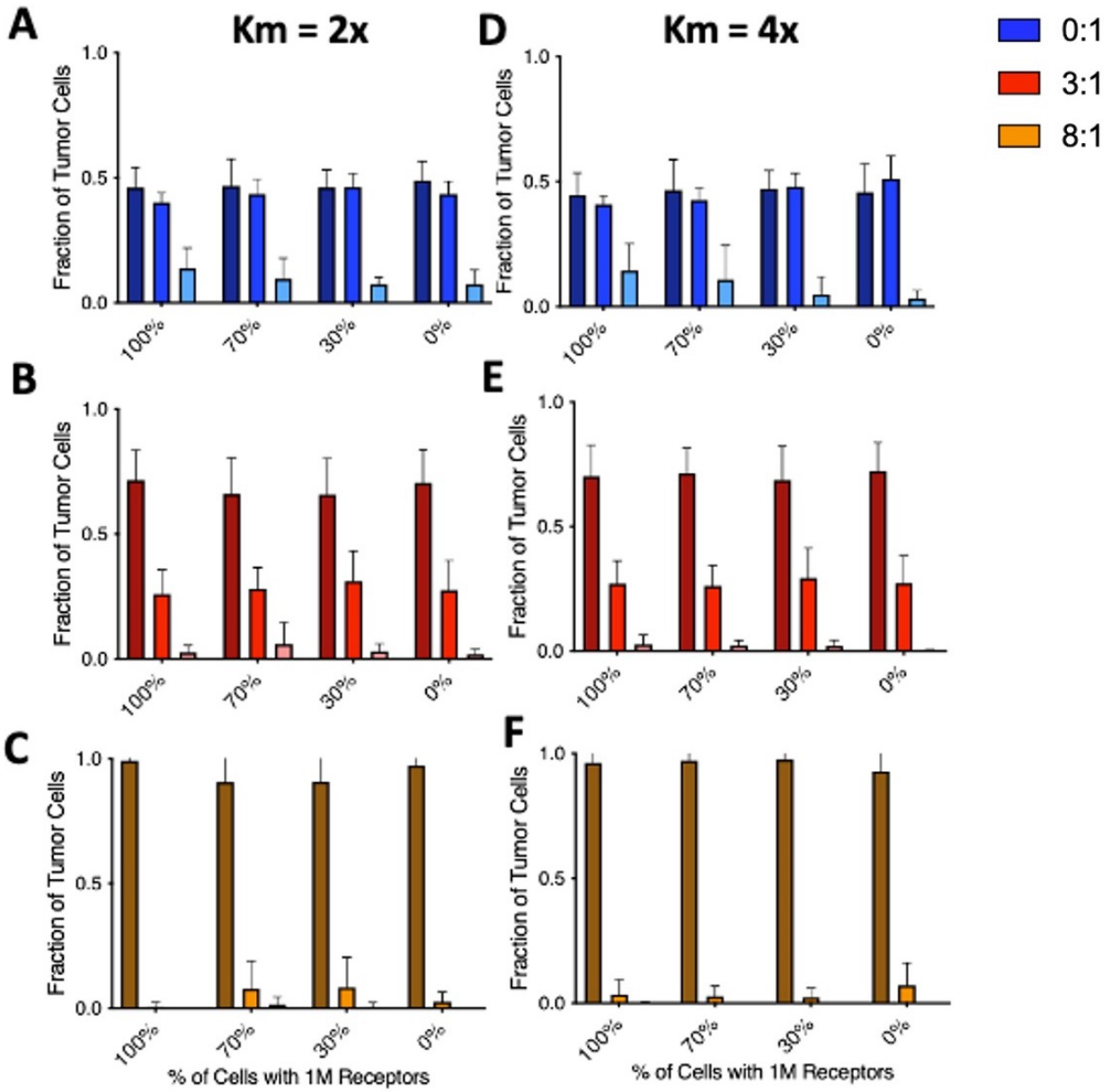

Figure B.11 Percentage of tumor cell with concentration of payload bound with different intrinsic resistant. Percentage of tumors cells with payload uptake with concentrations greater or equal to 150nM, in between 150nM and 1nM, and lower than 1nM with coadministration of T-DM1 and T-MMAE with trastuzumab**.** (A-C) Uptake of DM1 for coadministration of T-DM1 and trastuzumab for tumors with 100%, 70%, 30%, and 0% of cells with intrinsic resistance does not change.

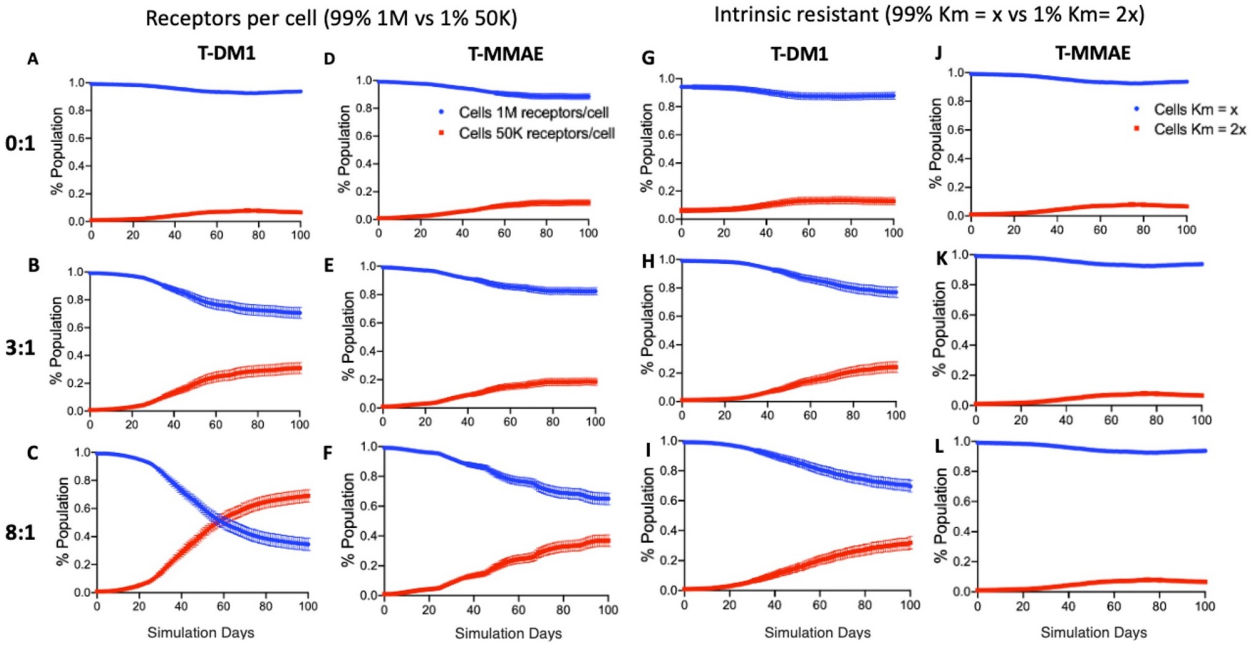

Figure B.12 Percentage of sensitive and resistant cells in tumor composition.
(A-F) Regimens changing tumor composition with 99% of cancer cells with 1M receptors per cell and 1% of cells with 50,000 receptors per cell. Regimens with T-DM1 (A-C) and T-MMAE (D-F) at 0:1, 3:1, and 8:1 coadministrations. (G-L) Regimens changing tumor composition with 99% of cancer cells with no resistance (km=x) and 1% of cells with resistance (km=2x). These were treated with T-DM1 (G-H) and T-MMAE (J-L) at 0:1, 3:1, and 8:1 coadministrations.

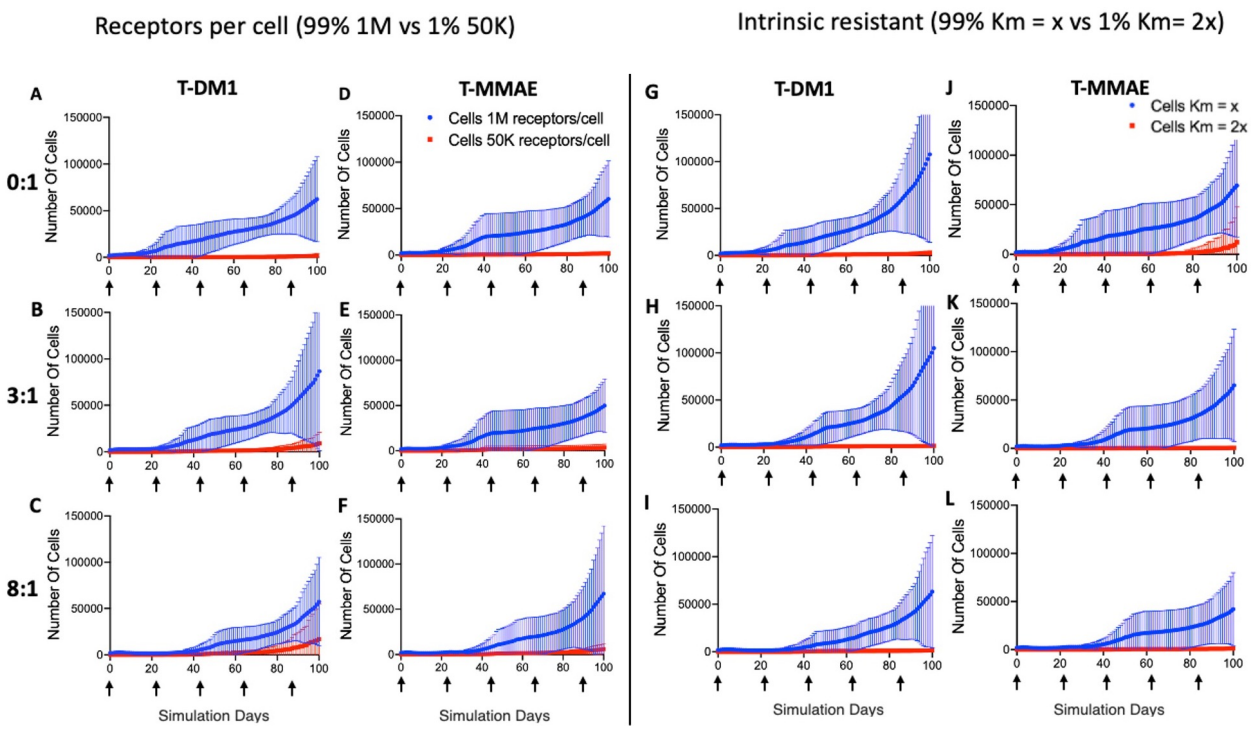

Figure B.13 Tumor cell growth with initial composition of 1% more resistant cells versus 99% sensitive cells for different regimens with T-DM1 or T-MMAE.
(A-F) Coadministration of trastuzumab 0:1, 3:1, 8:1 with T-DM1 (A-C) and T-MMAE (D-F) regimens with 1% of cells with 50K receptors per cell vs 99% of 1M receptors per cell. (G-L) Coadministration of trastuzumab 0:1, 3:1, 8:1 with (T-DM1 (A-C) and T-MMAE (D-F) regimens with 1% of cells with higher intrinsic resistance (Km=2x) vs 99% of cell with Km=x. Km=800nM for T-DM1 and Km=600nM for T-MMAE. All simulations were n=10, and SE is plotted.

Appendix C Supporting Information for Chapter 4

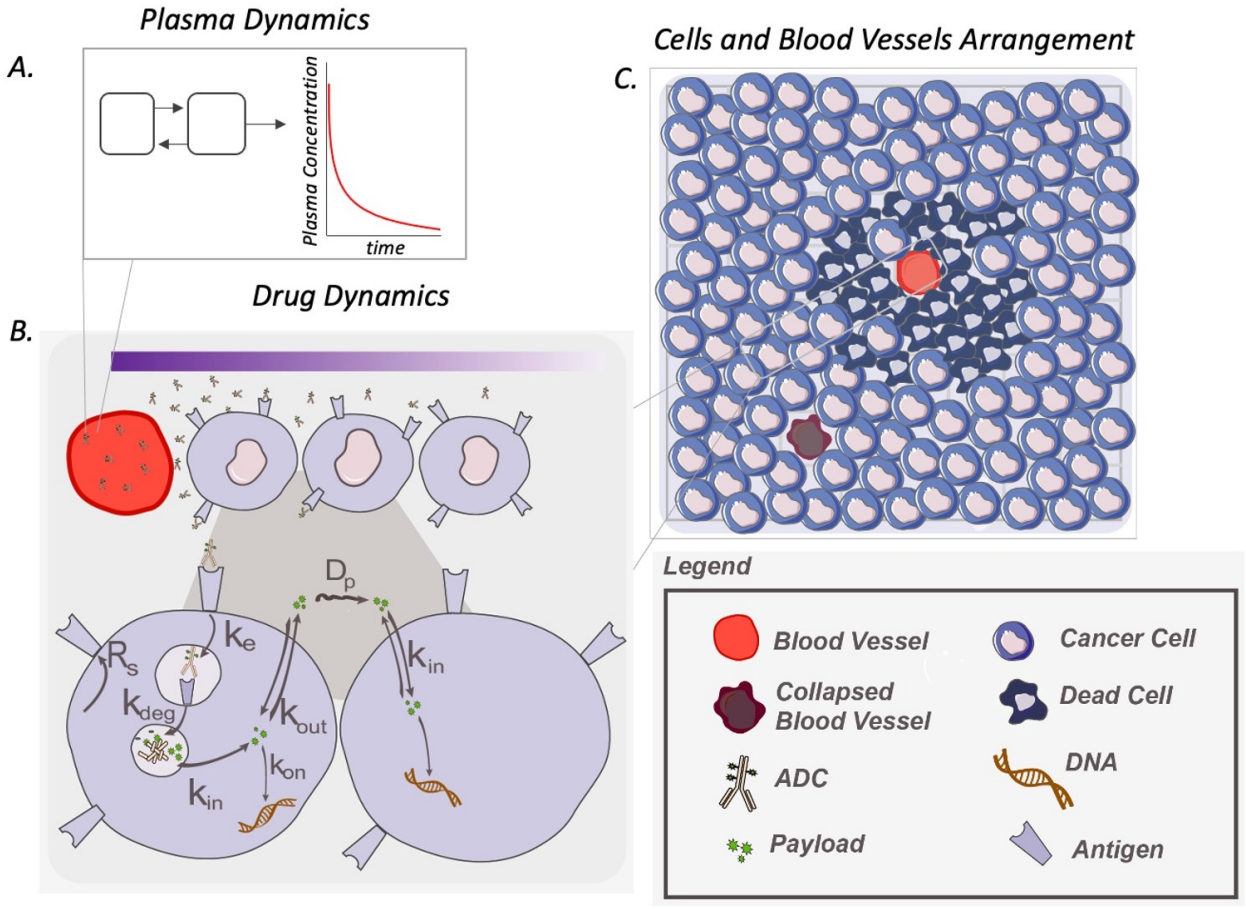

Figure C.1 Model Schematic. A) Plasma Dynamics for TAK-164 and 5F9. B) Drug Dynamics unreversible reaction of the payload DNG-549 and DNA. C) Cells and blood vessels act as agents to capture the 11C dynamics and efficacy.

Plasma clearance:

$$\frac{\mathrm{d[ADC]}}{\mathrm{dt}} = -k_{10}\,.\mathrm{ADC} - k_{12}\,.\mathrm{ADC} + k_{21}.\mathrm{ADC_{p2}} \tag{C.1}$$

$$\frac{\mathrm{d[ADC]}}{\mathrm{dt}} = -k_{21}.\mathrm{ADC_{p2}} + k_{12}\,.\mathrm{ADC} \tag{C.2}$$

Newman boundary condition around the blood vessels:

$$-\mathrm{D_{eff}}\frac{\mathrm{d[ADC]}}{\mathrm{dx}} = \mathrm{P(ADC_{plasma}} - \frac{ADC_{tumor}}{\varepsilon}) \quad \text{(C.3)}$$

Diffusion in 2D Cartesian coordinates:

$$\frac{\partial C}{\partial t} = D(\frac{\partial^2 C}{\partial x^2} + \frac{\partial^2 C}{\partial y^2}) \quad \text{(C.4)}$$

Equations for drug dynamics:

$$\frac{d[ADC]}{dt} = -\,k_{on}\frac{[ADC]}{\varepsilon}.\left[T_{free}\right] + \,k_{off}B_{ADC} \quad \text{(C.5)}$$

$$\frac{d[T_{free}]}{dt} = R_s - \,k_{on}\frac{[ADC]}{\varepsilon}.\left[T_{free}\right] + \,k_{off}[B_{ADC}] - \,k_{on}\frac{\left[Ab_{free}\right]}{\varepsilon}.\left[T_{free}\right] + \,k_{off}[B_{Ab}] - \,k_e[T_{free}] \quad \text{(C.6)}$$

$$\frac{d[B_{ADC}]}{dt} = k_{on}\frac{[ADC]}{\varepsilon}.\left[T_{free}\right] - \,k_{off}[B_{ADC}] - k_e[B_{ADC}] \quad \text{(C.7)}$$

$$\frac{d[B_{ADC,lys}]}{dt} = k_e[B_{ADC}] - \,k_{deg}\left[B_{ADC,lys}\right] \quad \text{(C.8)}$$

$$\frac{d[P_{lys}]}{dt} = \,k_{deg}\left[B_{ADC,lys}\right]DAR - \,k_{in}\left[P_{lys}\right] \quad \text{(C.9)}$$

$$\frac{d[P_{int}]}{dt} = \,k_{in}\left[P_{lys}\right] + \,k_{in,p}\left(\frac{1-\varepsilon_p}{\varepsilon_p}\right)[P_{ext}] - \,k_{out,p}[P_{int}] - \frac{k_{on,p}}{(1-\varepsilon_p)(1+R)}\left(P_{target} - \,P_b\right)[P_{int}] \quad \text{(C.10)}$$

$$\frac{d[P_b]}{dt} = \,\frac{k_{on,p}}{(1-\varepsilon_p)(1+R)}\left(P_{target} - \,P_b\right)[P_{int}] \quad \text{(C.11)}$$

$$\frac{d[P_{ext}]}{dt} = \,-\,k_{in,p}\left(\frac{1-\varepsilon_p}{\varepsilon_p}\right)[P_{ext}] + \,k_{out,p}[P_{int}] \quad \text{(C.12)}$$

$$\frac{d[Ab_{free}]}{dt} = -k_{on}\frac{\left[Ab_{free}\right]}{\varepsilon}.\left[T_{free}\right] + \,k_{off}[B_{Ab}] \quad \text{(C.13)}$$

$$\frac{d[B_{Ab}]}{dt} = k_{on}\frac{\left[Ab_{free}\right]}{\varepsilon}.\left[T_{free}\right] - \,k_{off}[B_{Ab}] - k_e[B_{Ab}] \quad \text{(C.14)}$$

Equations for cell killing:

$$P_{kill} = \frac{P_{max}\,[P_b]}{K_m + [P_b]} \quad \text{(C.15)}$$

Table C.1: Drug Dynamics Variables

Variables	Unit	Description
ADC	nM	Free ADC
T_{free}	nM	Free Target
B_{ADC}	nM	ADC bound to Target
$B_{ADC,lys}$	nM	Bound ADC in the lysosome
P_{lys}	nM	Payload in the lysosome
P_{int}	nM	Payload not bound to intracellular target
P_b	nM	Payload bound to intracellular target
P_{ext}	nM	Payload free extracellular
Ab_{free}	nM	Free bare antibody
B_{Ab}	nM	Bare antibody bound to Target
P_{kill}	-	Probability of cell killing per agent time step
P_{max}	-	Maximum probability of cell killing
K_m	nM	Michaelis-Menten coefficient

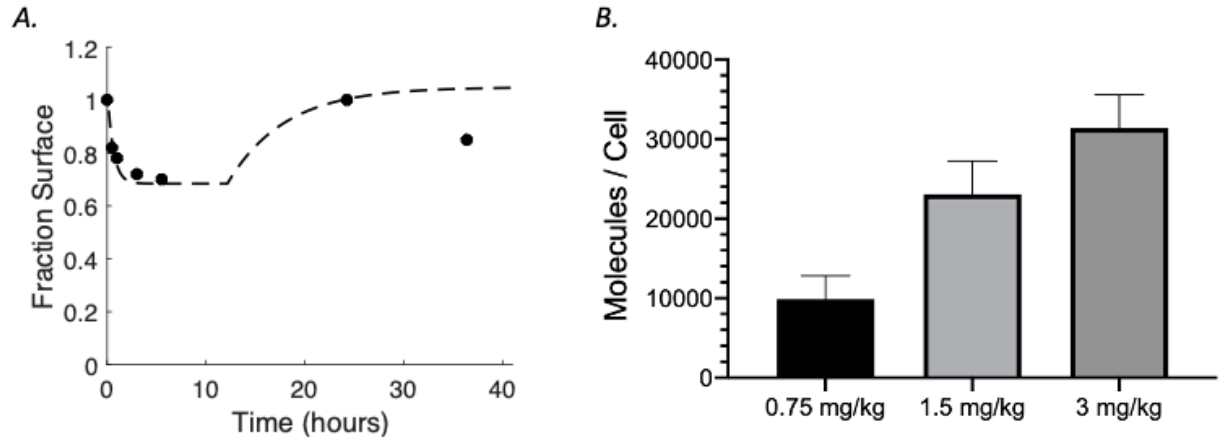

Figure C.2 Calibration to experimental data. A) In vitro internalization rate with 2 phases was calibrated to the ABM. (B) In vivo ADC uptake was approximated to experimental data to estimate average receptor expression, time change between phases, and fraction bound (fb).

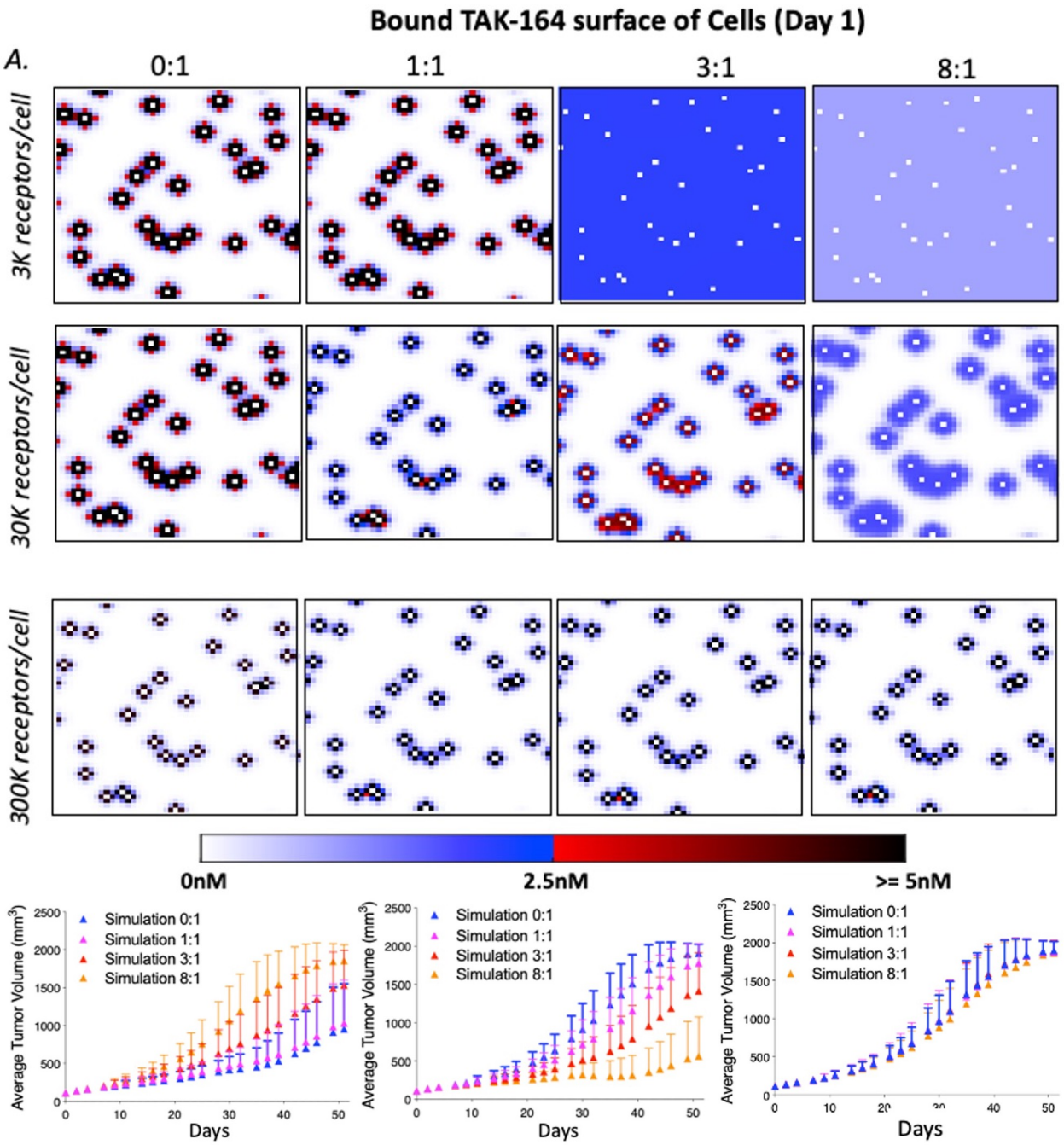

Figure C.3 Prediction of distribution and efficacy in tumors varying receptor expression.
(A) Distribution of bound TAK-164 on the GCC receptors of the cancer cells at day 1 (B) Tumor volume curves for different coadministrations.

Bibliography

1. in World Health Organization (2018).

2. Ahmed, S., Ellis, M., Li, H., Pallucchini, L. & Stein, A.M. Guiding dose selection of monoclonal antibodies using a new parameter (AFTIR) for characterizing ligand binding systems. *J Pharmacokinet Pharmacodyn* **46**, 287-304 (2019).

3. Khongorzul, P., Ling, C.J., Khan, F.U., Ihsan, A.U. & Zhang, J. Antibody-Drug Conjugates: A Comprehensive Review. *Mol Cancer Res* **18**, 3-19 (2020).

4. Birrer, M.J., Moore, K.N., Betella, I. & Bates, R.C. Antibody-Drug Conjugate-Based Therapeutics: State of the Science. *J Natl Cancer Inst* **111**, 538-549 (2019).

5. Schaaf, M.B., Garg, A.D. & Agostinis, P. Defining the role of the tumor vasculature in antitumor immunity and immunotherapy. *Cell Death Dis* **9**, 115 (2018).

6. Thurber, G.M. & Weissleder, R. A systems approach for tumor pharmacokinetics. *PLoS One* **6**, e24696 (2011).

7. Thurber, G.M., Zajic, S.C. & Wittrup, K.D. Theoretic criteria for antibody penetration into solid tumors and micrometastases. *J Nucl Med* **48**, 995-999 (2007).

8. Khera, E. & Thurber, G.M. Pharmacokinetic and Immunological Considerations for Expanding the Therapeutic Window of Next-Generation Antibody-Drug Conjugates. *BioDrugs* **32**, 465-480 (2018).

9. Erickson, H.K. et al. The effect of different linkers on target cell catabolism and pharmacokinetics/pharmacodynamics of trastuzumab maytansinoid conjugates. *Mol Cancer Ther* **11**, 1133-1142 (2012).

10. Lambert, J.M. & Berkenblit, A. Antibody-Drug Conjugates for Cancer Treatment. *The Annual Review of Medicine* **69**, 191-207 (2018).

11. Thurber, G.M., Schmidt, M.M. & Wittrup, K.D. Factors determining antibody distribution in tumors. *Trends Pharmacol Sci* **29**, 57-61 (2008).

12. Thurber, G.M., Schmidt, M.M. & Wittrup, K.D. Antibody tumor penetration: transport opposed by systemic and antigen-mediated clearance. *Adv Drug Deliv Rev* **60**, 1421-1434 (2008).

13. Bostrom, J., Haber, L., Koenig, P., Kelley, R.F. & Fuh, G. High affinity antigen recognition of the dual specific variants of herceptin is entropy-driven in spite of structural plasticity. *PLoS One* **6**, e17887 (2011).

14. Cilliers, C., Guo, H., Liao, J., Christodolu, N. & Thurber, G.M. Multiscale modeling of antibody-drug conjugates: connecting tissue and cellular distribution to whole animal pharmacokinetics and potential implications for efficacy. *AAPS J* **18**, 1117-1130 (2016).

15. Bhatnagar, S., Deschenes, E., Liao, J., Cilliers, C. & Thurber, G.M. Multichannel imaging to quantify four classes of pharmacokinetic distribution in tumors. *J Pharm Sci* **103**, 3276-3286 (2014).

16. Rhoden, J.J. & Wittrup, K.D. Dose dependence of intratumoral perivascular distribution of monoclonal antibodies. *J Pharm Sci* **101**, 860-867 (2012).

17. Nugent, L.J. & Jain, R.K. Extravascular Diffusion in Normal and Neoplastic Tissues. *Cancer Res* **44**, 238-244 (1984).

18. Massa, S. et al. Site-specific labeling of cysteine-tagged camelid single-domain antibody-fragments for use in molecular imaging. *Bioconjug Chem* **25**, 979-988 (2014).

19. Joubert, N., Beck, A., Dumontet, C. & Denevault-Sabourin, C. Antibody-Drug Conjugates: The Last Decade. *Pharmaceuticals (Basel)* **13** (2020).

20. Beck, A., Wurch, T., Bailly, C. & Corvaia, N. Strategies and challenges for the next generation of therapeutic antibodies. *Nat Rev Immunol* **10**, 345-352 (2010).

21. Nessler, I. et al. Increased Tumor Penetration of Single-Domain Antibody-Drug Conjugates Improves In Vivo Efficacy in Prostate Cancer Models. *Cancer Res* **80**, 1268-1278 (2020).

22. Bender, B. et al. A mechanistic pharmacokinetic model elucidating the disposition of trastuzumab emtansine (T-DM1), an antibody-drug conjugate (ADC) for treatment of metastatic breast cancer. *AAPS J* **16**, 994-1008 (2014).

23. Akinleye, A. & Rasool, Z. Immune checkpoint inhibitors of PD-L1 as cancer therapeutics. *J Hematol Oncol* **12**, 92 (2019).

24. Nejadmoghaddam, M. et al. Antibody-drug conjugates: possibilities and challenges. *Avicenna Journal of Medical Biotechnology* **11**, 3-23 (2017).

25. Chari, R. Target cancer therapy conferring specificity to cytotoxic drugs. *Accounts of Chemical Research* **41**, 98-107 (2007).

26. Surova, O. & Zhivotovsky, B. Various modes of cell death induced by DNA damage. *Oncogene* **32**, 3789-3797 (2013).

27. Yaghoubi, S. et al. Potential drugs used in the antibody-drug conjugate (ADC) architecture for cancer therapy. *J Cell Physiol* **235**, 31-64 (2020).

28. Zhao, P. et al. Recent advances of antibody drug conjugates for clinical applications. *Acta Pharm Sin B* **10**, 1589-1600 (2020).

29. Rios-Doria, J. et al. Antibody-drug conjugates bearing pyrrolobenzodiazepine or tubulysin payloads are immunomodulatory and synergize with multiple immunotherapies. *Cancer Res* **77**, 2686-2698 (2017).

30. Khera, E., Cilliers, C., Bhatnagar, S. & Thurber, G.M. Computational transport analysis of antibody-drug conjugate bystander effects and payload tumoral distribution: implications for therapy. *Molecular Systems Design & Engineering* **3**, 73-88 (2018).

31. Cilliers, C., Menezes, B., Nessler, I., Linderman, J. & Thurber, G.M. Improved tumor penetration and single-cell targeting of antibody–drug conjugates increases anticancer efficacy and host survival. *Cancer Research* **78**, 758-768 (2018).

32. Ocean, A.J. et al. Sacituzumab govitecan (IMMU-132), an anti-Trop-2-SN-38 antibody-drug conjugate for the treatment of diverse epithelial cancers: Safety and pharmacokinetics. *Cancer* **123**, 3843-3854 (2017).

33. Garcia-Alonso, S., Ocana, A. & Pandiella, A. Trastuzumab Emtansine: Mechanisms of Action and Resistance, Clinical Progress, and Beyond. *Trends Cancer* **6**, 130-146 (2020).

34. Chen, R. et al. CD30 Downregulation, MMAE Resistance, and MDR1 Upregulation Are All Associated with Resistance to Brentuximab Vedotin. *Mol Cancer Ther* **14**, 1376-1384 (2015).

35. Seol, H. et al. Intratumoral heterogeneity of HER2 gene amplification in breast cancer: its clinicopathological significance. *Mod Pathol* **25**, 938-948 (2012).

36. Ocana, A., Amir, E. & Pandiella, A. HER2 heterogeneity and resistance to anti-HER2 antibody-drug conjugates. *Breast Cancer Res* **22**, 15 (2020).

37. Yardley, D.A. et al. Quantitative measurement of HER2 expression in breast cancers: comparison with 'real-world' routine HER2 testing in a multicenter Collaborative Biomarker Study and correlation with overall survival. *Breast Cancer Res* **17**, 41 (2015).

38. Marchio, C. et al. Evolving concepts in HER2 evaluation in breast cancer: Heterogeneity, HER2-low carcinomas and beyond. *Semin Cancer Biol* (2020).

39. Whiteside, T.L. The tumor microenvironment and its role in promoting tumor growth. *Oncogene* **27**, 5904-5912 (2008).

40. Thakkar, S., Sharma, D., Kalia, K. & Tekade, R.K. Tumor microenvironment targeted nanotherapeutics for cancer therapy and diagnosis: A review. *Acta Biomater* **101**, 43-68 (2020).

41. Hinshaw, D.C. & Shevde, L.A. The Tumor Microenvironment Innately Modulates Cancer Progression. *Cancer Res* **79**, 4557-4566 (2019).

42. Baxter, L.T. & Jain, R.K. Transport of Fluid and Macromolecules in Tumors I Role of interstitial pressue and convection. *Microvascular Research* **37**, 77-104 (1988).

43. Jain, R.K. Transport of Molecules, Particles, and Cells in Solid Tumors. *Annual Reviews Biomed. Eng.* **01**, 241-263 (1999).

44. Jain, R.K. Normalization of Tumor Vasculatur- An Emerging concept in Antiangiogenic Therapy. *Science* **307** (2005).

45. Ronca, R., Benkheil, M., Mitola, S., Struyf, S. & Liekens, S. Tumor angiogenesis revisited: Regulators and clinical implications. *Med Res Rev* **37**, 1231-1274 (2017).

46. Balkwill, F.R., Capasso, M. & Hagemann, T. The tumor microenvironment at a glance. *J Cell Sci* **125**, 5591-5596 (2012).

47. Thorsson, V. et al. The Immune Landscape of Cancer. *Immunity* **48**, 812-830 e814 (2018).

48. Zuazo-Gaztelu, I. & Casanovas, O. Unraveling the Role of Angiogenesis in Cancer Ecosystems. *Front Oncol* **8**, 248 (2018).

49. Barbolosi, D., Ciccolini, J., Lacarelle, B., Barlesi, F. & Andre, N. Computational oncology mathematical modelling of drug regimens for precision medicine. *Nature reviews* **13**, 242-254 (2016).

50. Karolak, A. & Rejniak, K.A. Micropharmacology: An In Silico Approach for Assessing Drug Efficacy Within a Tumor Tissue. *Bull Math Biol* **81**, 3623-3641 (2019).

51. Williams, D.P. et al. Novel in vitro and mathematical models for the prediction of chemical toxicity. *Toxicol Res (Camb)* **2**, 40-59 (2013).

52. Roose, T., Chapman, S.J. & Maini, P.K. Mathematical Models of Avascular Tumor Growth. *SIAM Review* **49**, 179-208 (2007).

53. Norton, L. A gompertzian model of human breast cancer growth. *Cancer Research* **48**, 7067-7071 (1988).

54. Freyer, J. Regulation of growth saturation and development of necroses in emt6 Ro multicellular spheroids by the glucose and oxygen supply. *1986* **46**, 3504-3512 (1986).

55. Unni, P. & Seshaiyer, P. Mathematical Modeling, Analysis, and Simulation of Tumor Dynamics with Drug Interventions. *Comput Math Methods Med* **2019**, 4079298 (2019).

56. Boondirek, A., Triampo, W. & Nuttavut, N. A review of cellular automata models of tumor growth.pdf. *International Mathematical Forum* **61**, 3023-3029 (2010).

57. Rivaz, A., Azizian, M. & Soltani, M. Various Mathematical Models of Tumor Growth with Reference to Cancer Stem Cells: A Review. *Iranian Journal of Science and Technology, Transactions A: Science* **43**, 687-700 (2019).

58. Teicher, B.A. Tumor models for efficacy determination. *Mol Cancer Ther* **5**, 2435-2443 (2006).

59. Vaghi, C. et al. Population modeling of tumor growth curves and the reduced Gompertz model improve prediction of the age of experimental tumors. *PLoS Comput Biol* **16**, e1007178 (2020).

60. Tubiana, M. The growth and progression of human tumors implications for management strategy. *Radiotherapy and Oncology* **6**, 167-184 (1986).

61. Ribba, B. et al. A review of mixed-effects models of tumor growth and effects of anticancer drug treatment used in population analysis. *CPT Pharmacometrics Syst Pharmacol* **3**, e113 (2014).

62. Yankeelov, T.E. et al. Clinically relevant modeling of tumor growth and treatment response. *Sci Transl Med* **5**, 187ps189 (2013).

63. Drexler, D.A., Sápi, J. & Kovács, L. Modeling of Tumor Growth Incorporating the Effects of Necrosis and the Effect of Bevacizumab. *Complexity* **2017**, 1-10 (2017).

64. Antonopoulos, M., Dionysiou, D., Stamatakos, G. & Uzunoglu, N. Three-dimensional tumor growth in time-varying chemical fields: a modeling framework and theoretical study. *BMC Bioinformatics* **20**, 442 (2019).

65. Cornelis, F. et al. In vivo mathematical modeling of tumor growth from imaging data: soon to come in the future? *Diagn Interv Imaging* **94**, 593-600 (2013).

66. Tabassum, S., Rosli, N.B. & Mazalan, M.S. Mathematical modeling of cancer growth process a review. *Journal of physics conference series* **1366** (2019).

67. Peirce, S.M. Computational and mathematical modeling of angiogenesis. *Microcirculation* **15**, 739-751 (2008).

68. Vilanova, G., Colominas, I. & Gomez, H. A mathematical model of tumour angiogenesis: growth, regression and regrowth. *J R Soc Interface* **14** (2017).

69. Pillay, S., Byrne, H.M. & Maini, P.K. Modeling angiogenesis: A discrete to continuum description. *Phys Rev E* **95**, 012410 (2017).

70. Lugano, R., Ramachandran, M. & Dimberg, A. Tumor angiogenesis: causes, consequences, challenges and opportunities. *Cell Mol Life Sci* **77**, 1745-1770 (2020).

71. Qutub, A.A., Mac Gabhann, F., Karagiannis, E.D., Vempati, P. & Popel, A.S. Multiscale models of angiogenesis. *IEEE Eng Med Biol Mag* **28**, 14-31 (2009).

72. Amann, A. et al. Development of a 3D angiogenesis model to study tumour - endothelial cell interactions and the effects of anti-angiogenic drugs. *Sci Rep* **7**, 2963 (2017).

73. Burton, J.K., Bottino, D. & Secomb, T.W. A Systems Pharmacology Model for Drug Delivery to Solid Tumors by Antibody-Drug Conjugates: Implications for Bystander Effects. *AAPS J* **22**, 12 (2019).

74. Bocci, G. et al. ADME-Space: a new tool for medicinal chemists to explore ADME properties. *Sci Rep* **7**, 6359 (2017).

75. Clark, A.M. et al. Open Source Bayesian Models. 1. Application to ADME/Tox and Drug Discovery Datasets. *J Chem Inf Model* **55**, 1231-1245 (2015).

76. Shah, D.K. & Betts, A.M. Towards a platform PBPK model to characterize the plasma and tissue disposition of monoclonal antibodies in preclinical species and human. *J Pharmacokinet Pharmacodyn* **39**, 67-86 (2012).

77. Vassal, G. et al. Prospective validation of a novel IV busulfan fixed dosing for paediatric patients to improve therapeutic AUC targeting without drug monitoring. *Cancer Chemother Pharmacol* **61**, 113-123 (2008).

78. Jin, F. et al. Population pharmacokinetic modeling of idelalisib, a novel PI3Kdelta inhibitor, in healthy subjects and patients with hematologic malignancies. *Cancer Chemother Pharmacol* **77**, 89-98 (2016).

79. Shamsi, M., Mohammadi, A., Manshadi, M.K.D. & Sanati-Nezhad, A. Mathematical and computational modeling of nano-engineered drug delivery systems. *J Control Release* **307**, 150-165 (2019).

80. Shah, D.K. et al. Establishing in vitro-in vivo correlation for antibody drug conjugate efficacy: a PK/PD modeling approach. *J Pharmacokinet Pharmacodyn* **45**, 339-349 (2018).

81. Chen, Y. et al. Physiologically based pharmacokinetic modeling as a tool to predict drug interactions for antibody-drug conjugates. *Clin Pharmacokinet* **54**, 81-93 (2015).

82. Betts, A. & van der Graaf, P.H. Mechanistic Quantitative Pharmacology Strategies for the Early Clinical Development of Bispecific Antibodies in Oncology. *Clin Pharmacol Ther* (2020).

83. Singh, A.P., Shin, Y.G. & Shah, D.K. Application of Pharmacokinetic-Pharmacodynamic Modeling and Simulation for Antibody-Drug Conjugate Development. *Pharm Res* **32**, 3508-3525 (2015).

84. Cicchese, J.M., Dartois, V., Kirschner, D.E. & Linderman, J.J. Both Pharmacokinetic Variability and Granuloma Heterogeneity Impact the Ability of the First-Line Antibiotics to Sterilize Tuberculosis Granulomas. *Front Pharmacol* **11**, 333 (2020).

85. Biagi, M.J., Butler, D.A. & Wenzler, E. AUC-Based Monitoring of Vancomycin: Closing the Therapeutic Window. *J Appl Lab Med* **3**, 743-746 (2019).

86. Singh, A.P. et al. Evolution of Antibody-Drug Conjugate Tumor Disposition Model to Predict Preclinical Tumor Pharmacokinetics of Trastuzumab-Emtansine (T-DM1). *AAPS J* **18**, 861-875 (2016).

87. Welter, M. & Rieger, H. Interstitial fluid flow and drug delivery in vascularized tumors: a computational model. *PLoS One* **8**, e70395 (2013).

88. Goldman, D. Theoretical models of microvascular oxygen transport to tissue. *Microcirculation* **15**, 795-811 (2008).

89. Vasalou, C., Helmlinger, G. & Gomes, B. A mechanistic tumor penetration model to guide antibody drug conjugate design. *PLoS One* **10**, e0118977 (2015).

90. Jacob Leal, S., Napoletano, M., Roventini, A. & Fagiolo, G. Rock around the clock: An agent-based model of low- and high-frequency trading. *Journal of Evolutionary Economics* **26**, 49-76 (2015).

91. Nowak, S.A., Parker, A.M., Radhakrishnan, A., Schoenborn, N. & Pollack, C. Using an Agent-based Model to Examine Deimplementation of Breast Cancer Screening. *Medical Care* **00** (2020).

92. Suwarno, A., van Noordwijk, M., Weikard, H.P. & Suyamto, D. Indonesia's forest conversion moratorium assessed with an agent-based model of Land-Use Change and Ecosystem Services (LUCES). *Mitig Adapt Strateg Glob Chang* **23**, 211-229 (2018).

93. Manzo, G. & Baldassarri, D. Heuristics, Interactions, and Status Hierarchies. *Sociological Methods & Research* **44**, 329-387 (2014).

94. Salle, I., Sénégas, M.-A. & Yıldızoğlu, M. How transparent about its inflation target should a central bank be? *Journal of Evolutionary Economics* **29**, 391-427 (2018).

95. Hoehme, S. et al. Model Prediction and Validation of an Order Mechanism Controlling the Spatiotemporal Phenotype of Early Hepatocellular Carcinoma. *Bull Math Biol* **80**, 1134-1171 (2018).

96. Pourhasanzade, F., Sabzpoushan, S.H., Alizadeh, A.M. & Esmati, E. An agent-based model of avascular tumor growth: Immune response tendency to prevent cancer development. *Simulation* **93**, 641-657 (2017).

97. Norton, K.A., Wallace, T., Pandey, N.B. & Popel, A.S. An agent-based model of triple-negative breast cancer: the interplay between chemokine receptor CCR5 expression, cancer stem cells, and hypoxia. *BMC Syst Biol* **11**, 68 (2017).

98. Zhang, L., Strouthos, C.G., Wang, Z. & Deisboeck, T.S. Simulating Brain Tumor Heterogeneity with a Multiscale Agent-Based Model: Linking Molecular Signatures, Phenotypes and Expansion Rate. *Math Comput Model* **49**, 307-319 (2009).

99. Casarin, S. & Dondossola, E. An agent-based model of prostate Cancer bone metastasis progression and response to Radium223. *BMC Cancer* **20**, 605 (2020).

100. Metzcar, J., Wang, Y., Heiland, R. & Macklin, P. A review of cell-based computational modeling in cancer biology. *Clinical Cancer Informatics* (2018).

101. Ghaffarizadeh, A., Heiland, R., Friedman, S.H., Mumenthaler, S.M. & Macklin, P. PhysiCell: An open source physics-based cell simulator for 3-D multicellular systems. *PLoS Comput Biol* **14**, e1005991 (2018).

102. Anderson, A.R., Rejniak, K.A., Gerlee, P. & Quaranta, V. Microenvironment driven invasion: a multiscale multimodel investigation. *J Math Biol* **58**, 579-624 (2009).

103. Anderson, A.R. Modeling of cancer growth evolution and invasion bridging scales and models. *Math. Model Nat. Phenon.* **2**, 1-29 (2007).

104. Cilfone, N.A., Kirschner, D.E. & Linderman, J.J. Strategies for efficient numerical implementation of hybrid multi-scale agent-based models to describe biological systems. *Cell Mol Bioeng* **8**, 119-136 (2015).

105. Sun, X., Zhang, L., Boa, J., Strouthos, C. & Zhou, X. Multi-scale agent based brain cancer modeling and prediction of TKI treatment response: incorporating EGFR signaling pathway and angiogenesis. *BMC Bioinformatics* **13**, 218 (2012).

106. Coats, S. et al. Antibody-drug conjugates: future directions in clinical and translational strategies to improve the therapeutic Index. *Clinical cancer research : an official journal of the American Association for Cancer Research* (2019).

107. Baker, J.H.E. et al. Heterogeneous distribution of trastuzumab in HER2-positive xenografts and metastases: role of the tumor microenvironment. *Clin Exp Metastasis* **35**, 691-705 (2018).

108. Lu, G. et al. Co-administered antibody improves penetration of antibody-dye conjugate into human cancers with implications for antibody-drug conjugates. *Nat Commun* **11**, 5667 (2020).

109. Hinrichs, M.J.M. et al. Fractionated dosing improves preclinical therapeutic index of pyrrolobenzodiazepine-containing antibody drug conjugates. *Clinical cancer research : an official journal of the American Association for Cancer Research* **23**, 5858-5868 (2017).

110. Jumbe, N.L. et al. Modeling the efficacy of trastuzumab-DM1, an antibody drug conjugate, in mice. *J Pharmacokinet Pharmacodyn* **37**, 221-242 (2010).

111. Maass, K.F., Kulkarni, C., Betts, A.M. & Wittrup, K.D. Determination of cellular processing rates for a trastuzumab-maytansinoid antibody-drug conjugate (ADC) highlights key parameters for ADC design. *AAPS J* **18**, 635-646 (2016).

112. Shah, D.K., Haddish-Berhane, N. & Betts, A. Bench to bedside translation of antibody drug conjugates using a multiscale mechanistic PK/PD model: a case study with brentuximab-vedotin. *J Pharmacokinet Pharmacodyn* **39**, 643-659 (2012).

113. Thurber, G.M. & Dane Wittrup, K. A mechanistic compartmental model for total antibody uptake in tumors. *J Theor Biol* **314**, 57-68 (2012).

114. Singh, A.P. & Shah, D.K. A “dual" cell-level systems PK-PD model to characterize the bystander effect of ADC. *J Pharm Sci* (2019).

115. Cilliers, C., Nessler, I., Christodolu, N. & Thurber, G.M. Tracking Antibody Distribution with Near-Infrared Fluorescent Dyes: Impact of Dye Structure and Degree of Labeling on Plasma Clearance. *Mol Pharm* **14**, 1623-1633 (2017).

116. Nugent, L. & Jain, R.K. Extravascular diffusion in normal and neoplastic tissues. *Cancer Res* **44**, 238-244 (1984).

117. Thurber, G.M. & Weissleder, R. Quantitating antibody uptake in vivo: conditional dependence on antigen expression levels. *Mol Imaging Biol* **13**, 623-632 (2011).

118. Poon, K.A. et al. Preclinical safety profile of trastuzumab emtansine (T-DM1): mechanism of action of its cytotoxic component retained with improved tolerability. *Toxicol Appl Pharmacol* **273**, 298-313 (2013).

119. Schmidt, M.M. & Wittrup, K.D. A modeling analysis of the effects of molecular size and binding affinity on tumor targeting. *Mol Cancer Ther* **8**, 2861-2871 (2009).

120. Yuan, F.D., M. Fukumura, D. Leunig, M. Berk, D. Torchilin, V. Jain, R. K. Vascular permeability in a human tumor xenograft: molecular size dependence and cutoff size. *Cancer Research* **55**, 3752-3756 (1995).

121. Chalkley, H., Cornfiel,J., Park, H. A Method for Estimating Volume-Surface Ratios. *Science* **110**, 295-297 (1949).

122. Forster, J.C., Harriss-Phillips, W.M., Douglass, M.J. & Bezak, E. A review of the development of tumor vasculature and its effects on the tumor microenvironment. *Hypoxia (Auckl)* **5**, 21-32 (2017).

123. Cardillo, T.M. et al. Sacituzumab govitecan (IMMU-132), an anti-trop-2/SN-38 antibody-drug conjugate: characterization and efficacy in pancreatic, gastric, and other cancers. *Bioconjug Chem* **26**, 919-931 (2015).

124. Prabhu, S.B., A. Leipold, D. Khawli, L. Li, D. Lu D. Theil, F. Joshi, A. Lum, B. Antiboy delivery of drugs and radionuclides factors influencing clinical phamacology. *Therapeutic Delivery* **6**, 769-791 (2011).

125. Pienaar, E. et al. Comparing efficacies of moxifloxacin, levofloxacin and gatifloxacin in tuberculosis granulomas using a multi-scale systems pharmacology approach. *PLoS Comput Biol* **13**, e1005650 (2017).

126. Hamblett, K. et al. Effects of drug loading on the antitumor activity of a monoclonal antibody drug conjugate. *Clinical Cancer Research* **10**, 7063-7070 (2004).

127. Sukumaran, S. et al. Mechanism-based pharmacokinetic/pharmacodynamic model for THIOMAB drug conjugates. *Pharm Res* **32**, 1884-1893 (2015).

128. Rosenberg, J.E. et al. Pivotal trial of enfortumab vedotin in urothelial carcinoma after platinum and anti-programmed death 1:programmed death ligand 1 therapy. *Journal of Clinical Oncology*, 1-9 (2019).

129. Wang, J., Seebacher, N., Shi, H., Kan, Q. & Zhenfeng, D. Novel strategies to prevent the development of multidrug resistance (MDR) in cancer. *Oncotarget* **8 (No 48)**, 84559-84571 (2017).

130. Wittrup, K.D. Antitumor antibodies can drive therapeutic T cell responses. *Trends Cancer* **3**, 615-620 (2017).

131. Cilfone, N.A. et al. Computational modeling predicts IL-10 control of lesion sterilization by balancing early host immunity-mediated antimicrobial responses with caseation during mycobacterium tuberculosis infection. *J Immunol* **194**, 664-677 (2015).

132. Bartelink, I.H. et al. Tumor drug penetration measurements could be the neglected piece of the personalized cancer treatment puzzle. *Clin Pharmacol Ther* **106**, 148-163 (2019).

133. Rye, I.H. et al. Intratumor heterogeneity defines treatment-resistant HER2+ breast tumors. *Mol Oncol* **12**, 1838-1855 (2018).

134. Allgayer, H. & Aguirre-Ghiso, J.A. The urokinase receptor (u-PAR)--a link between tumor cell dormancy and minimal residual disease in bone marrow? *APMIS* **116**, 602-614 (2008).

135. Li, J. et al. Dormant Cells: The Original Cause of Tumor Recurrence and Metastasis. *Cell Biochem Biophys* **72**, 317-320 (2015).

136. Manthri, S., Singal, S., Youssef, B. & Chakraborty, K. Long-time Response with Ado-trastuzumab Emtansine in a Recurrent Metastatic Breast Cancer. *Cureus* **11**, e6036 (2019).

137. Bon, G. et al. Loss of HER2 and decreased T-DM1 efficacy in HER2 positive advanced breast cancer treated with dual HER2 blockade: the SePHER Study. *J Exp Clin Cancer Res* **39**, 279 (2020).

138. Rios-Luci, C. et al. Resistance to the Antibody-Drug Conjugate T-DM1 Is Based in a Reduction in Lysosomal Proteolytic Activity. *Cancer Res* **77**, 4639-4651 (2017).

139. Hunter, F.W. et al. Mechanisms of resistance to trastuzumab emtansine (T-DM1) in HER2-positive breast cancer. *Br J Cancer* **122**, 603-612 (2020).

140. Staudacher, A.H. & Brown, M.P. Antibody drug conjugates and bystander killing: is antigen-dependent internalisation required? *Br J Cancer* **117**, 1736-1742 (2017).

141. Menezes, B., Cilliers, C., Wessler, T., Thurber, G.M. & Linderman, J.J. An Agent-Based Systems Pharmacology Model of the Antibody-Drug Conjugate Kadcyla to Predict Efficacy of Different Dosing Regimens. *AAPS J* **22**, 29 (2020).

142. Hilmas, D.E. & Gillette, E.L. Morphometric Analyses of the Microvasculature of Tumors During Growth and After X-irradiation. *Cancer* **33**, 103-110 (1974).

143. Singh, A.P. et al. Evolution of the Systems Pharmacokinetics-Pharmacodynamics Model for Antibody-Drug Conjugates to Characterize Tumor Heterogeneity and In Vivo Bystander Effect. *J Pharmacol Exp Ther* **374**, 184-199 (2020).

144. Singh, A.P. et al. Antibody Coadministration as a Strategy to Overcome Binding-Site Barrier for ADCs: a Quantitative Investigation. *AAPS J* **22**, 28 (2020).

145. Joslyn, L.R., Kirschner, D.E. & Linderman, J.J. CaliPro: A Calibration Protocol That Utilizes Parameter Density Estimation to Explore Parameter Space and Calibrate Complex Biological Models. *Cellular and Molecular Bioengineering* (2020).

146. Ponte, J.F. et al. Antibody Co-Administration Can Improve Systemic and Local Distribution of Antibody Drug Conjugates to Increase In Vivo Efficacy. *Mol Cancer Ther* (2020).

147. Khera, E. et al. Quantifying ADC bystander payload penetration with cellular resolution using pharmacodynamic mapping. *Neoplasia* **23**, 210-221 (2020).

148. Clardy, S.M. et al. Abstract 754: Unique pharmacologic properties of Dolaflexin-based ADCs—a controlled bystander effect. *Cancer Research* **78**, 754-754 (2018).

149. Barok, M., Joensuu, H. & Isola, J. Trastuzumab emtansine: mechanisms of action and drug resistance. *Breast Cancer Res* **16**, 209 (2014).

150. Yoshida, G.J. Applications of patient-derived tumor xenograft models and tumor organoids. *J Hematol Oncol* **13**, 4 (2020).

151. Abu-Yousif, A.O. et al. Preclinical Antitumor Activity and Biodistribution of a Novel Anti-GCC Antibody-Drug Conjugate in Patient-derived Xenografts. *Mol Cancer Ther* **19**, 2079-2088 (2020).

152. Bolleddula, J. et al. Pharmacokinetics and Catabolism of [(3)H]TAK-164, a Guanylyl Cyclase C Targeted Antibody-Drug Conjugate. *Drug Metab Dispos* **48**, 1239-1245 (2020).

153. Gallery, M. et al. A monomethyl auristatin E-conjugated antibody to guanylyl cyclase C is cytotoxic to target-expressing cells in vitro and in vivo. *PLoS One* **13**, e0191046 (2018).

154. Waldman, S.A. et al. Heterogeneity of guanylyl cyclase C expressed by human colorectal cancer cell lines in vitro. *Cancer Epidemiology, Biomarkers & Prevention* **7**, 505-514 (1998).

155. Mizumoto, N. et al. Discovery of novel immunostimulants by dendritic-cell-based functional screening. *Blood* **106**, 3082-3089 (2005).

156. Trojandt, S. et al. The chemotherapeutic agent topotecan differentially modulates the phenotype and function of dendritic cells. *Cancer Immunol Immunother* **62**, 1315-1326 (2013).

157. Kashyap, A.S. et al. GEF-H1 Signaling upon Microtubule Destabilization Is Required for Dendritic Cell Activation and Specific Anti-tumor Responses. *Cell Rep* **28**, 3367-3380 e3368 (2019).

158. Muller, P. et al. Microtubule-depolymerizing agents used in antibody-drug conjugates induce antitumor immunity by stimulation of dendritic cells. *Cancer Immunol Res* **2**, 741-755 (2014).

159. Iwata, T.N. et al. A HER2-Targeting Antibody-Drug Conjugate, Trastuzumab Deruxtecan (DS-8201a), Enhances Antitumor Immunity in a Mouse Model. *Mol Cancer Ther* **17**, 1494-1503 (2018).

160. D'Amico, L. et al. A novel anti-HER2 anthracycline-based antibody-drug conjugate induces adaptive anti-tumor immunity and potentiates PD-1 blockade in breast cancer. *J Immunother Cancer* **7**, 16 (2019).

161. Muller, P. et al. Trastuzumab emtansine (T-DM1) renders HER2+ breast cancer highly susceptible to CTLA-4/PD-1 blockade. *Science Translabional Medicine* **7** (2015).

162. Ribas, A. & Wolchok, J.D. Cancer immunotherapy using checkpoint blockade. *Science* **359**, 1350-1355 (2018).

163. Sau, S. et al. Multifunctional nanoparticles for cancer immunotherapy: A groundbreaking approach for reprogramming malfunctioned tumor environment. *J Control Release* **274**, 24-34 (2018).

164. Huang, P.W. & Chang, J.W. Immune checkpoint inhibitors win the 2018 Nobel Prize. *Biomed J* **42**, 299-306 (2019).

165. Sau, S., Petrovici, A., Alsaab, H.O., Bhise, K. & Iyer, A.K. PDL-1 Antibody Drug Conjugate for Selective Chemo-Guided Immune Modulation of Cancer. *Cancers (Basel)* **11** (2019).

166. Weinberg, F. & Gadgeel, S. Combination pembrolizumab plus chemotherapy: a new standard of care for patients with advanced non-small-cell lung cancer. *Lung Cancer (Auckl)* **10**, 47-56 (2019).

167. Brinkmann, U. & Kontermann, R.E. The making of bispecific antibodies. *MAbs* **9**, 182-212 (2017).

168. Andreev, J. et al. Bispecific Antibodies and Antibody-Drug Conjugates (ADCs) Bridging HER2 and Prolactin Receptor Improve Efficacy of HER2 ADCs. *Mol Cancer Ther* **16**, 681-693 (2017).

169. Chen, I.J. et al. Bispecific antibody (HER2 x mPEG) enhances anti-cancer effects by precise targeting and accumulation of mPEGylated liposomes. *Acta Biomater* **111**, 386-397 (2020).

170. Mandikian, D. et al. Relative Target Affinities of T-Cell-Dependent Bispecific Antibodies Determine Biodistribution in a Solid Tumor Mouse Model. *Mol Cancer Ther* **17**, 776-785 (2018).

171. Betts, A. et al. A Translational Quantitative Systems Pharmacology Model for CD3 Bispecific Molecules: Application to Quantify T Cell-Mediated Tumor Cell Killing by P-Cadherin LP DART((R)). *AAPS J* **21**, 66 (2019).

172. Blanco, B., Compte, M., Lykkemark, S., Sanz, L. & Alvarez-Vallina, L. T Cell-Redirecting Strategies to 'STAb' Tumors: Beyond CARs and Bispecific Antibodies. *Trends Immunol* **40**, 243-257 (2019).

173. Herter, S. et al. A novel three-dimensional heterotypic spheroid model for the assessment of the activity of cancer immunotherapy agents. *Cancer Immunol Immunother* **66**, 129-140 (2017).

174. Marin-Acevedo, J.A., Soyano, A.E., Dholaria, B., Knutson, K.L. & Lou, Y. Cancer immunotherapy beyond immune checkpoint inhibitors. *J Hematol Oncol* **11**, 8 (2018).

175. Cao, D., Zheng, Y., Xu, H., Ge, W. & Xu, X. Bevacizumab improves survival in metastatic colorectal cancer patients with primary tumor resection: A meta-analysis. *Sci Rep* **9**, 20326 (2019).

176. Garcia, J. et al. Bevacizumab (Avastin(R)) in cancer treatment: A review of 15 years of clinical experience and future outlook. *Cancer Treat Rev* **86**, 102017 (2020).

177. Mohyeldin, A., Garzon-Muvdi, T. & Quinones-Hinojosa, A. Oxygen in stem cell biology: a critical component of the stem cell niche. *Cell Stem Cell* **7**, 150-161 (2010).